Water Sustainability Fund Report
Project #5192

Dr. Aaron Mittelstet
University of Nebraska-Lincoln

December 2022

Table of Contents

Table of Figures:

Table of tables:

Abstract:

Chapter 1 of this report focused on the assessment of eastern redcedar encroachment in central Nebraska with Landsat and multilayer perceptron. The increase in *Juniperus virginiana* (redcedar) has a significant influence on the grassland ecosystem of the Nebraska Sand Hills. Current redcedar encroachment estimates are mostly localized based on pixel counting approach that do not provide the spatial and temporal variation present within the study area. This study uses object-based image analysis, machine learning, and sampling-based design to estimate the current and historical encroachment rates. The training samples generated using object-based image analysis were refined using visual image interpretation to select pure pixels. Multilayer perceptron (MLP) and random forest classifier were trained and tested to classify 1990, 2000, 2010, and 2020 Landsat images. The classified images were then used to design stratified sampling to calculate and estimate the current and historical redcedar encroachment. A comparison showed MLP extracted redcedar with higher accuracy than the random forest classifier. The estimates show redcedar increased annually by 1.07 -10.95% from 1990-2000, 0.35 -3.85% from 2000-2010, 4.64-5.01% from 2010-2020, and 2.26-11.19% from 1990-2020. The highest encroachment is distributed in counties with a high proportion of Loess canyons and hills. The study reveals that pure pixels selected from winter months using visual interpretation, object-based image analysis, MLP, and the stratified sample provide unbiased estimates of the redcedar area and its encroachment rate. The study demonstrates the potential to extrapolate regional assessments of woody species encroachment in the North American Great Plains.

The next chapter, Chapter 2, covered the use of Markov chain-cellular automata model to predict and assess Juniperus virginiana (redcedar) encroachment in central Nebraska. Eastern redcedar (*Juniperus virginiana*) encroachment is one of the primary threats to the native grasslands in the North American Great Plains. Redcedar encroachment not only reduces the biodiversity but also alters ecosystem services such as groundwater recharge and pasture habitat, both vital for the socio-economy in the region. Redcedar, an invasive native species primarily susceptible to fire proliferated the grasslands with reduction of fire intensity, frequency, and availability of suitable environmental and socio-economic conditions. This study uses Markov chain and cellular automata (Markov-CA) model to characterize the spatial and temporal distribution of redcedar (a dominant evergreen species in the study area) encroachment. A multi-layer perceptron (MLP) neural network optimized for hidden layers, regularization, and dropout ratio were used to identify and extract the redcedar from 1990, 2000, and 2020 Landsat images. Markov-CA approach was used to determine the transition probabilities, transition potential, and redcedar distribution for 2020, 2050, and 2100. The different encroachment rate present in study area were calculated using transition probabilities from the eastern, Halsey National Forest, northern, and southern areas. The northern part showed area estimates closer to stratified random sampling estimates and also had consistent transition probabilities. The predicted redcedar cover using northern area transition probabilities, increased by more

than two-fold (3899 km^2) in 2050 and four-fold (6887 km^2) in 2100 when compared with an area of 1767 km^2 in 2020. Halsey National Forest, an area largely modified by humans because of various management practices showed the decreasing redcedar encroachment over time. The southern transition probabilities resulted in highest redcedar encroachment while the eastern area transition probabilities resulted in the least encroachment. The study shows that the redcedar encroachment scenarios with various encroachment pattern can be used to inform the decision-makers and be incorporated into various biophysical models to simulate effects of encroachment (e.g., hydrological effects of redcedar encroachment).

The third chapter, Chapter 3, evaluated redcedar encroachment impacts on water resources in Nebraska Sandhills. Worldwide, tree or shrub dominated woodlands have encroached into herbaceous dominated grasslands. While very few studies have evaluated the impact of Eastern Redcedar encroachment on the water budget, none have analyzed the impact on water quality. In this study, we evaluated the impact of redcedar encroachment on the water budget in the Nebraska Sandhills, a major recharge zone for the High Plains Aquifer, and how the decreased streamflow would increase nitrate and atrazine concentrations in the Platte River. We calibrated a Soil and Water Assessment Tool (SWAT model) for discharge, recharge, and evapotranspiration. Using a moving window (3x3 m to 7x7 m) with a dilate morphological filter, encroachment scenarios of 11.9%, 16.1%, 28.0%, 40.6%, 57.5%, 72.5% and 100% were developed and simulated by the calibrated model. At 11.9% and 100% encroachment, discharge was reduced by 4.6% and 45.5%, respectively in the Upper Middle Loup River, a tributary to the Platte River. With 28% of the Platte River water originating from the Loup River, discharge in the Platte River, a major water source for Omaha and Lincoln, at encroachment levels of 28%, 57.5%, and 100% would decrease by 2.6%, 5.5%, and 10.5% respectively. This reduction in streamflow could increase nitrate concentrations from 1.44 to 1.61 m L^{-1}, and atrazine from 1.22 to 1.37 µg L^{-1}. The recharge decreased by ___ and the ET increased by ___. At 28% encroachment, the modeled risk level for atrazine would increase from (1) Low Risk to 2 (At Risk) and the dual risk of nitrate and atrazine could increase from Medium Low Risk to Medium Risk, based on our modeling assumptions.

The last chapter, Chapter 4, focused on combined impacts of redcedar encroachments and climate change on water resources in the Nebraska Sandhills. The Nebraska Sand Hills (NSH) is considered a major recharge zone for the High Plains Aquifer in the central United States. The uncontrolled expansion of the eastern redcedar (*Juniperus Virginiana*) under climate warming is posing threats to surface water and groundwater resources. The combined impact of land use and climate change on the water balance in the Upper Middle Loup River watershed (4,954 km^2) in the NSH was evaluated by simulating different combinations of model scenarios using the Soil Water Assessment Tool (SWAT) model. A total of 222 climate models were ranked according to the aridity index and three models representing wet, median (most likely), and dry conditions were selected. Additionally, the impacts of carbon dioxide (CO$_2$) emissions on

root water uptake were simulated. Four plausible redcedar encroachment scenarios, namely 0.5% (no encroachment), 2.4%, 4.6%, and 11.9%, were considered in the numerical simulations. We, therefore, built: *i*) the historical scenario (2000-2019) with the current climate and redcedar cover leading to baseline results; *ii*) the most-likely future scenario (2020-2099) with projected climate (50th percentile of aridity index distribution) and redcedar encroachment that was estimated by using a combination of neural network and Markov-chain cellular automata model; *iii*) 16 future scenarios (2020-2099) with different combinations of extreme climate (5th and 95th percentiles of aridity index distribution) and four hypothetical encroachment scenarios (0.5%, 2.4%, 4.6%, and 11.9%). The most-likely climate projection indicates that a warming pattern will be expected with a 4.1°C increase in average temperature over the 100-year period, and this will be associated with lower-than-normal precipitation (P). Nevertheless, the concurrent increase in temperature and CO_2 concentration is likely to induce stomata closure by reducing potential (ET_p) and actual (ET_a) evapotranspiration losses. Projected P, ET_p, ET_a, and discharge (D) are expected to decrease by 6%, 39%, 24%, and 2%, respectively, while recharge (R) will likely increase by 27%. Finally, a sensitivity analysis of 16 combined climate and land use scenarios is presented and discussed. The scenario modeling approach presented in this paper can support decision-making by stakeholders for optimal management of water resources

Chapter 1.   Assessing eastern redcedar (Juniperus virginiana) encroachment in central Nebraska with Landsat and multilayer perceptron

1.1. Introduction

The North American Great Plains hosts one of the most biologically significant grassland ecosystems with exceptional and distinct biodiversity (Olson and Dinerstein, 2002). However, the semi-arid grassland ecosystem has undergone significant changes with its range reduced by as much as 70% since European settlement (Samson et al., 2004). Besides the direct loss, the remnant grasslands are overexploited and fragmented through overgrazing, recreational activities, and proliferation of woody plant species (trees and shrubs) (Briggs et al., 2002; Knapp et al., 2008; Meneguzzo and Liknes, 2015; Van Auken, 2009). Eastern redcedar (*Juniperus virginiana*; hereafter redcedar) and Mountain juniper (*Juniperus scopulorum*) have proliferated the Great Plains, once dominated by tall and mixed-grass prairies (Barger et al., 2011). The woody encroachment rates are 5-7-fold higher (1.7% cover change yr^{-1}) relative to ecoregions outside of the Great Plains (< 0.4% cover change yr^{-1}) (Barger et al., 2011). For example, redcedar coverage in Nebraska increased from 9% to 17% from 2005 to 2012 (Meneguzzo and Liknes, 2015). Although introduction of redcedar has some ecological and socioeconomic benefits, it significantly reduces biodiversity (Knapp et al., 2008; Van Auken, 2009) and may fully convert a native grassland into a closed-canopy redcedar forest in as little as 40 years (Briggs et al., 2002). In addition to biodiversity loss and socio-economic impact (Anadón et al., 2014a; Twidwell et al., 2013), the encroachment causes direct and indirect impacts on the hydrological (stream runoff, groundwater recharge) (Huxman et al., 2005; Zou et al., 2018), carbon (alters carbon and carbon accumulation) (Asner et al., 2003; McKinley and Blair, 2008; Norris et al., 2001) and nutrient cycles. The primary factors that accelerate redcedar encroachment are exclusion or reduction of wildfires, intensive grazing, and climate change (Briggs et al., 2002; Fowler and Konopik, 2007). Other factors that aid in the process are edaphic (Rodriguez-Iturbe, 2000), above and belowground competition (Brown and Archer, 1999; Wilson and Witkowski, 1998), biogeochemical and biophysiological properties, land degradation as a part of desertification process or successional process of an ecosystem (Briggs et al., 2002; Cordova et al., 2011; Van Auken, 2009).

Remote sensing is widely used to identify the species distribution (Fassnacht et al., 2016; Ghosh et al., 2014; He et al., 2015; Noujdina and Ustin, 2008; Ustin et al., 2004; Weisberg et al., 2007), plant invasions (Alvarez-Taboada et al., 2017; Bradley, 2014; Peerbhay et al., 2016), and potential distribution of invasive species (Baidar et al., 2017; López and Stokes, 2016; Rocchini et al., 2015). Redcedar, or in general conifer species have been identified using satellite images (Filippelli et al., 2020; C. Wang et al., 2018; Weisberg et al., 2007). Remote sensing-based encroachment assessment involves the identification of individual or groups of plants/canopies (based on the spectral and spatial characteristics) in images (Meddens et al., 2016). In higher-resolution aerial or satellite images, individual or groups of species are interpreted with

manual, semi-automatic, or object-based image analysis (Asner et al., 2003; Coop and Givnish, 2007; Filippelli et al., 2020; Hudak and Wessman, 1998; Weisberg et al., 2007). Moderate resolution satellite images are mainly used to evaluate spatial and temporal distribution of species at the regional scale. Automatic and semi-automatic methods are preferred and developed with the availability of multi-spectral, temporal, and multi-sensor (optical, LIDAR, microwave) images. However, due to spectral similarity between redcedar with other vegetation types (e.g., vegetation in wetlands) and sparse occurrence (early stage of encroachment), the differentiation of redcedar has shown mixed results. For example, although (Kaskie et al., 2019) reported high accuracy (88.9%) using matched filtering approach to differentiate redcedar on snow-covered images, the accuracy was lower (74.1%) on non-snow-covered and seasonal images. The sub-pixel approaches mainly used to extract species in mixed pixels have difficulty in proper identification of endmembers spectra. A reference spectral library representing pure reflectance values in laboratory conditions may not represent actual reflectance values due to changes in radiometric or spatial characteristics (Quintano et al., 2012), while image based endmembers may vary greatly with space (e.g., different scene) and time (multi-year) (Sankey et al., 2010). Similarly, a pixel and phenology-based method as proposed by (Wang et al., 2017) showed limitations due to seasonal availability of cloud-free images (J. Wang et al., 2018). The data fusion-based methods reported a marginal (0-5%) increase in Juniper detection and delineation when compared with LIDAR or microwave-based methods (Erdody and Moskal, 2010; Hyde et al., 2006). A neural network with multiple hidden layers and neurons learn complex pattern and hidden relationship between the target and explanatory features and provide higher accuracy in object detection and extraction.

Machine learning approaches such as support vector machine, random forest, and neural network have shown promising results in classifying and detecting an object of interest from remote sensing images. Random forest classifier with a smaller number of hyper parameters is easily implemented and provide accuracy similar to support vector machine (SVM) and artificial neural networks (ANN) with single hidden layer. In general, neural network-based with multiple hidden layers have resulted in higher accuracy than the support vector machine and random forest methods while classifying land cover and land use maps (He et al., 2016; Hu et al., 2015; Kussul et al., 2017; Raczko and Zagajewski, 2017). Neural network, however, require large quantity of high-quality training samples: any noise present in samples my result in inaccurate representation of features. The most used neural network architecture in remote sensing is the multilayer perceptron (MLP), convolution neural network (CNN), recurrent neural network (RNN), autoencoders (AE), deep belief networks (DBN), and generative adversarial networks (GAN) (Li et al., 2018; Ma et al., 2019). MLP is widely used in image classification (Del Frate et al., 2007; Zhang et al., 2018) and extraction of targeted features such as rice (Tang et al., 2022), and surface water extraction (Jiang et al., 2018). MLP typically with a single, or additional hidden layers can learn non-linear relationships between the input and

response variables with a smaller number of samples (Tang et al., 2022; Zhang et al., 2018). A quality samples for this research is generated through combination of object-based image classification of high-resolution satellite/aerial images and visual interpretation.

While remote sensing-based methods are widely used to extract and estimate encroachment, most rely on a pixel counting approach (Olofsson et al., 2014). The pixel counting method is biased partly because it uses each of the pixels (population) to estimate an area and does not consider the classification error. A sampling-based approach such as suggested by (Olofsson et al., 2014) uses samples derived from the interpretation of high-resolution images to provide unbiased area estimates and associated encroachment rates. The goal of this study is to examine the application of a MLP with multiple hidden layers to assess redcedar encroachment in central Nebraska using Landsat images. The integration of high-resolution National Agriculture Imagery Program (NAIP) images with MLP helps identify and locate redcedar with higher accuracy, address some of the limitations imposed in the above-discussed methods and provides a simple and robust approach to identify redcedar. The specific objectives of this research are to 1) integrate object-based image analysis and MLP to extract redcedar; 2) evaluate and validate the extracted redcedar using stratified sampling; and 3) estimate annual encroachment rates from 1990-2020.

1.2. Materials and Methods

1.2.1. Study area

The study area Figure 1-1 lies in central Nebraska and covers the hotspots of redcedar encroachment in the Nebraska Sand Hills Figure 1-1.b. The study area covers different percentage of tree canopy cover and redcedar percent as shown in (Meneguzzo and Liknes, 2015). The area covers latitude from 44.46 N to 42.99 N and longitude from 102.48 W to 99.34 W covering an area of 70,759 km^2. The area is characterized by strong topographical variation with a wetter climate in the east and drier in the west. The study area is primarily dominated by permeable coarse sand that promotes recharge to the underlaying High Plains Aquifer while sandy soil is present in the interdunal valleys (Barnes et al., 1984). The mean annual temperature is 10°C while precipitation ranges from 400-500 mm. As per the 2016 National Landcover Database (NLCD), the area is dominated by grassland (84%), hay/pasture (8.7%), and wetlands (4%). Forest occupies around 1% of the land area and is composed of evergreen (0.30%), mixed (0.35%), and deciduous (0.35%) trees (Dewitz, 2019).

Native grass species such as little bluestem (*Schizachyrium scoparium*), switchgrass (*Panicum virgatum*), sand dropseed (*Sporobolus cryptandrus*), yucca (*Yucca* spp.), and Kentucky bluegrass (*Poa pratensis*) are dominant species. Tree species include redcedar, ponderosa pine, hackberry, green ash, red mulberry, bur oak, American elm, eastern cottonwood, honeylocust, and Siberian elm. Redcedar, a native conifer species of the United States, is distributed to the East of the Rockies and occupies the eastern and central portions of Great Plains (Lawson, 1990) . Although their expansion was originally limited by

wildfires, redcedar with drought resistant characteristics has proliferated into grasslands as well as understory in mature oak-hickory and deciduous forest (Lassoie et al., 1983). For example, among trees with at least three or twelve-centimeter diameter at breast height, redcedar comprises at least 80% and ponderosa pine occupies 18% of live conifer species (see Supplement1) and are considered dominant species in Nebraska (Forest Service, 2020). The study area also hosts Halsey National Forest, a largest human planted forest in the United States (Hellerich, 2006). Redcedar although largely occupies stream channels and Loess hills, the percentage of conifer is increasing at an alarming rate, especially in the areas excluded from Forest Inventory Analysis (FIA). FIA defines forest as land with at least 10 percent live-tree canopy cover, at least 4046 m^2 in size, and 36 m wide (Meneguzzo et al., 2018). Many redcedar and ponderosa pine species in the forest and trees outside the forest show the growing concern of invasive nature and the need to have an accurate map depicting the spatial and temporal distribution in Nebraska.
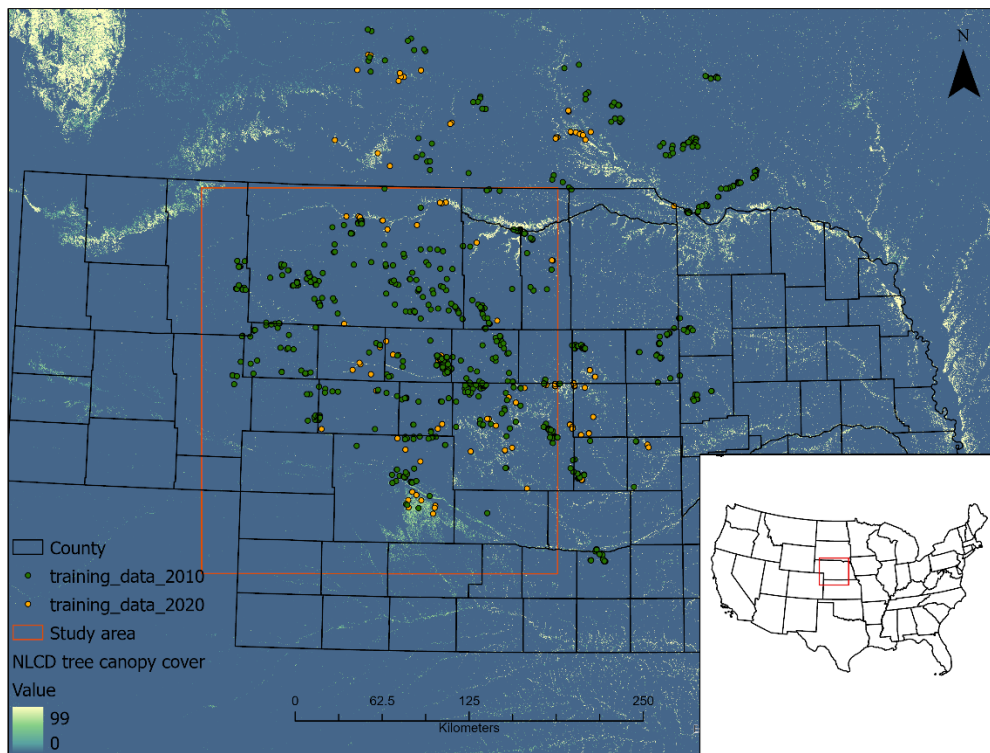
Figure 1-1. Study area illustrating the training sample (redcedar and others) used to classify 1990, 2000, 2010, and 2020 Landsat images. Some of the training samples were collected from regions outside of the study area. Background images shows NLCD percent tree canopy cover from 2016.

1.2.2. Data

Landsat 5 and 8 images with 30 m spatial resolution were used to extract the redcedar. We used surface reflectance images from winter months (November-April) hosted in the Google Earth Engine (GEE) with cloud cover less than 30% from 1990, 2000, 2010, and 2020. The winter month (dormant period) images helped to differentiate the redcedar (green vs dry/yellow leaves) from other species present in the study area. Since a limited number of snow-free images were available within a year and the number and density of redcedar does not change significantly within 1-2 years, we used the preceding and the following years to increase the number of snow and cloud-free images (i.e., a 1990 mosaic contains images from 1989 and 1991) and reduce the uncertainties caused by the limited data availability. NAIP data sets consists of either red, green, blue, or near-infrared spectral bands with a spatial resolution between 0.6 to 1 m. Training samples were generated using 2020 and 2010 NAIP images. Samples to validate the areas estimates were generated using visual interpretation of 2020, 2010, 2003 NAIP and 1993, 1994, and 1999 panchromatic digital orthophoto quadrangles (DOQ).

1.2.3. Redcedar encroachment assessment

We used MLP and random forest classifiers to identify and extract redcedar from Landsat 5 and 8 images. The process involves Figure 1-2 i) subset, classify, interpret, and select pure pixels to generate training samples, ii) spectrally transform and combine original bands of Landsat, iii) train, test and predict using MLP, and v) estimate and validate the redcedar using stratified sample design.
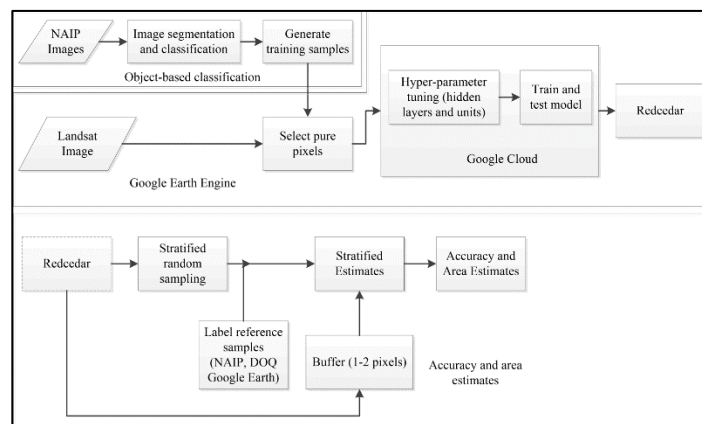
Figure 1-2. Workflow to differentiate and estimate redcedar encroachment using an integration of object-based image analysis, multilayer perceptron, and stratified sampling.

1.2.4.2.3.1 Image pre-processing

The Landsat images were mosaicked using the median values and transformed to compute principal component analysis (PCA), hue, saturation, and value (HSV) (Smith, 1978), and tasseled cap (TCAP) (Crist

and Cicone, 1984) images. The normalized difference vegetation index (NDVI) [NIR − Red)/(NIR + Red] (Tucker, 1979), and normalized difference built-up index (NDBI) [SWIR− NIR)/(SWIR + NIR (Zha et al., 2010) were also calculated. We then stacked the PC1, PC2, and PC3-PCA, hue-HSV, brightness, greenness, wetness-TCAP, NDBI, and NDVI with the original bands as an input to provide spectral variability for the classifier. We included NDBI as the SWIR-based indices are associated with conifer forest structure (Cohen and Spies, 1992; Lobell et al., 2001; Puhr and Donoghue, 2000).

1.2.5. Collection of training samples

The training samples were generated using classification and manual interpretation of NAIP images for 2010 and 2020. High-resolution NAIP images provide proper identification of redcedar locations. The areas representing different tree canopy cover Figure 1-1 were clipped and classified using object-based image classification. The smaller subset of images not only improved the processing time but also provided a homogenous background for easier redcedar identification and extraction. The object-based method involves segmentation and classification of images. The segmentation splits the image into separated regions (objects) based on spectral and spatial similarity (Im et al., 2008). We used eCognition Developer 9 to perform object-based classification. The multiresolution segmentation algorithm splits the images into segments based on the shape, compactness, and scale parameter. The shape parameter controls the spectral homogeneity, compactness defines the object shape between the smooth boundaries and compact edge, and scale determines the size of the object (Benz et al., 2004). To include the smaller redcedar, we segmented the images with a combination of scale (20), color (0.7), and shape (0.3) parameters. The objects were then classified using the nearest neighbor classifier. The nearest neighbor uses a set of samples (selected using visual interpretation) from different classes and assigns values to each object. We used the mean brightness, a standard deviation of the individual bands, and NDVI to differentiate the redcedar from other species.

The sample points, generated randomly within the boundaries of extracted redcedar cover, was then overlaid on Landsat images to identify the pure Landsat pixels through visual interpretation. Pure pixels were defined when a pixel entirely contains redcedar, mostly the center pixels within boundary defined by classified NAIP images. Although, a patch may occur as redcedar, due to similar spectral and temporal characteristics, the samples may include Pinus species. The training samples were collected in the ArcGIS with aided by visual interpretation of images in Google Earth Pro, digital orthophoto quadrangle (DOQs). A total of 1065 [348, 717] and 785 [276,509] training samples were generated for redcedar and others respectively for 2010 and 2020 respectively. Others class contain samples from grassland, water, barren, wetland, and built-up areas.

1.2.6. Image classification

The MLP algorithm typically has a fully connected network of an input, hidden, and output layers. We modified the network to include more hidden layers Figure 1-3 so that neurons on multiple hidden layers can transform and learn patterns at multiple levels of abstraction. The training involves learning with an objective function that measures the error between the output and desired scores and alters internal parameters (e.g, weights) to reduce the error (Del Frate et al., 2007). The backpropagation algorithm updates and optimizes weights sequentially in the forward and backward directions.
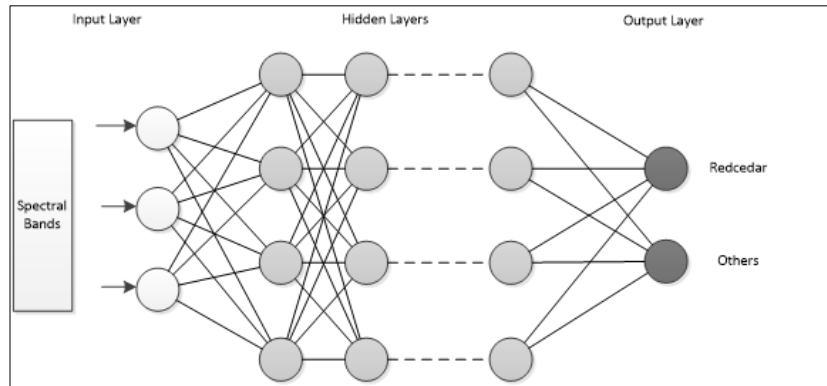
Figure 1-3. Multilayer perceptron network architecture with multiple hidden layers for Landsat image classification.

To reduce the difference in spectral response between the Landsat 5 and 8 sensors, we developed an L5-MLP and L8-MLP model. The optimum number of hidden layers, the number of neurons, and activation function were determined using a random search hyper-parameter tuning algorithm. The tuning process determined the 5 and 3 fully connected hidden layers with 32 nodes in each layer for L5-MLP and L8-MLP. A combination of a dropout ratio of 0.2 and regularization (L2) was used to facilitate the learning process and avoid overfitting the model. A rectified linear unit (ReLU) was selected as a non-linear mapping function. The parameters of the neural network were tuned using 100 epochs with 70% of the samples to train and 30% to test the model. The neural network architecture was implemented using GEE and TensorFlow library in Google Cloud Service Figure 1-2. The L5-MLP model constructed with 2010 data was also used to classify the 1990 and 2000 images as they use the same Landsat 5 sensor. The resultant probability maps were reclassified using the threshold of 10% or more to extract the redcedar cover.

In order to compare the performance, a random forester classifier was also developed using training samples of 2010 and 2020. The number of variables per split parameter were the square root of the number of features in the model (a default parameter in GEE) consistent to the studies using random forest for remote sensing applications (Belgiu and Drăgu, 2016). The optimal number of trees was tested using 20, 50, 100, and 200 trees. We used 20 trees for 2010 and 200 trees for 2020 on final random forest models (Table 1-2).

1.2.7. Area estimates and accuracy assessment

The area of the redcedar cover was estimated using the stratified design and estimation method at 95% confidence interval (Cochran, 1963; Olofsson et al., 2013). The pixel counting method does not consider classification errors, thus resulting in biased area estimates that may not provide a true representation of land cover classes (Olofsson et al., 2013; Stehman, 2009). The stratified sampling-based approach considers classification error as well as the proportion of the landcover classes thereby providing a more accurate representation of land cover classes (Olofsson et al., 2014). The classified images from 1990, 2000, 2010, and 2020 were stratified into the redcedar and other classes. Stratified random sampling approach was used to estimate the number of samples from each of the classified images. The number of samples was determined using 0.01 (1%) target standard error for overall accuracy. Of the 909 points generated, 305 samples were allocated to redcedar while 604 samples were allocated to other strata. Although (Olofsson et al., 2014) suggested a minimum of 50 samples for smaller classes, our initial sample allocation of 50 to redcedar resulted in a larger confidence interval (higher uncertainty in the estimates), therefore we allocated larger samples to the redcedar. The samples were generated in GEE using AREA2 tool (Arévalo et al., 2020; Bullock et al., 2020). The generated samples were labeled based on the visual interpretation of high-resolution NAIP, USGS DOQs, and GEE images. A second analyst performed independent verification of the samples while any conflict was discussed to either include or exclude from the analysis based on agreed consensus. The overall, producer's and user's accuracy were calculated. A detail in method and equation is provided in (Cochran, 1963) and (Olofsson et al., 2013).

The stratified estimation, however, results in higher omission error when the sample from a class occupying a small proportion of the study area falls into class with a larger proportion leading to uncertainty in precision of the estimates (Olofsson et al., 2020). Since redcedar encroachment is in the early stages (see **Figure 1-10**) and occupies a smaller proportion of the study area, we buffered the redcedar strata by one (30 m) and two pixels (60 m) to reduce the uncertainty caused by the higher weight of larger strata. The buffered maps were created by passing classified through morphological filter using focal max operation in GEE. The accuracy of the MLP model was evaluated using the accuracy and loss metrics (Géron, 2019). Encroachment rates were then calculated for the entire period between 1990-2020 and the decadal period between 1990-2000, 2000-2010, and 2010-2020.

1.3. Results

1.3.1. Training sample generation

The object-based image classification approach was used to extract the redcedar from NAIP images. The visual interpretation shows a high level of correspondence between classified and reference images. Because images were clipped in areas of known redcedar and mostly contained homogenous grass cover as background (Figure 1-4 a,b,c), redcedar is well-differentiated from other species (Figure 1-4 d, e, f).

Although the boundary is overestimated by a fraction of pixels, the result fulfills the purpose of identifying pure pixels in Landsat images. Pure pixels were selected using larger redcedar cover e.g., Figure 1-4 a,d, and c, f containing multiple Landsat pixels, while smaller areas that do not represent redcedar cover in the Landsat images, (e.g., Figure 1-4 b, e) were not used.
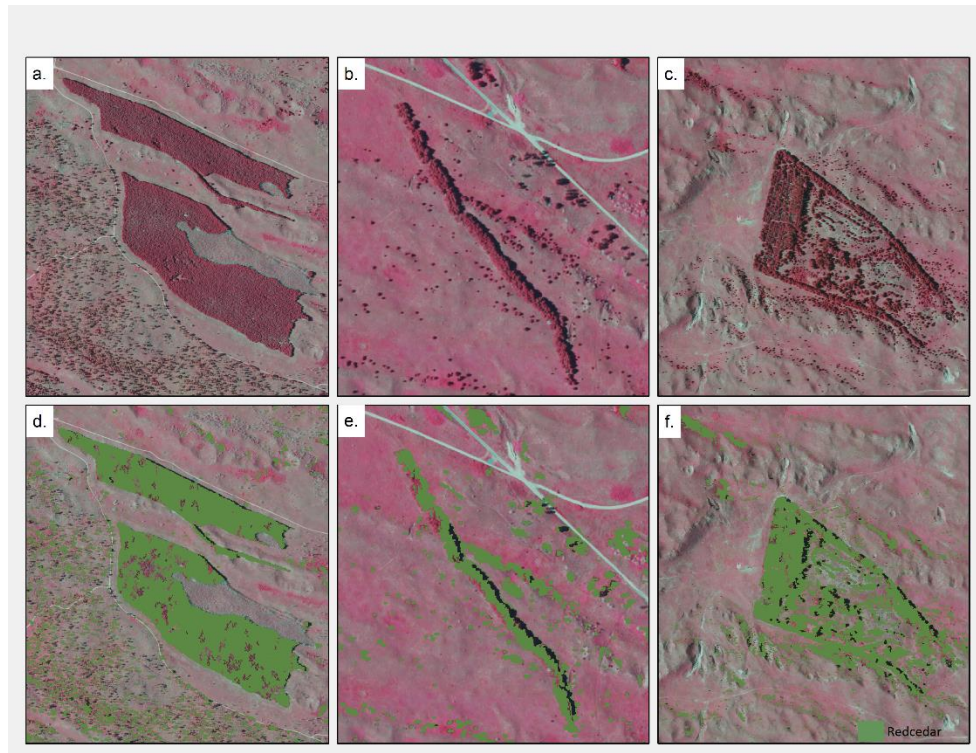
Figure 1-4. Redcedar identification using object-based image classification of National Aerial Imagery Program (NAIP) images (e.g., 2020). The upper row (a, b, c) shows the false-color composite of NAIP images while the bottom row (d, e, f) shows the extracted redcedar overlaid on the corresponding NAIP images.

1.3.2. Spectral response of redcedar vs other classes

The use of spectral transformation provides the difference in spectral response between classes for the MLP classifier. The spectral curve between the wetland vegetation, deciduous trees, and redcedar has a similar pattern in the visible and near-infrared spectrum Figure 1-5a. Spectral transformation provides the classifier with a differing response pattern between classes Figure 1-5b. For example, redcedar shows higher values in the first principal component (pc1) and lower values in NDBI and has lower brightness and higher greenness values in tasseled cap transformed images compared with wetland and deciduous classes Figure 1-5. A combination of the original bands and the spectrally transformed bands, therefore, provides spectral variability between classes for identification and classification.
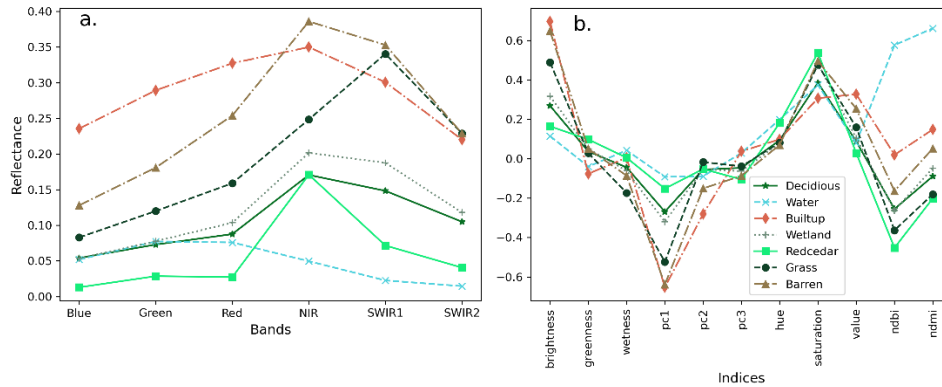
Figure 1-5. Spectral response curves of redcedar vs. others land cover (deciduous, water, built-up, wetland, grass, and barren) types in the study area with original (a) and spectrally transformed bands for median Landsat-8 winter images (b). The original bands represent the blue (B2), green (B3), red (B4), near-infrared (B5), and short-wave infrared (B6/B7).

1.3.3. Model performance

The internal model performance was evaluated using the accuracy and loss metric from training and testing data. The result shows that L8-MLP has better correspondence between the train and test accuracy and loss Figure 1-6a. The L5-MLP also shows a good correspondence between the train and test accuracy and loss below Figure 1-6b. The results from both models show the minimal presence of overfitting and underfitting as the accuracy and loss in training and testing data do not diverge by a huge difference.
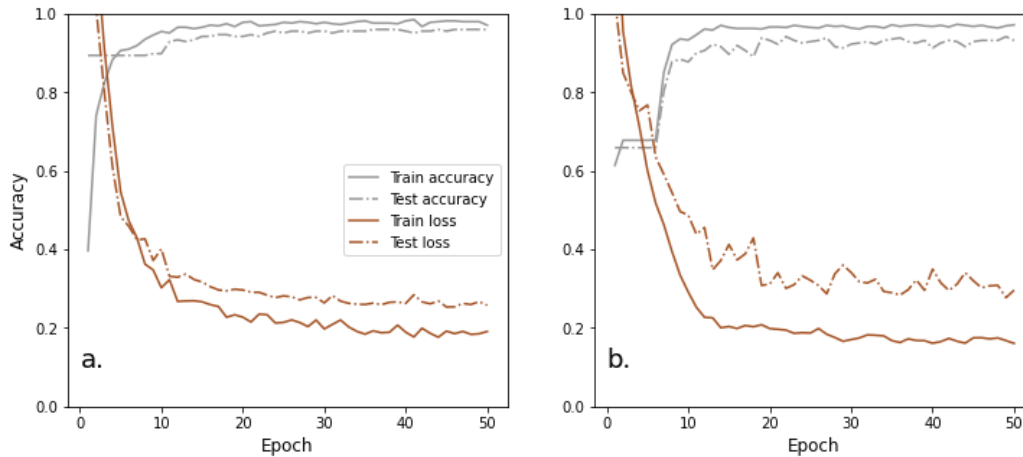
Figure 1-6. Internal model evaluation using the accuracy and loss function for the L8-MLP (a) and L5-MLP (b) model on the training and test dataset.

1.3.4. Accuracy assessment and area estimates

A comparison of MLP and random forester classifier shows that MLP provides better estimates of redcedar cover than the random forest classifier. With original classified images, MLP has higher overall, producer's and user's accuracy than the random forest classifier. With the buffered maps, the difference, however, is minimal (Table 1-1). The result from MLP models show high overall accuracy (>99%) for

classified maps of 1990, 2000, 2010, and 2020 along with the corresponding buffered maps (Table 1-1) at 95% confidence interval. The high producer's and user's accuracy (>98%) of other classes such as agriculture, water, grassland, wetlands, built-up, and barren areas shows proper differentiation of redcedar (Table 1-1). However, redcedar showed higher omission error, especially in 1990, as the redcedar encroachment was at very early stages and occupied only fraction of pixel leading to mixed pixel effects. The use of class weight in a stratified estimator also contributes to higher omission error as it falls on a class with a high weight (Table 1-3). The use of a buffer (1 and 2 pixels) considerably reduced the omission error, although it also increased the commission error (Table 1-1).

Table 1-1: Overall, producer's and user's accuracy for redcedar in 1990, 2000, 2010, 2020 at original, one and two pixels buffered redcedar maps.

Labels	Original		One Pixel Buffer		Two Pixel Buffer	
	1990					
Overall accuracy (± 95% CI)	0.993(±0.007)		0.994(±0.006)		0.995(±0.005)	
Property/ Strata	redcedar	others	redcedar	others	redcedar	others
Area (ha)	606.79	68131.53	686.30	68063.83	765.50	67991.13
95% Cl (ha)	470.49	470.49	409.58	409.58	334.82	334.82
Producer's	0.21	1.00	0.47	1.00	0.69	1.00
User's	0.84	0.99	0.84	1.00	0.84	1.00
	2000					
Overall accuracy (± 95% CI)	0.996(±0.005)		0.995(±0.005)		0.996(±0.003)	
Property/ Strata	redcedar	others	redcedar	others	redcedar	others
Area (ha)	512.63	68225.30	896.55	67853.58	1151.54	67605.09
95% Cl (ha)	316.02	316.02	316.69	316.69	227.49	227.49
Producer's	0.56	1.00	0.75	1.00	0.90	1.00
User's	0.88	1.00	0.87	1.00	0.87	1.00
	2010					
Overall accuracy (± 95% CI)	0.996(±0.005)		0.997(±0.003)		0.996(±0.003)	
Property/ Strata	redcedar	others	redcedar	others	redcedar	others
Area (ha)	630.61	68106.21	1029.17	67720.96	1488.62	67268.01
95% Cl (ha)	315.57	315.57	226.25	226.25	230.11	230.11
Producer's	0.64	1.00	0.89	1.00	0.92	1.00
User's	0.91	1.00	0.89	1.00	0.88	1.00

	Random forest classifier					
Producer's	0.18	1.00	0.75	1.00	0.90	1.00
User's	0.91	0.96	0.89	0.99	0.87	1.00
	2020					
Overall accuracy (± 95% CI)	0.994(±0.006)		0.995(±0.005)		0.993(±0.005)	
Property/ Strata	redcedar	others	redcedar	others	redcedar	others
Area (ha)	913.79	67822.86	1521.47	67228.66	2169.28	66587.35
95% Cl (ha)	385.21	385.21	316.09	316.09	319.71	319.71
Producer's	0.63	1.00	0.85	1.00	0.90	1.00
User's	0.92	1.00	0.91	1.00	0.90	1.00
	Random forest classifier					
Producer's	0.41	1.00	0.82	1.00	0.91	1.00
User's	0.94	0.98	0.92	1.00	0.90	1.00

A visual comparison highlights that the redcedar coverage is well-represented by the MLP classification approach. The probability map Figure 1-7 from L8-MLP overlaid on corresponding NAIP images shows that redcedar is well-differentiated from other land cover classes and avoided misclassification, especially in areas that contained wetlands. Areas with significant redcedar coverage (Figure 1-7 a, b) have high redcedar probability (> 50%) while areas with no or little redcedar coverage have low redcedar probability (<10%). However, in some areas where the redcedar are mixed (understory or overlapping canopies) with deciduous trees and other vegetation (Figure 1-7 f, g), MLP showed limited success due to overlapping spectral signature.
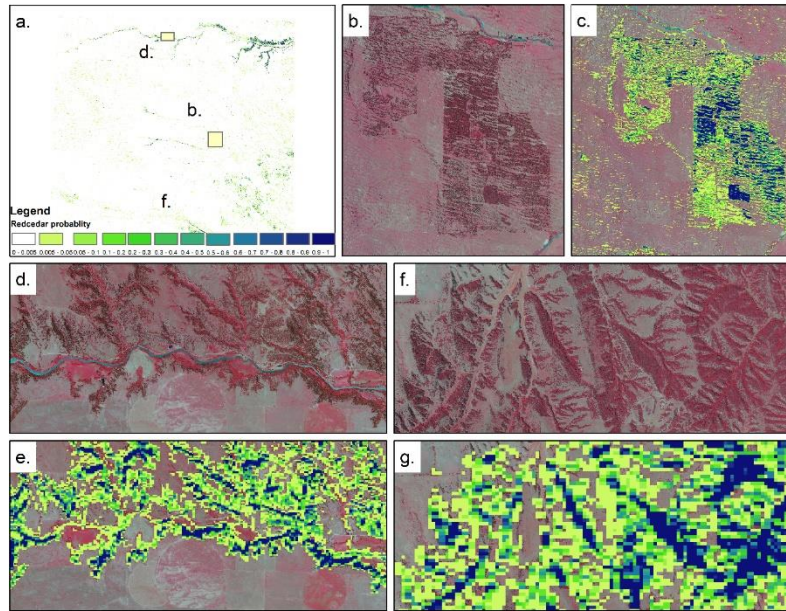
Figure 1-7. A visual comparison between 2020 NAIP image (false-color composite) and extracted redcedar probability using L8-MLP. A darker tone of red color is redcedar while the lighter red (brighter) is deciduous trees or other vegetation in NAIP images.

The estimated redcedar area of 606 ± 470 km^2 in 1990 is greater than 512 ± 316 km^2 in 2000 (Table 1). The larger area estimates in 1990 compared to 2000 shows the effect of uncertainty due to lower producer's accuracy (~20%) and larger confidence interval. Therefore, we used area estimates from one pixel buffered maps for further analysis. The use of buffered maps may, however, overestimate redcedar area and its associated encroachment rates. The redcedar area estimates in one and two pixels buffered maps increased consistently from 1990, 2000, 2010, and 2020 (Figure 1-8). The one- and two-pixel buffer reduced omission errors and range in confidence interval. The process, however, increased the commission error as the buffer covered more sample points at the boundaries.
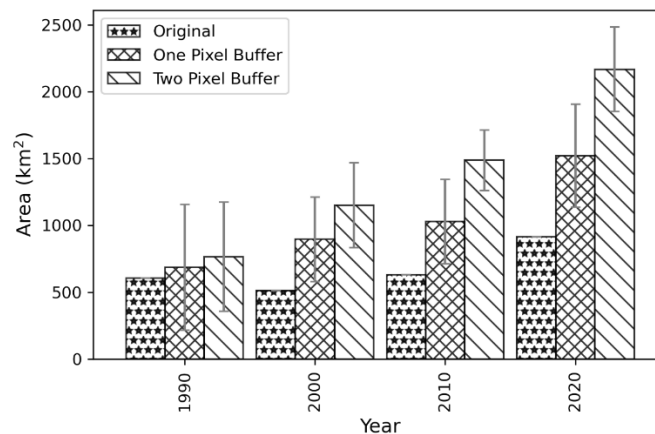
Figure 1-8. Comparison of redcedar cover between original, one, and two pixels buffered maps.

24

1.3.5.Pattern in redcedar encroachment

We used one-pixel buffered maps to calculate redcedar encroachment rates. The results (Table S3) provide ranges in encroachment rates present in the study area at 10-year intervals. The time period from 2000-2010 has the lowest encroachment rate while 1990-2000 has the highest. The overall (1990-2020) encroachment rate varies between 2.26 to 11.19% per year in the study area (Table S3). The range in encroachment rates provides the spatial and temporal variation in redcedar encroachment present in the study area that can be used to generalize rates for Nebraska.

A visual interpretation of the redcedar encroachment shows a substantial change in the eastern, northern, and southern parts of the study area. The Loess canyons in the southern (Figure 1-9 e, f, g, h) and (Figure 1-9 I, j, k, l) hills along the Niobrara and Missouri Rivers in the northern part shows the highest increase in redcedar. The Halsey Forest (Figure 1-9 a, b, c, d), the largest man planted forest (Hellerich, 2006), shows little change due to the implementation of management practices such as prescribed burning. The results show that redcedar favors certain landscape types and could be managed through the proper implementation of management practices.
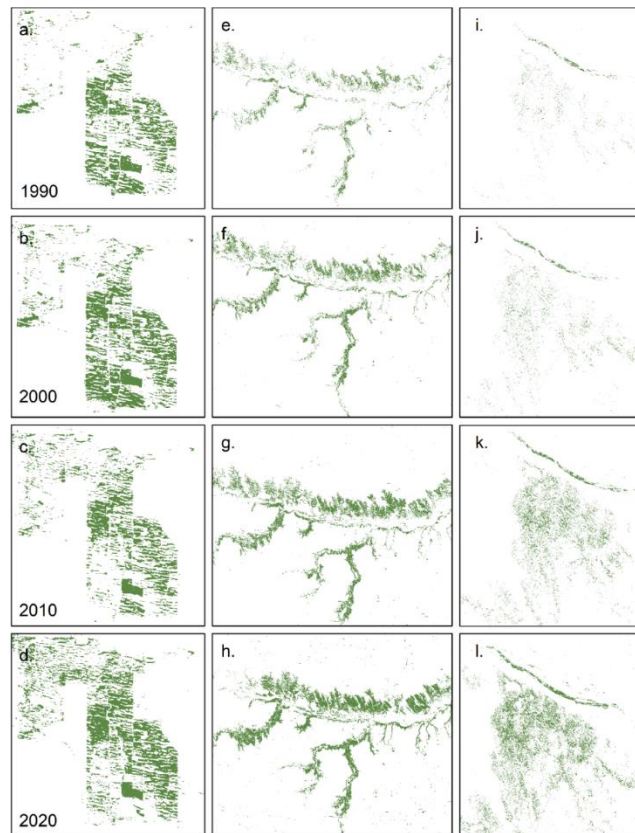
Figure 1-9. Pattern in redcedar encroachment along the Halsey National Forest (a, b, c, d), Missouri River (e, f, g, h), and Loess canyons (i, j, k, l) in 1990, 2000, 2010, and 2020.

1.4. Discussion

This study shows promising results in redcedar encroachment assessment in central Nebraska. A combination of object-based image analysis, MLP, winter images, and sampling-based method helped reduce uncertainty to provide unbiased area estimates and encroachment rates. The identification of pure pixels using visual interpretation of training samples generated using OBIA provided an unambiguous representation of the redcedar location necessary for the classifier to learn and discriminate the non-linear association between the target and other classes. Similarly, high spatial resolution images (e.g, NAIP) provide high-quality and reliable training samples that are a basis for land use and cover classification when field surveys are difficult and costly to conduct (Copass et al., 2018). The quality, quantity, and distribution of training samples are the most important determinants for proper quantification of classes (Mellor et al., 2015; Millard and Richardson, 2015; Zhou et al., 2020; Zhu et al., 2016). Although a large number of training samples of major and minor classes leads to the most accurate classification results (Hermosilla et al., 2022; Zhu et al., 2016), limited occurrence of species (e.g., redcedar) may lead to a compromise to find the balance between the quality and quantity of the training samples. An incorrectly labeled training sample may increase data noise leading to a reduction in classification accuracy (Mellor et al., 2015; Rodriguez-Galiano et al., 2012; Rogan et al., 2008). With an early stage of encroachment (Figure 1-10) and limited coverage of redcedar, the research focused on identifying pure pixels using high-resolution images.

The results show that the MLP classifier produced better results than the random forest classifier. While random forest and single hidden layered MLP produce comparable results in feature identification, land use and land cover analysis, extraction of redcedar from Landsat images were less accurate than the MLP classifier. With multiple hidden layers provides hierarchical framework to reveal the non-linear relationship at multiple scale between input and response variables (Géron, 2019; LeCun et al., 2015). The two MLP models were developed to reduce the difference in spectral and radiometric quantization between the Landsat 5 and 8 sensors. We also assumed that the reflectance images, corrected for atmospheric effects, should have minimal spectral shifts due to different acquisition conditions (Olthof et al., 2005; Song et al., 2001). The trained models were optimized for the number of hidden layers and units using random search hyperparameter tuning. While the model used a combination of a dropout ratio (0.2) (Srivastava et al., 2014) and a regularization (L2) parameter to prevent overfitting. Although a smaller number of samples were used, a shallow MLP with fewer hidden layers (5 and 3) and parameters [4,000-5,000] does not require thousands of samples to learn like deep neural networks. The results show that MLP with shallow architecture with smaller training samples identified and extracted redcedar with high accuracy given that the contrasting spectral (PCA, HSV, NDVI, and NDBI) and temporal (winter images) attributes were taken into consideration. For example, the redcedar showed a differing spectral pattern when using the first principal component and NDBI compared with other land cover classes (Figure 5b). Similarly, a similar

spectral pattern in the first principal components between redcedar and water differed in NDBI. Thus, the combination of multiple factors helped reduce the misclassification errors, especially in wetlands. The current method shows potential to be applied in wider spatial and temporal settings in differentiating the redcedar as well as other species of interest. However, the extracted redcedar cover also represents evergreen vegetation such as pine species as they exhibit similar spectral and temporal characteristics.

Due to redcedar occupying a small fraction (< 1%) of the study area, the stratified estimator showed a higher error of omission, especially in 1990 when the redcedar were sparsely distributed. The higher omission errors are also due to the mixed pixel effect as sparse redcedar distribution was not captured by the Landsat resolution at 30 m. Although an object with at least one-half the diameter of a pixel is detected by sensors, with radiometric, and geometric errors, along with the associated sample-scene phase, a significantly smaller pixel size (or larger object) is required to detect and resolve an object (Cowen et al., 1995; Myint et al., 2011). With the largest canopy diameter between 4-5 m, there need to be more than 10 trees for consistent representation. Studies show that the redcedar density with equal and greater than 50% has 90% or greater detection probabilities (Kaskie et al., 2019; Wang et al., 2017). Therefore, the redcedar area might be underrepresented in areas with a newer establishment or lower densities. A subpixel approaches may provide early-stage encroachment given proper identification of endmembers spectra. With changes in radiometric and spatial characteristics, esp. in historical images, sub-pixel approach has shown limitations (Quintano et al., 2012). Future research involving neural network that can learn sub-pixel structure may provide early stage encroachment (He et al., 2021). Although the images are unable to represent early-stage encroachment, they capture the moderate and significant encroachment scenarios that have higher environmental effects. A difference of 30 years (1990-2020) should compensate for some of the undetected areas in the early years. The extracted redcedar cover also represents other evergreen tree species that have similar spectral and temporal characteristics such as ponderosa pine and rocky mountain juniper even though we used winter images to reduce the influence of other land cover classes. The omission errors decreased with the inclusion of 1- and 2-pixel buffer in the classified maps, showing the effect of mixed pixels at the boundaries of maps.

A comparison of our annual encroachment rate (2.26 -11.19%) provides the spatial and temporal variation of redcedar encroachment in the study area. Our estimates are closer to the estimates of 2% by (Walker and Hoback, 2007), and encompasses 2.3% by (Filippelli et al., 2020). Some differences could be due difference in spatial and temporal coverage and removal of < 10% cover from those estimates as approximately half of the treed area lies outside of the forest in the Great Plains (Meneguzzo et al., 2018). Similarly, our estimates of redcedar cover of 4.64 % in Custer County is closer to 2% and 8.7% forest cover of the National Land Cover Database (NLCD) and Tree canopy cover (TCC) produced by US Forest Service. However, one-pixel buffer used to decrease omission error increases commission error that may

overestimate the redcedar cover and associated encroachment rate. The other difference in estimates could be due to the method used or the scale dependence of redcedar encroachment. Our results at 900 m² resolution generalizes the encroachment rate of finer scale resolution maps (Weisberg et al., 2007). Higher resolution satellite or aerial images, corrected for variation in radiometric properties, provides encroachment at finer scales (Falkowski et al., 2017). The accuracy of the extracted redcedar may have some uncertainties due to the limited availability of high-resolution images. We used the nearest available NAIP and DOQs images to define the validation points with the assumption that the redcedar coverage does not change significantly within 2-3 years at a coarser scale. However, the temporal difference might have introduced some uncertainties while selecting reference pixels. For example, the 1990 redcedar cover was validated using 1993 panchromatic images through visual interpretation. The differentiation of redcedar from deciduous trees and wetland vegetation were difficult in panchromatic images taken in growing seasons. Studies have shown that the presence of understory redcedar, dead leaves, and bark might lead to mixed pixels that are challenging to classify (Gong et al., 2012; Herold et al., 2008).

With a high annual increase rate, the redcedar encroachment will have a significant effect on the natural resources and environment of the Nebraska Sand Hills. Given the semiarid-nature and vulnerable geographic setting and the ability of the redcedar to grow under a variety of soil types and climatic conditions, redcedar will proliferate the grasslands of the Sand Hills. The current encroachment, although limited under the loess hills and nearby streams, will eventually lead to invasion. The encroachment map (regional and county scale), paired with other maps such as fire practices, topography, and soil, could help prioritize management practices.

1.5. Conclusions

The study shows that a multilayer perceptron (MLP) with multiple hidden layers and optimization provides a proper and accurate representation of redcedar encroachment. Given the proper identification of pure pixels from the winter images, a relatively smaller number of training samples also provides highly accurate maps. The study highlighted that through temporal transfer of MLP model, species distribution from historical images can be effectively identified and extracted when the training samples are limited or unavailable. With the availability of the sensor harmonization, a single MLP model should be able to extract species from multiple Landsat sensors. The unbiased estimates from sampling-based method provides spatial and temporal variation in encroachment scenarios in the study area. The encroachment range provides encroachment patterns that exists in larger areas vital for formulating proper management plans and practices.

1.6. Supplement Figure and Table
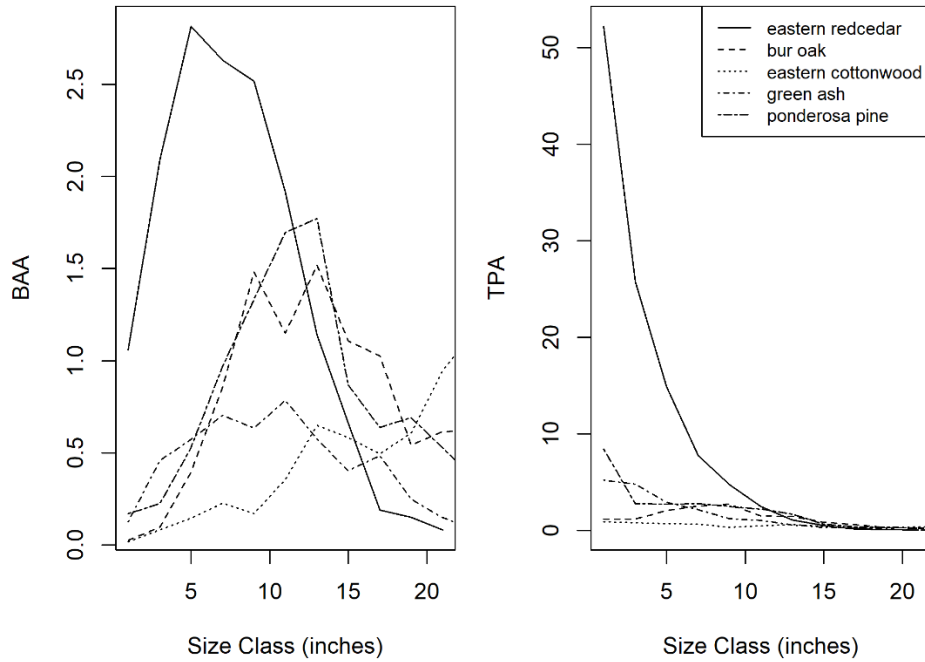
Figure 1-10. Size class distribution of basal area per acre (BAA) and tree per acre (TPA) estimates from forest inventory analysis (FIA) database in 2019 for Nebraska. Highest BAA and TPA shows redcedar as a dominant species with smaller basal area.

Table 1-2: Accuracy of random forest classifier with different number of trees

	2010							
	20 tree		50 tree		100 tree		200 tree	
Overall accuracy	0.964 (± 0.014)		0.961 (± 0.015)		0.963 (± 0.015)		0.963 (± 0.015)	
	redcedar	other	redcedar	other	redcedar	other	redcedar	other
Producer's	0.21	0.99	0.18	0.99	0.20	0.99	0.20	0.99
User's	0.91	0.96	0.91	0.96	0.91	0.96	0.91	0.96
	2020							
Overall accuracy	0.977 (± 0.012)		0.978 (± 0.011)		0.980 (± 0.011)		0.985 (± 0.009)	
Producer's	0.32	0.99	0.32	0.99	0.34	0.99	0.41	0.99
User's	0.93	0.97	0.93	0.97	0.93	0.98	0.93	0.98

Table 1-3: Error matrix for redcedar and others class with original maps, one-pixel buffer, and two-pixel buffer. The values in square brackets represent the proportion of each class in the corresponding year.

Year		Reference		One Pixel Buffer		Two Pixel Buffer		Model
		redcedar	others	redcedar	others	redcedar	others	
1990	redcedar	293 [0.002]	55 [0]	294 [0.005]	58 [0.001]	295 [0.008]	58 [0.001]	MLP
	others	4 [0.007]	566 [0.991]	3 [0.005]	563 [0.989]	2 [0.004]	563 [0.987]	
2000	redcedar	264 [0.004]	35 [0.001]	264 [0.01]	38 [0.001]	265 [0.015]	40 [0.002]	MLP
	others	2 [0.003]	598 [0.992]	2 [0.003]	595 [0.986]	1 [0.002]	593[0.981]	
2010	redcedar	275 [0.006]	28 [0.001]	276 [0.013]	33 [0.002]	276 [0.02]	37 [0.003]	MLP
	others	2 [0.003]	598 [0.99]	1 [0.002]	593 [0.983]	1 [0.002]	598 [0.976]	
	redcedar	**253 [0.008]**	**24 [0.001]**	**273 [0.019]**	**34 [0.002]**	**275 [0.028]**	**40 [0.004]**	**RF**
	others	**24 [0.038]**	**602 [0.953]**	**4 [0.007]**	**592 [0.972]**	**2 [0.003]**	**586 [0.964]**	
2020	redcedar	288 [0.008]	26 [0.001]	289 [0.019]	29 [0.002]	289 [0.028]	33 [0.003]	MLP
	others	3 [0.005]	597 [0.986]	2 [0.003]	594 [0.976]	2 [0.003]	590 [0.965]	
	redcedar	**278 [0.01]**	**19 [0.001]**	**288 [0.022]**	**26 [0.002]**	**289 [0.032]**	**31 [0.003]**	**RF**
	others	**13 [0.021]**	**604 [0.969]**	**3 [0.005]**	**597 [0.972]**	**2 [0.003]**	**592 [0.962]**	

Table 1-4: A comparison of annual redcedar encroachment rate in the study area

Interval	Annual rate of increase (%)	
	Lower	Higher
1990-2000	1.07	10.95
2000-2010	0.35	3.85
2010-2020	4.64	5.01
1990-2020	2.26	11.19

Chapter 2.   Juniperus virginiana (redcedar) encroachment assessment and prediction using Markov chain-cellular automata model in central Nebraska

2.1. Introduction

Native prairies, with range reduced by as much as 70 %, have undergone significant changes in North America since European settlements (Samson and Knopf, 1994; Samson et al., 2004). Besides direct loss, the remnant prairies are overexploited and fragmented through overgrazing, recreation activities, and proliferation of woody plants such as Eastern redcedar (*Juniperus virginiana*). For example, 8-60% of the original plant species were lost from the remnant prairie over a 32 to 52-year period in Wisconsin (Leach and Givnish, 1996). Redcedar, with a high reproductive growth, and dispersal rate, propagates even in harsh environmental conditions and thereby poses a serious threat to the lowlands and uplands grassland community (Briggs et al., 2002). A native tallgrass prairie may fully convert into a closed-canopy redcedar forest in as little as 40 years (Briggs et al., 2002). Redcedar encroachment thereby effectively alters and threatens the structure and function of the grassland ecosystem, especially in the semi-arid region vulnerable to climate change and human encroachment. For example, redcedar encroachment in grasslands can reduce groundwater recharge by two-thirds (Wine and Hendrickx, 2013), potentially altering the vast amount of recharge to High Plains Aquifer in the Nebraska Sand Hills (NSH). Nebraska occupies the largest portion of the aquifer (37% of the total area) and contributes highest recharge of up to 210 mm yr^{-1} in coarse-textured soils in the NSH(Crosbie et a l2013).The substantial increase in number, density, and volume is due to the suitable social, environmental, and ecological conditions present throughout the vast expanse of grassland in Nebraska (Meneguzzo and Liknes, 2015). The redcedar spreads quickly and inhibits other prairie species from growing as it can photosynthesize all year long and is the first to infringe on grassland, farmlands, cleared pastures, and marginal lands (Meneguzzo and Liknes, 2015). Redcedar, primarily controlled through the fire, thrive on exclusion or reduction of fire. They outcompete and establish in areas with native grassland due to intensive grazing, land degradation (Brown and Archer, 1999; Wilson and Witkowski, 1998), increased atmospheric CO_2 (Polley et al., 1997), and climate change (Briggs et al., 2002; Fowler and Konopik, 2007). It is therefore imperative to measure, monitor, and predict the spatial and temporal distribution of redcedar in the Nebraska Sand Hills.

The change in land cover at two different periods assessed through remote sensing provides spatial and temporal approximation that can predict the future distribution. Markov chain and cellular automata (Markov-CA) model computes the transition probability from two different periods to predict the future distribution. The Markov chain calculates the transition probabilities from one state to another over a specified period, while cellular automata quantify the spatial-temporal dynamics through neighborhood configuration and transition potential maps. A Markov-CA model is widely used to assess the land use and

cover dynamics (Arsanjani et al., 2011; Coppedge et al., 2007; Guan et al., 2011; Mas et al., 2014; Pontius and Malanson, 2005), especially in urban areas (Guan et al., 2011; Myint and Wang, 2006), and are also useful in forest change analysis. Balzter (2000) used the Markov chain model to assess the vegetation dynamics in grassland communities. Vázquez-Quintero et al. (2016) used the Markov-CA model to assess the forest change in Pueblo Nuevo, Mexico and found a decreasing trend in the pine forest cover. Markov-CA analysis by Kura & Beyene (2020) found that the woodland cover decreased due to human encroachment through expanding the agriculture and urban centers in southern Ethiopia. Aksoy & Kaptan (2020) used the Markov-CA model and showed a 17.4% increase in forest cover during the calibration and validation periods (1999-2019) and a 2.4% decrease during the simulation period (2019-2039). Although studies have used the Markov-CA model to estimate forest changes directly altered by human intervention such as clearing for agriculture or establishment of urban centers, few studies have used it to assess and simulate the encroachment with minimum and indirect human interventions (e.g., plantation). This study simulates the encroachment of redcedar, a dominant evergreen species occupying 90% of basal tree area in the Nebraska, especially into the grassland of the NSH.

Remote sensing provides improved estimates of the species and environmental processes required by Markov-CA models at varied spatial and temporal scales. A species with unique spatial, spectral, or temporal characteristics, can be detected using remote sensing images. Satellite images (optical and microwave), aerial photographs, light detection and ranging (LIDAR), and unmanned aerial vehicles (UAV) are widely used to characterize the state of an ecosystem such as land use and cover, vegetation structure, phenology, and the climatic conditions such as temperature, precipitation, snow, and wind. Recent studies used remote sensing to identify the species (dominant in some cases) distribution (Andrew and Ustin, 2009; Bradley, 2014; Morisette et al., 2006; Noujdina and Ustin, 2008; Peterson, 2005; Ustin et al., 2004; Weisberg et al., 2007), plant invasions (Alvarez-Taboada et al., 2017; Peerbhay et al., 2016) and potential distribution of invasive species (López and Stokes, 2016; Rocchini et al., 2015). Redcedar, one of the dominant species with unique spectral and temporal characteristics, was identified using the satellite images. Shrestha, (2021) used combination of object-based classification, MLP, and stratified random sampling to estimate the annual redcedar encroachment in the central Nebraska. The estimated encroachment rate of 2.26 -11.19% showed the spatial and temporal variation of encroachment present in central Nebraska. Wang et al. (2017) found redcedar increases by 8% annually using pixel and phenology-based algorithms on Phased Array type L-band Synthetic Aperture Radar (PALSAR) and Landsat images. Wang et al. (2018) used Phased Array type L-band Synthetic Aperture Radar (PALSAR) and Landsat images and found *Juniper Spp.* increases by 40km^2 annually. This study uses remote sensing estimates of redcedar cover derived by (Shrestha, 2022) with Markov-CA models to predict the future redcedar distribution. The specific objectives of the research are to: i) simulate the effect of different encroachment

rate on future redcedar distribution using the Markov-CA approach ii) assess and validate the accuracy of the model.

2.2. Material and methods

2.2.1. Study area and data

The study area Figure 2-1 lies in central Nebraska and covers most of the Nebraska Sand Hills. The study area ranges in latitude from 41.09 N to 42.40 N and in longitude from 102.06 W to 99.27 W covering an area of 50,671 km^2. The area comprising flat lands, dunes, Loess hills show little to strong topographical variation. Dunes present in the area consist of permeable coarse sand that promotes recharge to underlaying aquifer while sandy soil is present in the interdunal valleys (Barnes et al., 1984). The area receives an average precipitation of between 400-500mm. The mean annual temperature is 10˚C. As per the national landcover database (NLCD) of 2016 (Dewitz, 2019), the study area is dominated by grassland (84%) followed by hay/pasture (8.7%) and wetlands (4%). It consists of 0.32% of evergreen, 0.35% mixed, and 0.35% of deciduous forest. The study area was selected to cover the hotspots of redcedar encroachment in the NSH (Figure 2-1b). The southern, middle, and northern part of the study area covers less than 1 to 1-5% of redcedar live trees distribution (Meneguzzo and Liknes, 2015), signifying differing stages of redcedar encroachment. In order to simulate the various prevalent encroachment rate as estimated by (Shrestha, 2022), we used the northern, Halsey National Forest, eastern, and southern parts of study area. The Halsey National Forest area is managed forest and shows least change in area (~ 6.7 km^2) between the calibration period (1990-2010), while the southern area shows the highest changes (231 km^2). The northern area showed consistent presence of redcedar while eastern area shows newer establishment.
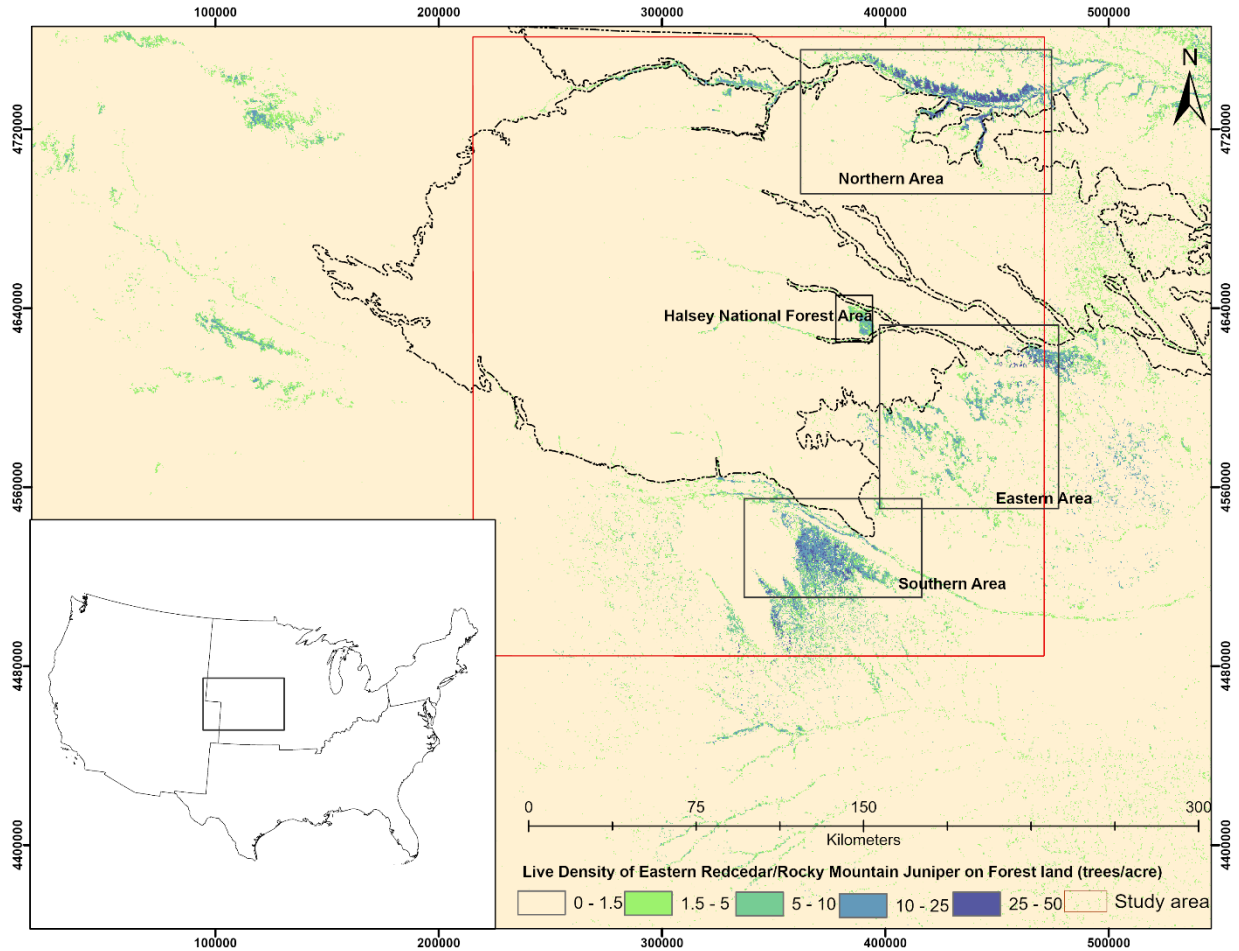
Figure 2-1. Study area (red box) showing redcedar live tree density (trees/acre) from 2005-(Meneguzzo and Liknes, 2015). Boxes show the eastern, southern, northern, and Halsey National Forest areas used for transition probability calculations.

Landsat 5 and 8 images with 30 m spatial resolution were used to extract the redcedar coverage. We used winter months (November-April) surface reflectance images with less than 30% cloud cover hosted in the Google Earth Engine (GEE). The winter months images helped to differentiate the redcedar (green vs dry/yellow leaves) from other species present in the study area. Since a limited number of snow-free images were available and the redcedar do not change significantly within 1-2 years, we used the preceding and the following years to increase the number of snow and cloud-free images (i.e., a 1990 mosaic contains images from 1989 and 1991) and reduce the uncertainties caused by the data availability.

The driver variables used to determine the redcedar occurrence and distribution were based on morphological factors rather than biological factors such as competition. A digital elevtion model (DEM) with 30 m resolution National Elevation Dataset (NED) was used to derive the morphological variables. The effect of redcedar distribution by geomorphology of an area were represented by aspect, topographic position index, total insolation, duration of insolation, and wind spreadness derived using the System for Automated Geoscientific Analyses (SAGA) (Conrad et al., 2015). The topographic position index shows

34

whether a topography is higher, lower, or flat when compared with surrounding features. Total insolation shows the incoming radiation determined by the elevation, slope, and aspect under clear sky conditions that determine whether redcedar favors high or low insolation areas. The wind spreadness index shows whether an area is shadowed or exposed to wind from all possible wind directions representing possible spreadness of redcedar seeds. Since redcedar were primarily introduced as windbreaks in the Midwest, we digitized windbreaks using visual interpretation of 2020 NAIP images. The distance to windbreak was derived using Euclidian distance. Assuming redcedar are able to thrive in semiarid region with excess to deeper soil moisture, we derived distance to the water table from the gSSURGO database (Soil Survey, 2021). Distance to stream and distance to road network were derived as the redcedar mainly occurred along the stream channels. The road network was included with assumption that it facilitated the windbreaks and seedling distribution during transportation.

2.3. Redcedar encroachment assessment

Shrestha et. al., (2022) used a multi-layer perceptron (MLP) with multiple hidden layers, regularization, and dropout ratio to identify and extract the redcedar from Landsat 5 and 8 images. Each of Landsat 8 (L8-MLP) and Landsat 5 (L5-MLP) model were trained using pure pixels collected and visually identified after object-based classification of NAIP images. The classified images were stratified randomly sampled to estimate the redcedar cover and associated uncertainty. Redcedar Details on redcedar extraction, area estimates, and validation is provided in Shrestha et. al., (2022).
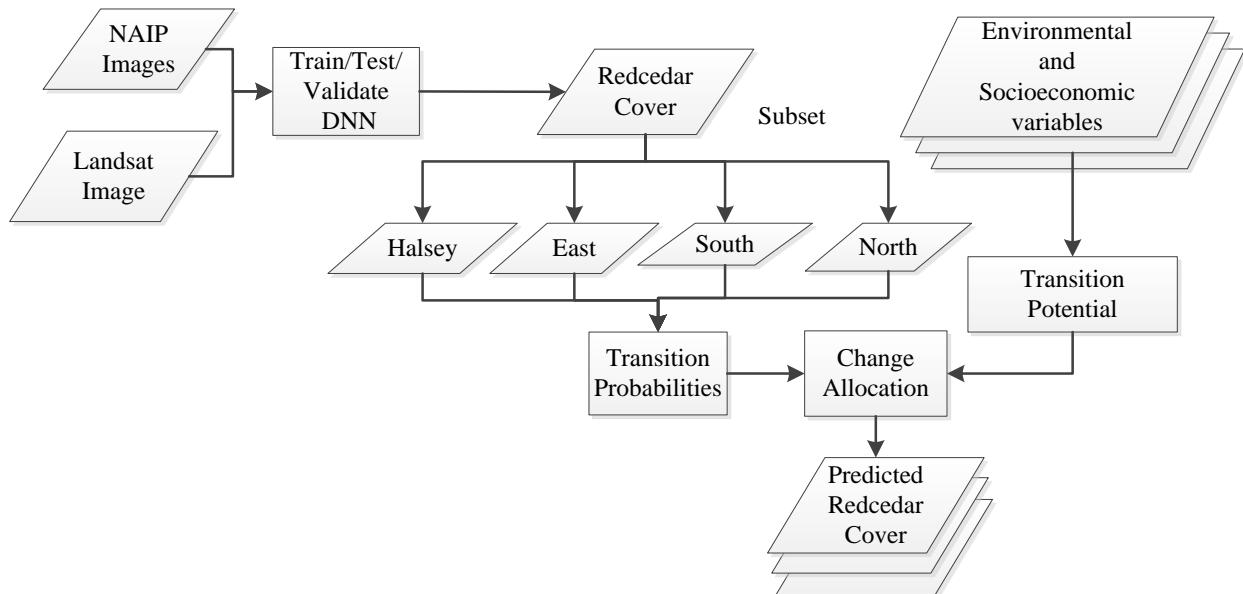
Figure 2-2: Workflow to determine and predict the redcedar distribution in the study area.

2.4. Markov chain cellular automata (Markov-CA) model

Markov model provides the probability of transition of a pixel from one category to another at every time step, as a stochastic process. The future state of a pixel is only related to its immediately preceding state but not to any other previous state. As the Markov process is independent of neighboring pixels, the cellular automata define the spatial dynamics and allow the influence of the neighboring pixels during prediction (Eastman et al., 2005). Markov-CA model combines the temporal and spatial components to assess and predict change in the state of pixels. The Markov-CA model involves computation of i) transition probabilities, ii) transition potential, and, iii) spatial allocation of simulated land use/cover probabilities. We used the Land change modeler (LCM) module in IDRISI Terrset to analyze the redcedar encroachment (Eastman et al., 2005). We tested the model simulation for equal interval and unequal interval time periods. The simulation with equal calibration (1990-2005) and validation (2005-2020) duration showed lower agreement in location and quantity, therefore, was removed from the analysis. The study, therefore, uses the 1990-2010 to calibrate and the 2010-2020 period to validate the simulation results.

The transition probability between two dates is analyzed using the Markov chain probability approach. The transition matrix for the period between 1990 (t_0) and 2010 (t_1) ($t_1 = t_0 + T)$ is obtained by overlaying the two redcedar cover maps at t_0 and t_1. This matrix indicates the area (or the number of pixels) for each transition and forms the basis for projecting to a future date. We estimated transition probabilities of differing encroachment scenarios present in the study area. For example, the transition probabilities from the Halsey National Forest, which is the largest human planted forest in the United States that undergoes various management practices such as prescribed fire, logging, and herbicides represent the effect of management practices and human influence in redcedar encroachment.

The transition potential map is produced using the MLP neural network. MLP learns the complex relationship between the variables. The change in the area between the two dates is the dependent variable, while the driver of change is the independent variable. The independent variables were determined from the factors that facilitate the redcedar growth and distribution. We used morphometric (elevation, aspect, topographic position index, total insolation, duration of insolation, and wind spreadness) and social-environmental (distance to road, distance to windbreak, distance to stream, and depth to water table) variables described in section 2.1.

The hyperparameters of MLP such as number of nodes in the hidden layer was determined by iteratively running the algorithm with a different number of nodes. The increase in the number of nodes greater than 10 did not significantly increase the accuracy, therefore, we selected 10 nodes to determine the transition potential (Figure 2-3). The optimum learning rate was automatically determined by the algorithm while the sigmoid constant and momentum factors were made constant. The accuracy rate is the comparison between

the simulated and test data sets. Skill measure provides the difference between the measurement accuracy and expected accuracy by chance.
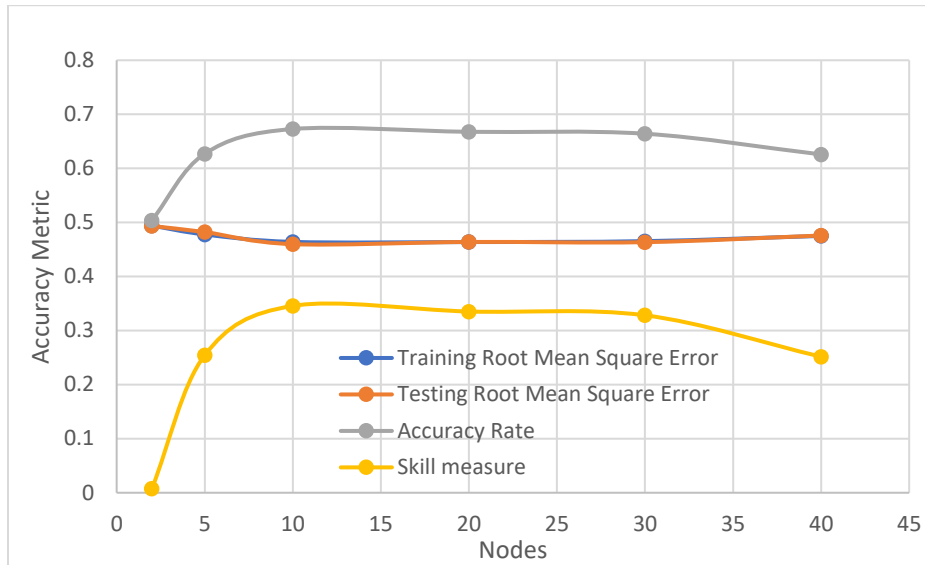
Figure 2-3: Accuracy metrics for determining number of nodes of multi-layer perceptron used for transition potential

2.4.1. Spatial allocation

The future redcedar cover is simulated based on the a) redcedar cover map, b) transition potential maps, and c) transition area matrix using the multi-objective land allocation (MOLA) algorithm. The MOLA in the LCM allocates change at the highest-ranking pixels in the transition potential maps (Camacho Olmedo et al., 2013; Eastman and Toledano, 2018). Any conflict during change allocation in MOLA procedure is resolved based on a minimum-distance-to-ideal-point rule using the weighted ranks (Houet and Hubert-Moy, 2006). A new patch is generated when the independent variables produce disjoint patches with high transition potential (Mas et al., 2014). The transition area matrix derived from the Markov chain analysis determines how much land is allocated to a class over the *n*-year period (Myint and Wang, 2006). At the end of each iteration, a new land use/cover map is generated by overlaying all results of the MOLA procedure.

2.4.2. Validation of Markov-CA

The Markov-CA model predicted redcedar cover for 2020 is validated against the classified Landsat images for 2020 using Kappa variations. Two maps with common categories can be compared along with the components of agreement (agreement due to chance, quantity, and location) and disagreement (disagreement due to location and quantity) in terms of quantity and location of each category. The component of agreement is the proportion of pixels classified correctly while the component of disagreement is the proportion of pixels classified incorrectly (Pontius and Spencer, 2005). Kappa variations measure the goodness of fit between predicted and reference maps and corrects for accuracy by

chance (Bishop et al., 1975). It includes traditional Kappa ($K_{standard}$), Kappa for no information/ability (K_{no}), Kappa for location ($K_{location}$) and Kappa for quantity (Kquantity). The information on quantity is donated by bold letters: **n**-no information, **m**-medium information, and **p**-perfect information. Information of location is represented by capital letters: N-no information, M-medium information and, P-perfect information. A detailed explanation is provided by (Pontius et al., 2004).

$$K_{no} = (M(\boldsymbol{m})N(\boldsymbol{n}))/(P(\boldsymbol{p}) - N(\boldsymbol{n}))$$

$$K_{location} = (M(\boldsymbol{m})N(\boldsymbol{n}))/(P(\boldsymbol{m}) - N(\boldsymbol{m}))$$

$$K_{quantity} = (M(\boldsymbol{m})H(\boldsymbol{m}))/(K(\boldsymbol{m}) - H(\boldsymbol{m}))$$

$$K_{standard} = (M(\boldsymbol{m})N(\boldsymbol{n}))/(P(\boldsymbol{p}) - N(\boldsymbol{m}))$$

K_{no} indicates the overall correct proportion relative to the expected proportion classified correctly by simulation while, $K_{location}$ and $K_{quantity}$ measures the validation between the actual and simulated maps based on location and quantity respectively (Pontius and Malanson, 2005; Pontius and Schneider, 2001). A value of one indicates perfect agreement and a value of zero means unsatisfactory or imperfect agreement (Pontius and Schneider, 2001).

2.5. Results

2.5.1. Image classification accuracy

The results show high overall and user's accuracy (Table 2-1). The producer's accuracy is low due to presence of mixed pixels esp. in 1990 when the redcedar were at early stage of encroachment. The results also highlight the effect of class weight in stratified random estimator leading to higher omission errors. The producer's accuracy increased when the classified maps were buffered by one (30 m) and two pixels (60 m). To balance the proper representation of the redcedar cover and the accuracy of maps, we chose the one pixel buffered map for further analysis. Using no buffer can underestimate redcedar coverage while a two-pixel buffer may overestimate the coverage.

Table 2-1: Producer's and user's accuracy metrics for redcedar in 1990, 2010, and 2020 (Shrestha, 2022).

Labels	Original		One Pixel Buffer		Two Pixel Buffer	
	1990					
Property/Strata	redcedar	others	redcedar	others	redcedar	others
Overall accuracy (± 95% CI)	0.993(±0.007)		0.994(±0.006)		0.995(±0.005)	
Producer's accuracy	0.21	1.00	0.47	1.00	0.69	1.00
User's accuracy	0.84	0.99	0.84	1.00	0.84	1.00
	2010					
Overall accuracy (± 95% CI)	0.996(±0.005)		0.997(±0.003)		0.996(±0.003)	
Producer's accuracy	0.64	1.00	0.89	1.00	0.92	1.00

User's accuracy	0.91	1.00	0.89	1.00	0.88	1.00
	2020					
Overall accuracy (± 95% CI)	0.994(±0.006)		0.995(±0.005)		0.993(±0.005)	
Producer's accuracy	0.63	1.00	0.85	1.00	0.90	1.00
User's accuracy	0.92	1.00	0.91	1.00	0.90	1.00

2.5.2. Markov chain – Cellular automata

The Markov-CA model was used to derive the transition probabilities, transition potential, and change allocation.

2.5.3. Redcedar transition probabilities and potentials

The transition probabilities calculated in the north, east, south, and Halsey Forest areas show differing transition probabilities for 2020, 2050, and 2100 (Table 2-2). The northern and southern areas show higher persistence in redcedar cover than the eastern and Halsey National Forest areas. The transition probabilities of others to redcedar are high in the eastern and Halsey National Forest area leading to a consistent reduction in redcedar area in future simulation years. The difference in transition probabilities of redcedar to others and others to redcedar is less in northern and southern areas. A balanced redcedar transition probabilities (redcedar to others Vs others to redcedar) and area estimate closer to the stratified random estimate (Table 2), we assume that the northern area transition probabilities provide best estimate of redcedar encroachment.

Table 2-2: Transition probabilities between redcedar and others class in eastern, Halsey National Forest, northern, and southern areas in 2020, 2050, and 2100. redcedar cover (area) for 2020 is calculated in km2 in equal area projection system.

	Simulation year					
	2020		2050		2100	
Landcover	Eastern Area					
	redcedar	others	redcedar	others	redcedar	others
redcedar	0.9037	0.0963	0.6721	0.3279	0.4291	0.5709
others	0.0136	0.9864	0.0461	0.9539	0.0803	0.9197
Area (km^2)	1676.87	56451.25	-	-	-	-
	Halsey National Forest					
redcedar	0.8985	0.1015	0.6659	0.3341	0.4463	0.5537
others	0.0317	0.9683	0.1044	0.8956	0.173	0.827
Area (km^2)	2706.06	55422.05	-	-	-	-
	Northern					
redcedar	0.9718	0.0282	0.894	0.106	0.7849	0.2151

others	0.014	0.986	0.0527	0.9473	0.1069	0.8931
Area (km^2)	1767.51	56360.61	-	-	-	-
Southern						
redcedar	0.959	0.041	0.8535	0.1465	0.7253	0.2747
others	0.0353	0.9647	0.1263	0.8737	0.2368	0.7632
Area (km^2)	2972.09	55156.03	-	-	-	-
Reference (Stratified sampling)						
Area (km^2)	1521.47	67228.66	-	-	-	-
CI	316.09	316.09	-	-	-	-

We used ten independent variables to derive the transition potential map. The most influential variables are the duration of insolation followed by depth to the water table and total insolation. The least influential variables are distance to windbreak and distance roads. The MLP used to determine the transition potential although learns complex, non-linear association and interaction among variables, the most influential variables may not relate to expectations in the real world. For example (Table 2-3), the distance to windbreak is the least influential while it could be one of the important variables in the redcedar invasion.

Table 2-3: Sensitivity analysis of independent variables for transition potential calculation.

Variables	Model	Accuracy (%)	Skill measure	Influence order
With all variables	With all variables	86.69	0.73	N/A
Aspect	constant	86.62	0.73	7
Wind exposition	constant	84.27	0.69	4
Topographic position index	constant	86.41	0.73	6
Total insolation	constant	82.46	0.65	3
Duration of insolation	constant	81.35	0.63	1 (most influential)
Depth to water table	constant	81.70	0.63	2
Distance to road	constant	86.67	0.73	8
Distance to stream	constant	85.86	0.72	5
Distance to windbreak	constant	86.80	0.74	9 (least influential)

2.5.4. Model validation

The simulated redcedar cover for 2020 was compared with the classified redcedar (reference) cover from 2020. The Kappa variation (Table 2-4) show that the reference and simulated maps match with each other

better than chance and can be used to simulate the future distribution of redcedar. Table 4 compares the agreement and disagreement between reference and simulated maps at the eastern, northern, southern, and Halsey National Forest areas. The northern and eastern area showed similar agreement due to quantity, location and Kapps variation than the southern and Halsey National Forest. Some statistics are better in northern area such as disagreement due to grid cell, Kstandard, Klocation and KlocationStrata. The northern area showed total disagreement less than 3% of which disagreement due to quantity is less than 1% and disagreement due to grid cell is less than 2%.

Table 2-4: Validation statistics for reference and simulated redcedar cover for 2020. The Kappa variation (Kno, Klocation, KlocationStrata, and Kstandard) shows the simulation is better than chance based on location, quantity, and traditional Kappa statistics.

Category	Information			
	North	South	East	Halsey
Agreement due to chance	0.50	0.50	0.50	0.50
Agreement due to quantity	0.45	0.43	0.45	0.43
Agreement Strata	0.00	0.00	0.00	0.00
Agreement Gridcell	0.03	0.03	0.03	0.03
Disagree Gridcell	0.01	0.01	0.01	0.01
Disagreement Strata	0. 00	0. 00	0. 00	0. 00
Disagreement due to quantity	0.01	0.03	0.01	0.02
Kno	0.96	0.92	0.96	0.93
Klocation	0.70	0.76	0.66	0.71
KlocationStrata	0.70	0.76	0.66	0.71
Kstandard	0.59	0.45	0.57	0.45

The validation image (Figure 2-4 a, b, c) shows that most of the areas match each other. Areas that are altered due to human intervention (e.g., forest fire), are missed, or underrepresented in the simulation. Any landscape changed after the calibration period (1990-2010), is not properly represented. For example (Figure 2-4 c -north west part), a forest fire in 2012 in the northern part of the study area is over-predicted in the simulated redcedar cover.
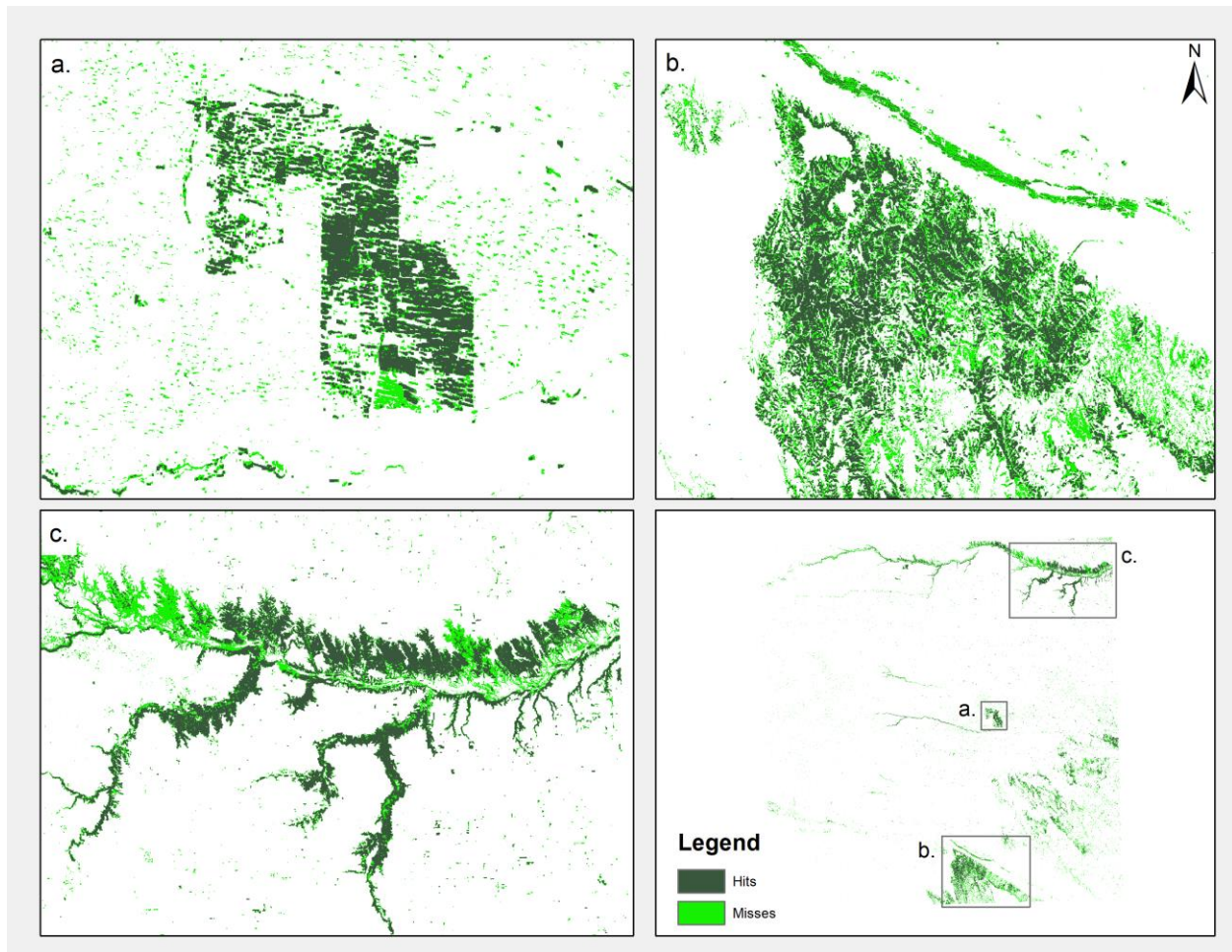
Figure 2-4: Validation map using northern transition probabilities between the reference and simulated 2020 redcedar cover for a. Halsey National Forest; b. southern and; c. northern area.

2.5.5. Predicted redcedar cover

The redcedar cover is predicted for 2050 and 2100 using 2020 as a base map, transition probability matrix, and transition potential maps. The predicted redcedar cover shows temporal patterns in the redcedar distribution. The difference in transition probabilities has resulted in various scenarios of redcedar encroachment. The eastern area transition probabilities resulted in the lowest increase in redcedar area while the southern area transition probabilities resulted in the highest increase (Figure 2-5). The redcedar area calculated using transition probabilities of Halsey National Forest resulted in high increase in redcedar than anticipated. The transition probabilities of northern area predicted redcedar cover increased by more than two-fold (3899 km^2) in 2050 and four-fold (6887 km^2) in 2100 when compared with an area of 1767 km^2 in 2020.
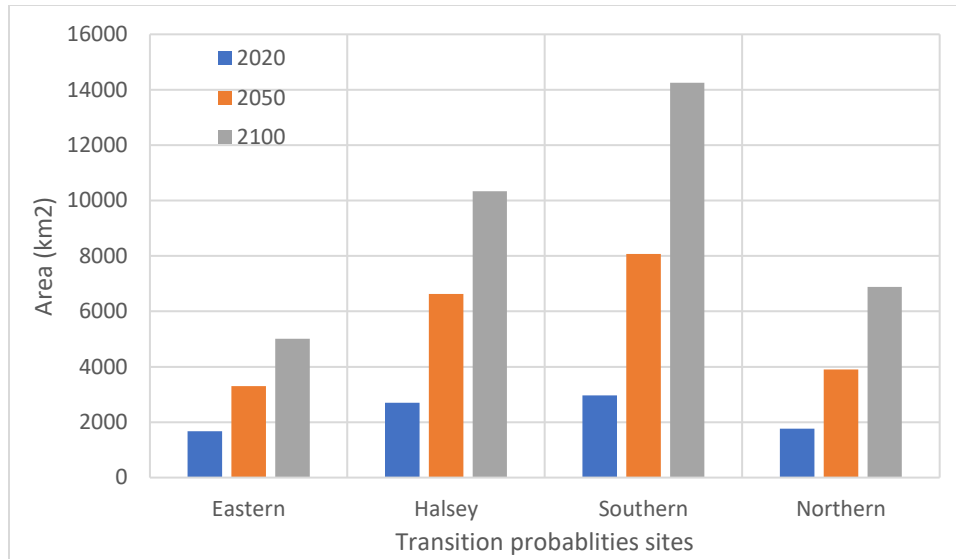
Figure 2-5: Simulated redcedar area using transition probabilities calculated from the eastern, Halsey National Forest, Southern, and Northern area.

The results of the eastern, Halsey National Forest, northern and southern areas transition probabilities also showed a substantial spatial variation in encroachment patterns. The Halsey National Forest decayed in all of the simulation, while the northern and southern area showed increase in redcedar density and cover, esp. using southern area transition probabilities (Figure 2-9). Eastern area transition probabilities resulted in least dense redcedar distribution (Figure 2-7) compared to Halsey National Forest (Figure 2-8) and southern area (Figure 2-9). While considering the northern area transition probabilities more realistic, the Figure 2-6 shows increase in redcedar cover and density in the northern (Figure 2-6 d, e, f) and southern (Figure 2-6 g, h, i) parts of the study area while the Halsey National Forest shows a decrease and ultimately vanishing of redcedar cover (Figure 2-6 a, b, c) and (Figure 2-7, Figure 2-8, Figure 2-9). The potential reason could be the transition potential map showing the Halsey National Forest unsuitable for redcedar as determined by the driving factors estimated using the MLP method. The transition probabilities using Halsey National Forest showed the least persistence and thus showed anticipated decay over the simulation in a longer time. Although Halsey National Forest decayed over time, the surrounding area showed increased redcedar cover or showed newer encroachment areas. While the encroachment was confined within the boundaries defined by topography in the northern and southern areas. The results could be used as potential redcedar distribution with highest (southern area), lowest (eastern area), and moderate (northern area) encroachment scenarios.
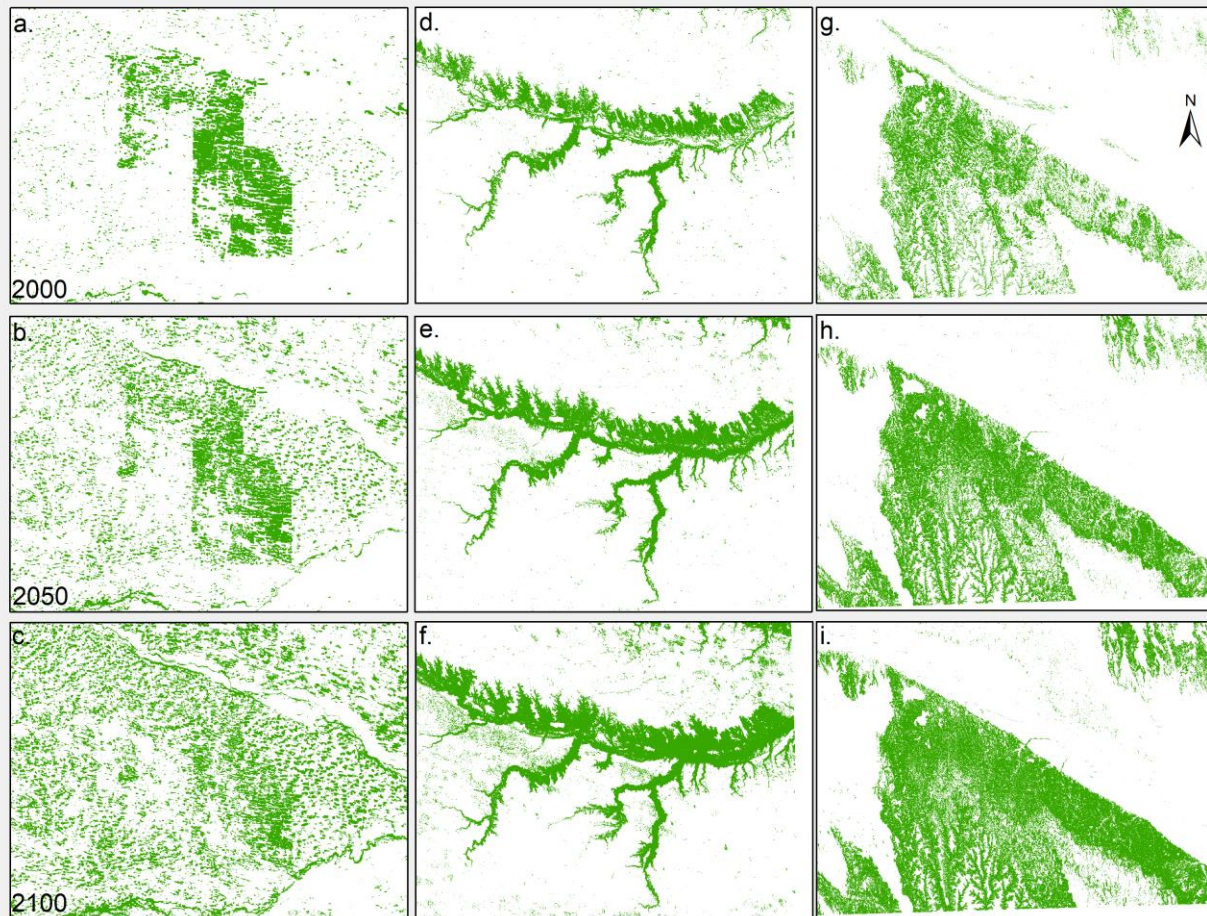
Figure 2-6: A comparison between the predicted redcedar for 2000, 2050, and 2100. redcedar coverage decreased in the Halsey National Forest area (a-c); increased in northern (d-f) and southern (g-i) part of the study area.

2.6. Discussion

The accuracy of the simulated redcedar encroachment depends entirely on the accuracy of the input maps. Although winter images were used to facilitate the differentiation of evergreen trees from mixed forests and wetlands with vegetation, the overlapping spectral signature (e.g., the presence of redcedar as understory vegetation in the mixed forest) resulted in an error of omission and commission. The use of one-pixel buffered maps in analysis reduced effect of omission errors but may include effect of increasing commission error. The representation of redcedar, however, is limited due to the spatial resolution of the Landsat images. With radiometric and geometric errors, and associated sample-scene phase, a 30 m pixel resolution does not consistently detect and resolve at least one-half the diameter of the smallest object of interest as described in the literature (Cowen et al., 1995; Myint et al., 2011). With an average tree canopy diameter of 1.2-12 m (Bechtold, 2003), a minimum of three to twenty trees must be present for detection and delineation of redcedar. Therefore, the redcedar cover might be underrepresented in areas with the newer establishment. Although the images are unable to represent early-stage encroachment, they capture the

moderate and significant encroachment that has higher environmental effects. A difference of 20 years (1990-2010) should compensate for some of the undetected areas.

The Markov-CA model is a simple and effective approach to assessing and predicting the landcover change and encroachment analysis. The higher Kappa coefficient suggests that the model can capture the variation better than chance and can be used for further analysis. The output from the Markov-CA model is governed by the transition probabilities and transition potentials. To ensure natural encroachment, we calculated transition probabilities using a subset of locations with different redcedar encroachment. The eastern area resulted in smallest increase while the southern area showed largest increase in redcedar encroachment. The approach provides multiple encroachment scenarios that can help decision makers on formulating management strategies. It also provides input maps for various simulation models such as hydrological modelling to evaluate the effect of encroachment in discharge, groundwater recharge, and evapotranspiration. The results show that the output of the simulation is sensitive to the base images used to derive the transition probabilities and area matrices (Sinha and Kumar, 2013). The transition potentials, however, were calculated using the social-environmental (distance to road, distance to windbreak, distance to stream, and depth to water table) and morphometric (elevation, aspect, topographic position index, total insolation, duration of insolation, and wind spreadness) variables. The soil and its associated properties were excluded as they do not vary much in the NSH.

The difference in validation between the simulated and reference redcedar cover for 2020 could be inherently associated with the limitation of the Markov chain approach. Other models such as species distribution model, machine learning, could possibly be used albeit with their own limitations and strengths. The Markov chain assumes the change process to be stationary over time while in reality the change is governed by the dynamic interaction of socio-economic and biophysical factors and is therefore non-stationary (Eastman et al., 2005; Pérez-Vega et al., 2012; Sinha and Kumar, 2013). As such the transition probabilities vary over time and carry the non-stationarity property in the prediction leading to a mismatch with the reference redcedar cover. Similarly, the dependence of the Markov chain on the immediately previous state rather than on the sequence of states might underestimate the importance of the historical event in change analysis and prediction (Eastman et al., 2005; Sinha and Kumar, 2013; Staver et al., 2011). Some differences in the result of simulated redcedar cover could be due to the transition between categories at a smaller proportion of the study area (Pontius and Petrova, 2010) and difference in growth rate or transition between two time periods that results in systematic errors (Camacho Olmedo et al., 2015; Pontius and Neeti, 2010). A transition rate between 1990-2010 might be different than the transition between 2010-2020. The results show that areas with significant land cover change due to human intervention such as fire, conversion of land to agriculture, planting redcedar for wind breaks, or other developmental practices, are not well represented in the simulated redcedar cover. Implementation of human intervention in the model

will help to address such problems. The use of prescribed burns is increasing in the Great Plains with formulations of burn cooperative that allows or circumvents state policies that forbid burns when wildfire danger is increased (Twidwell et al., 2013).

The simulated map of future redcedar distribution provides the spatial and temporal dimension of encroachment that enables decision-makers to formulate better-informed management plans and practices. With considerable changes in the ecosystem function and services in the prairies due to encroachment, the scenarios also provide an opportunity to localize and regulate redcedar distribution. Although the model used socio-environmental and morphometric variables, incorporation of edaphic and other change-inducing variables (e.g., social and economic) may improve prediction.

2.7. Conclusions

The study shows that the redcedar encroachment can be assessed using the multi-layer perceptron using Landsat images. The high accuracy of the extracted redcedar shows that the method provides reliable estimates of redcedar cover at a regional scale. Although the images do not provide sufficient resolution to map early-stage encroachment, the results capture the significant encroachment. The Markov chain cellular automata model provides a simple and effective way to incorporate transition between the redcedar and others land cover and predict the future distribution of the redcedar. The subset of study area (eastern, northern, Halsey National Forest, and southern) showed differing transition probabilities that resulted in variation in spatial and temporal patterns of redcedar encroachment. The southern area transition probabilities resulted in the highest increase in encroachment while the eastern area transition probabilities showed lowest encroachment. The northern area model results showed that redcedar cover increased by four-fold in 2100 compared to 2020. The result can be used to simulate the effect of redcedar encroachment in different biophysical modeling environments that helps in the formulation of an effective management plan.

2.8. Supplementary materials
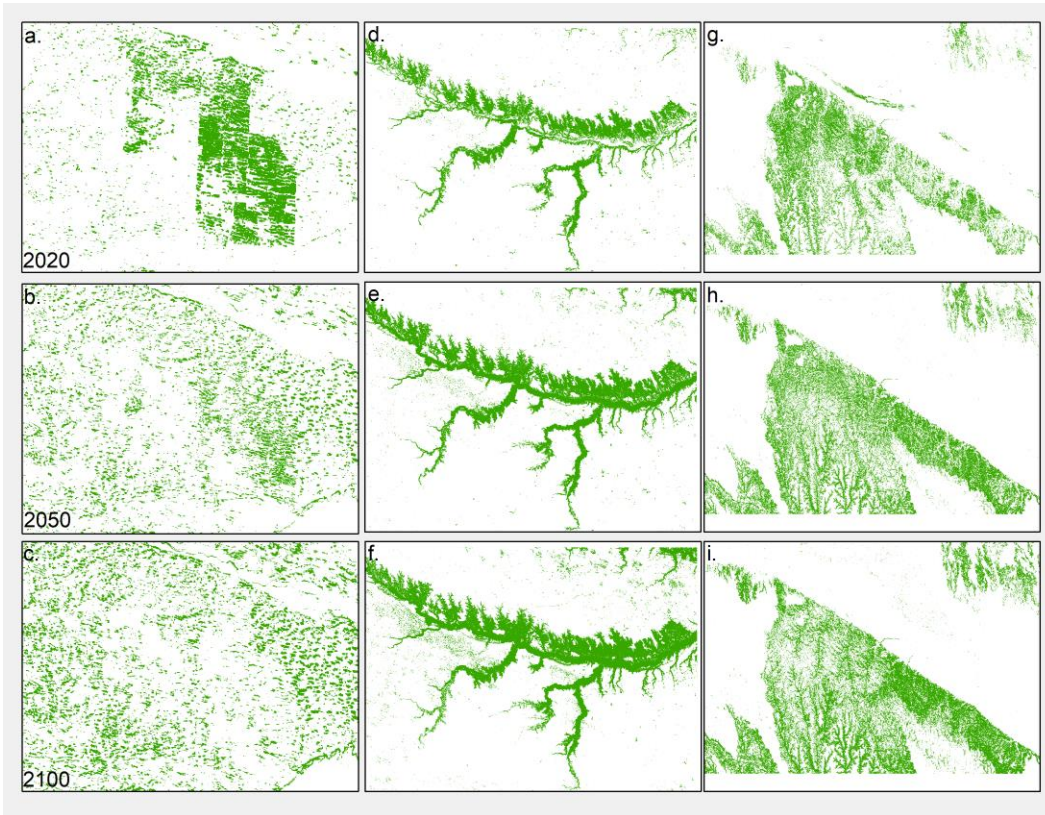
Figure 2-7: Simulated redcedar cover for 2020, 2050, and 2100 using the eastern area transition probabilities
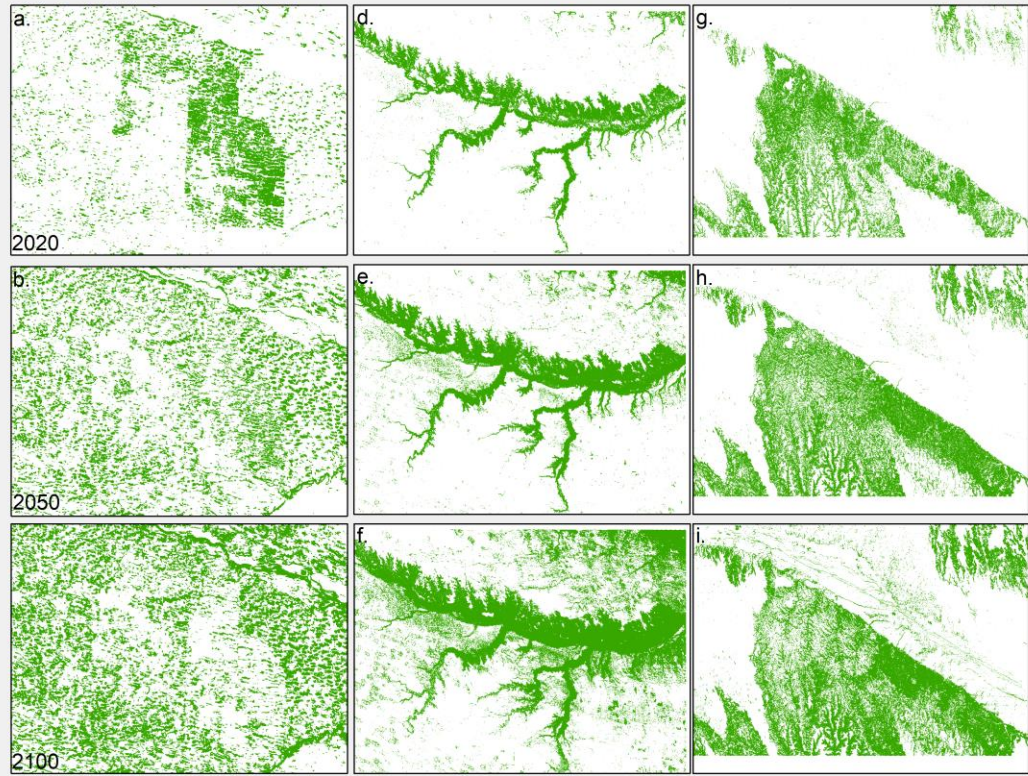
Figure 2-8: Simulated redcedar cover for 2020, 2050, and 2100 using the Halsey National Forest area transition probabilities.
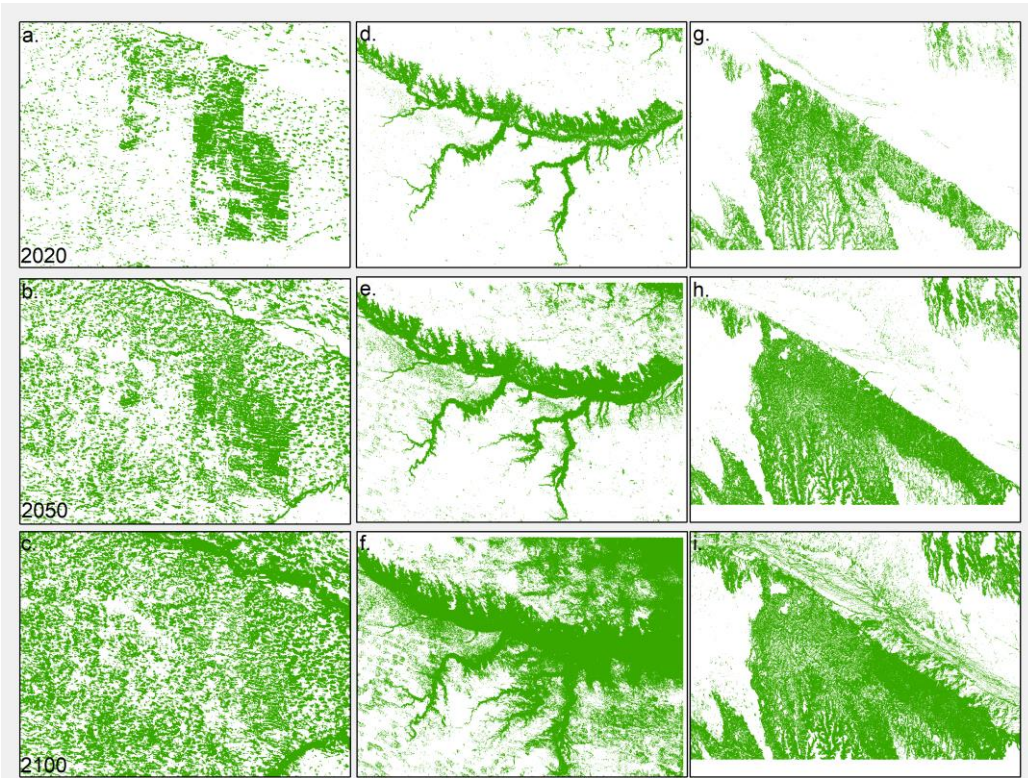
Figure 2-9: Simulated redcedar cover for 2020, 2050, and 2100 using the southern area transition probabilities.

Chapter 3. Impact of Eastern Redcedar encroachment on water resources in the Nebraska Sandhills

3.1. Introduction

Globally, grasslands are shifting rapidly to woody-plant dominance (Anadón et al., 2014b; Eldridge et al., 2011; Zou et al., 2014). This phenomenon is known as woody-plant encroachment and is driving important changes in hydrological function in biodiversity and productivity, biophysical changes, and related social costs (Huxman et al., 2005; Schreiner-McGraw et al., 2020).

One of the most notorious species encroaching into grasslands in North America is Eastern Redcedar (ERC) (Engle et al., 2008; Fogarty et al., 2020; Twidwell et al., 2013). ERC (Juniperus Virginiana) is native to North America but historically limited in abundance due to fire (Axmann and Knapp, 1993). ERC is considered the most widely distributed conifer species in North America (Ferguson et al., 1968). The range of ERC spans from eastern North America to southeastern parts of Canada down to the southern parts of the United States (U.S.) at the Gulf of Mexico and it expands towards the eastern Great Plains (Gilman and Watson, 1993; Oklahoma Conservation Commission, 2008). Meneguzzo and Liknes (2015) found that ERC has increased range from the eastern coasts of the U.S. to the Midwest states reaching as far as western Nebraska. They concluded that the ERC geographic distribution in the central U.S. is considered widespread, with the most significant increases occurring in Nebraska and Missouri during the early 2000s.

Several studies quantified the ERC encroachment in Nebraska, including the Nebraska Sandhills (NSH), the principle recharge area for the High Plains Aquifer (Adane et al., 2017; Adane and Gates, 2014; Awada et al., 2013). According to Walker and Hoback (2007), the rate of ERC encroachment was 2% annually, and in the past 30 years, the coverage has increased to 30% in the Loess Canyons in southeastern Lincoln County in Nebraska. In the last 20 years, ERC has noticeably increased from 10,000 to 300,000 trees (30 times) in the NSH (Nebraska Forest Service, 2016).

The impacts of ERC encroachment in Nebraska have been evaluated by scientists since the beginning of the 20th century. According to Bielski et al., (2017)http://cedarliteracy.unl.edu/, the impact of ERC on soil was documented in the 1940s, the impact on livestock production in the 1970s, and recently the impact on society. The impacts can be categorized into social costs, changes in biodiversity and productivity and biophysical changes. ERC control costs for public schools (or land in related trusts), a social cost, have increased by $250,000 since 2006 and livestock production has decreased by 75% in areas with substantial ERC encroachment on grasslands. Wildfire risk has shifted from frequent grass-driven fires to infrequent juniper driven crown fires with longer flames (Bielski et al., 2017)http://cedarliteracy.unl.edu/. Biodiversity and productivity impacted different species. For example, grassland birds and prairie chickens have been replaced by woodland/shrubland birds in areas with more than 10% encroachment. ERC canopy allows very few plants to grow underneath. The richness of grassland species declined by 88% in ERC

encroached areas. The abundance of beetle species is reduced in a similar manner as small mammal species, and most of these species are no longer present in areas encroached by more than 30%. Finally, the biophysical impacts include carbon storage shifts from beneath grasslands (96%) to above ground in ERC (52%). Due to this shift to aboveground storage, there is an increased potential for rapid losses of carbon due to disturbance factors such as drought, wildfire, disease, or insect outbreaks in the encroached areas (Bielski et al., 2017).

Multiple studies have evaluated the impacts of ERC on water resources. To understand the extent of ERC encroachment and its implications to evapotranspiration (ET), surface runoff and infiltration, Zou et al. (2018) reviewed the impacts of ERC proliferation on water resources in the U.S. Great Plains. The study concluded that watersheds with ERC encroachment have increased ET and precipitation loss to canopy interception. This leads to soil moisture depletion and reductions in surface runoff and deep recharge. A study by Wine and Hendrickx (2013) investigated the bio-hydrologic effects of ERC encroachment into Oklahoma grassland. The study found that the average ET from grassland and ERC was 787 mm (95% of precipitation) and 798 mm (97% of precipitation), respectively. Another study by Zou et al. (2010) examined how ERC encroachment would impact the water cycle in Oklahoma rangelands. They concluded that evaporation, transpiration, and subsurface flow increase while water storage, groundwater recharge, and baseflow decrease because of the encroachment. A study by Adane et al. (2018) investigated the impacts of grassland conversion to dense pine forest on the water budget in the NSH; however, past studies did not evaluate the impacts of ERC encroachment on the water resources in the NSH.

The impacts of ERC encroachment on water resources in Nebraska, specifically in the NSH, are significant for multiple reasons. First, the Sandhills is one of the last remaining intact prairie regions in the world and has only recently begun to experience woody encroachment (Fogarty et al., 2020). Second, landscape transformation (from rangeland to ERC) is believed to reduce groundwater recharge and discharge to the stream system, however, the extent of ERC encroachment and its effect on the hydrologic functioning of NSH's hydrology are still unknown. Lastly, the Loup River, which drains the NSH, is a major tributary to the Platte River, a vital waterway for Nebraska. Understanding the hydrological impacts of ERC encroachment will play an important role in the sustainability of the High Plains Aquifer and the Nebraska rivers and ecosystems. Studies in the past have evaluated different characteristics of this area related to hydrology, geology, agriculture, and climate. For example, Gosselin et al. (2006) performed a study on the hydrological effects and groundwater fluctuations in NSH. The study employed simple water balance approach estimating ET from water levels. They found that groundwater level fluctuations in the wet meadow are strongly linked to the seasonal growth patterns of vegetation, but it was limited to areas where the groundwater table was within the rooting zone. It was found that the average ET ranged between 5-6 mm/day in mid-growing season and 2-3 mm/day during the period of senescence.

In this study, we use the Soil and Water Assessment Tool (SWAT) to model the impacts of ERC encroachment on recharge and discharge at the watershed scale within the NSH. Few studies have applied the SWAT model to evaluate the impacts of ERC on water resources (Qiao et al., 2015; Starks and Moriasi, 2017). Starks and Moriasi (2017) conducted a modeling study in the central reach of the North Canadian River basin in central Oklahoma. The model was used to simulate an encroachment of ERC into grasslands by 10% increments and assess its impacts on the stream discharge. They found that if rangeland was replaced by ERC completely (100% encroachment), a reduction in stream discharge could reach 112% of the current municipal water demand and 89% of the projected 2060 demand. This was supported by Zou et al. (2018), where they assessed the impacts of ERC proliferation on water resources in the Great Plains, U.S. using the SWAT model. They found that a complete conversion from rangeland to ERC would result in a reduction in streamflow throughout the year between 20 to 40% depending on the aridity of the climate. None of these studies evaluated the impact of ERC encroachment on water quality, a recommended topic for future research identified by Zou et al (2018). The objectives of this study were to evaluate the (1) impacts of the current and future ERC encroachments on the recharge and discharge in the NSH and (2) implications of ERC encroachment on the water quantity and quality in the Platte River, a vital river in Nebraska.

3.2. Methods

3.2.1. Study Area

The Nebraska Sandhills (NSH) is an area of vegetated sand dunes located in central to western Nebraska with a total area of approximately 50,000 km^2 (Ahlbrandt and Fryberger, 1980; Smith, 1965; Sweeney and Loope, 2001). It consists mainly of interdunal basins, connected with an unconfined aquifer, and hosts around 4,700 lakes and over 2,000 km^2 of wetlands (Dappen et al., 2007). The climate in the NSH is semiarid, with annual precipitation ranging from 406 mm (west) to 610 mm (east) and an average temperature of 8.9°C (Ahlbrandt and Fryberger, 1980). Most of the land cover (93% of total watershed area) is herbaceous (Pasture), 4.2% as wetlands, 1% as lakes, 0.7% urban land, 0.44 red cedar, and 0.23 corn fields based on the NLCD 2016. (Dewitz, 2019).

With a maximum saturated thickness of about 300 m in western Nebraska (Miller and Appel, 1997), the NSH overlies the majority of unconfined groundwater storage within the High Plains Aquifer. Historically there has been little evidence of reductions in groundwater storage beneath the NSH (Haacker et al., 2016a; V.L. McGuire, 2017; Peterson et al., 2016; Scanlon et al., 2012a), but the shallow water table in much of the NSH increases vulnerability to ERC encroachment and climate change (Adane et al., 2019b; Burbach and Joeckel, 2006; Loope and Swinehart, 2000; Suttie et al., 2005; Zou et al., 2018).

The Upper Middle Loup (UML) watershed is in the center of the NSH with an area of 4,950 km^2 (Figure 3-1). The study area expands over parts of Grant, Hooker, Thomas, Blaine, Sheridan, and Cherry counties.

The UML watershed (as part of the NSH) is highly baseflow-dominated (95% baseflow) (Szilagyi et al., 2011). Figure 3-2a illustrates the water depth in the NSH, estimated as the difference between the 30-m digital elevation model (DEM) (USGS, 1999) and spring 1995 water table data. As shown in Figure 3-2b, the water depths near the streams, where ERC usually persist, is 0-4 m which is within the range of ERC roots and would probably be impacted with ERC encroachments, especially where water depths are shallow. According to Anderson (2003), ERC roots can penetrate 7.5 m which increases the access to the water table to more than 17%. Figure 3-2c shows conceptually how ERC can have access to an unconfined aquifer and can limit seepage to the lake and streams. Though ET would be expected to be higher in areas where ERC roots can penentrate the water table, encroachment is not limited to those areas. Briggs et al., (2002) found that a tallgrass praire can be converted to closed-canopy ERC forest in as little as 40 years.
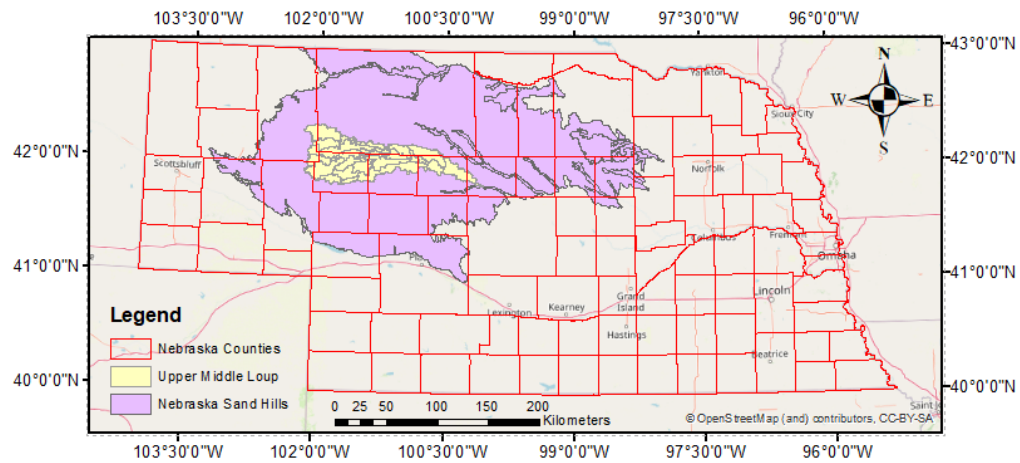
Figure 3-1: Location of the Upper Middle Loup watershed compared with Nebraska Sandhills and Nebraska state map.
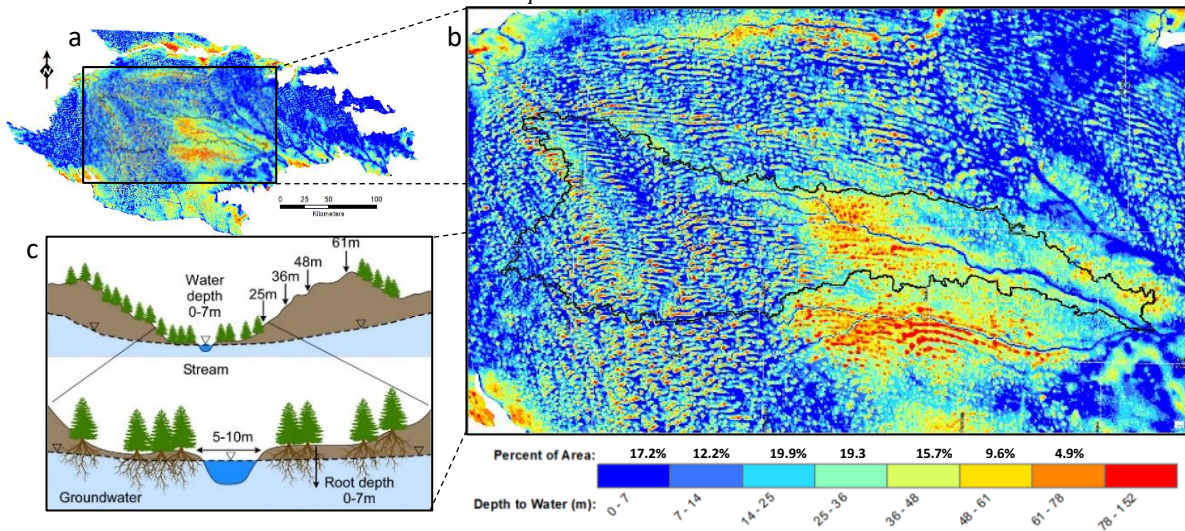
Figure 3-2: (a) The depth of water (m) in the Nebraska Sand Hills (source: Rossman et al., 2014) and (b) the Upper Middle Loup watershed, (c) schematic drawing of Eastern Redcedar root penetration into the vadose zone and water table.

3.2.2. Eastern Redcedar encroachment

Starks and Moriasi (2017) evaluated ERC encroachment impacts on stream discharges based on three scenarios (one to simulate the baseline encroachment, a second to simulate encroachment removal ERC-to-grassland, and a third scenario grassland-to-ERC by 10% increments up to 100%). However, the spatial distribution and expansion of ERC were not considered in conjunction with the 10% incremental changes. In this study, the impact of ERC on water resources in the UML watershed were evaluated using encroachment scenarios that incorporated different spatial distributions and expansion. Encroachment scenarios were created based on existing ERC cover and spatial variation of encroachment representative of the present and potential future environmental conditions. The baseline scenario (present condition, Figure 3-3a) had less than 1% encroachment in the watershed area. The additional encroachment scenarios, developed from baseline scenario using neighborhood approach, represent ERC cover at 11.9%, 16.1%, 28.0%, 40.6%, 57.5%, 72.5%, and 100 % of the landuse occupied by the rangeland (Pasture). In these scenarios, only rangeland was encroached while other land uses (e.g., lakes, wetlands, urban) remained constant. It was assumed that all these scenarios happens instantaneuously without development. However, it is worth mentionig here that the ecology of the red cedar can be affeted by different factors including the precipitation, levels of CO_2 in the atmosphere, accessbility to water, but quantifying these factors are out of the scope of this paper. The adopted scenarios, hypothitically, assumed the encraochment will occure to test its impacts on the water resources.

The baseline scenario was created by combining the evergreen and mixed forest land cover classes from National Land Cover Database (NLCD) 2016 where the landuse percentage are 93% of total watershed area) is herbaceous (Pasture), 4.2% as wetlands, 1% as lakes, 0.7% urban land, 0.44 red cedar, and 0.23 corn fields. The literature showed that evergreen eastern redcedar can encraoch into other forest types also the root system of evergreen can grow up to 7m deep into ground exceeding other species in the mixed lands according to US Forest Service Database (Anderson D., 2003), which means a higher level of impact on the water resource is expected from the red cedar in the mixed areas. Taking this into consideration the impact, combining the two land covers into ony evergreen not only serves the purpose of considering the higher impact but it help reduce the number of HRUs in the model itself. The baseline map was classified as a binary image, the presence of ERC is represented with a value of 1 while absence with 0. The binary image was passed through a moving window (3x3 m to 7x7 m) with a dilate morphological filter (Haralick et al., 1987b). When a binary image passes through the process of dilation, the area with value of 0 (non-redcedar/no encraochment) is replaced by 1 (ERC) represeting an encraochment occuring. The process was iterated to create ERC encroachment percentages of 11.9%, 16.1%, 28.0%, 40.6%, 57.5%, 72.5% and 100%.
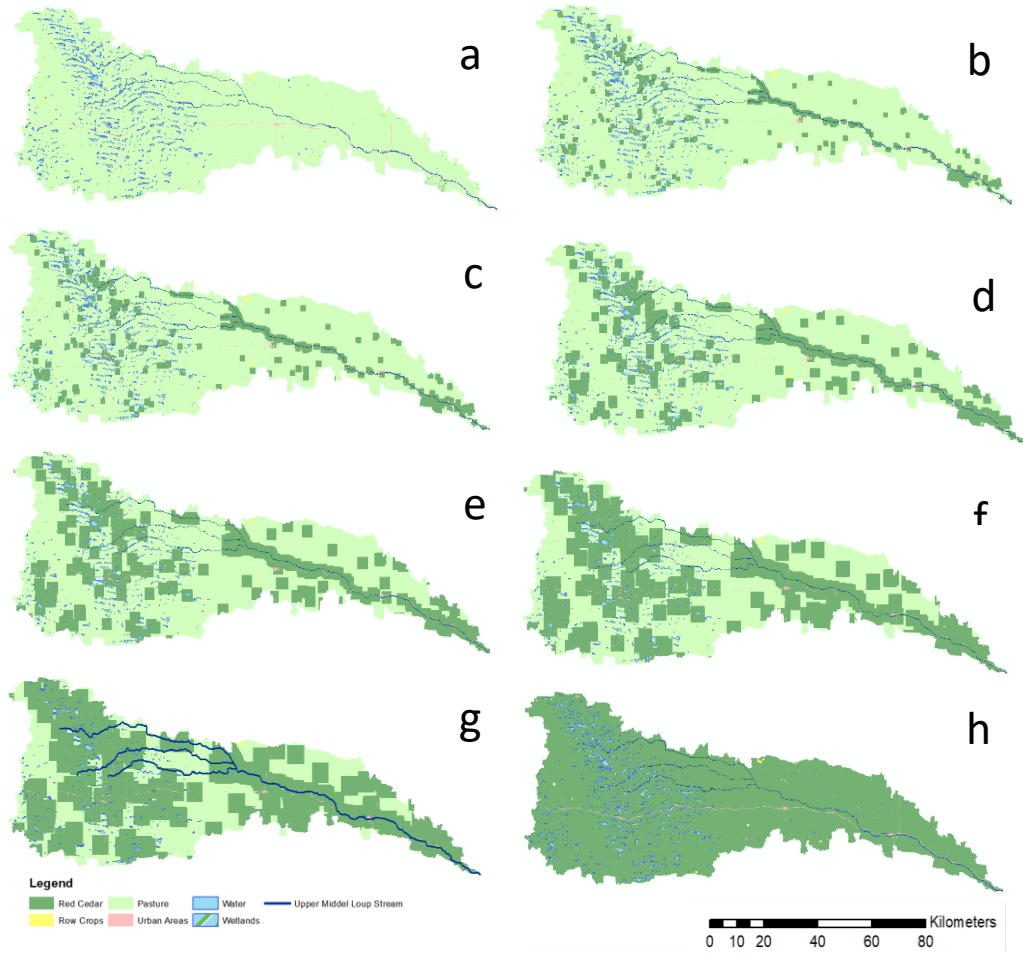
Figure 3-3: Eastern Redcedar (ERC), represented by dark green color, encroachment scenarios (a) baseline scenario <1%, (b) 11.9% (c) 16.1% (d) 28.0% (e) 40.6% (f) 57.5% and (g) 72.5% and (h) 100%

3.2.3. SWAT Model Setup

ArcSWAT version 2012.10._5.21 was used to set up the SWAT model using a 30 m DEM, NLCD land cover, and STATSGO soil layer. Table 3-1shows the different land cover, soil types, and slope and their percentage within the UML. Different combinations of land use, soil type, and slope produce unique hydrological response units (HRUs). Initially a total of 1439 HRUs and 37 subbasins were generated as shown in Figure 3-4. However, a segmentation of the Land use was performed to improve the representation of the encroachment scenarios as described in the next section of this paper.

Table 3-1: Percentage of each land use, soil type and slope for the Middle Loup Watershed used in the SWAT model.

LULC	Area %	Soil Type	Area %	Slope	Area %
Water	1.07%	NEW*	0.44%	0-2%	19.44%
Wetlands	4.27%	NE081	1.94%	2-4%	16.65%

Urban land	0.68%	NE133	40.61%	4-6%	14.86%
Forest	0.19%	NE134	17.08%	6-10%	24.74%
Pasture	93.56%	NE135	6.00%	>10%	24.31%
Corn	0.23%	NE137	33.16%	-	-
-	-	NE146	0.77%	-	-

* SWAT defined NEW soil type where soil data is missing. The model creates a new soil profile, and the user should populate the parameters. This is usually created where waterbodies cover the soil map, and no information is available about the bed soil.
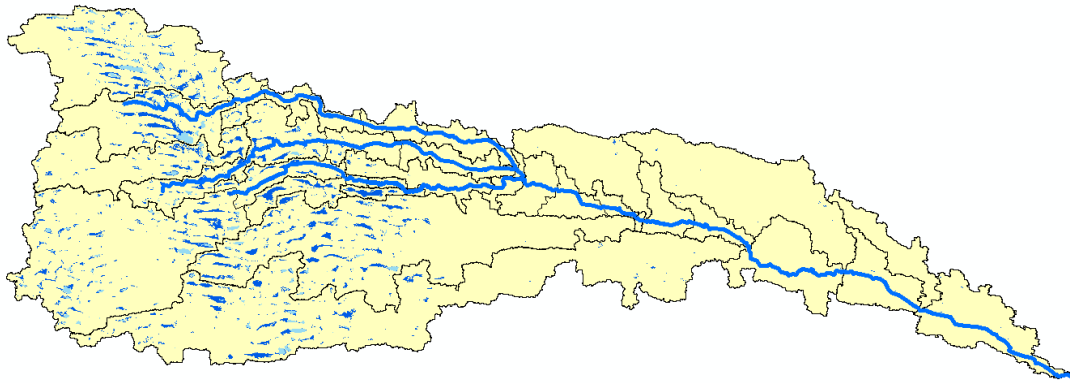
Figure 3-4: Upper Middle Loup watershed with SWAT model 37 subbasins and the ponds, wetlands and streams.

Daily rainfall and temperature data from 1981-2019 were obtained from the PRISM model (Parameter-elevation Relationships on Independent Slopes Model) (Manatsa et al., 2008) and downloaded through the PRISM Explorer (PRISM Climate Group, 2004). Although the water bodies within the model (wetlands and ponds) represent only 5% of the total area, they are concentrated within the upstream subbasins and are discharge regions (Rossman et al., 2019). Therefore, special focus was given to populate the wetland and pond parameters within the SWAT model, as shown in Table 3-2. The values of the parameters were mainly related to the area of each pond/wetland, which was calculated from the NLCD land use map. The estimation of the depth and volume of the ponds/wetlands parameters were based on the method mentioned by Evenson et al. (2018, 2016, 2015) and Muhammad et al. (2019). Additionally, the actual stream was defined based on aerial images (U.S. Geological Survey, 2020) to ensure better representation.

Table 3-2: Ponds and Wetlands SWAT Model Parameters

Pond Parameters	Parameters Definition	Value	Wetland Parameters	Parameter Definition	Value
PND_FR	Fraction of subbasin area that drains into ponds	Varies	WET_FR	Fraction of subbasin area that drains into wetlands	Varies

PND_PSA	Ponds Surface area when filled to principal spillway (ha)	Varies	WET_NSA	Wetlands Surface area when filled to normal water level (ha)	Varies
PND_PVOL	water Vol. stored when filled to principal spillway (m^3)	Varies	WET_NVOL	water Vol. stored when filled to normal water level (m^3)	Varies
PND_ESA	Ponds Surface area when filled to emergency spillway (ha)	Varies	WET_MXSA	Wetlands Surface area when filled to maximum water level (ha)	Varies
PND_EVOL	Water Vol. stored when filled to emergency spillway (m^3)	Varies	WET_MXVOL	Water Vol. stored when filled to maximum water level (m^3)	Varies
PND_VOL	Initial water Vol. in ponds (m^3)	Varies	WET_VOL	Initial water Vol. in wetlands (m^3)	Varies
PND_K	Hydraulic Conductivity of ponds bottom (mm/hr)	0.5	WET_K	Hydraulic Conductivity of wetlands bottom (mm/hr)	0.5
PNDEVCOEFF	Ponds Evaporation Coefficient	0.1	WETEVCOEFF	Wetlands Evaporation Coefficient	0.1

3.2.4. Modifying SWAT HRUs to perform proper Eastern Redcedar Encroachment Simulations

The discharge, ET, and recharge simulated by the calibrated SWAT model constituted the baseline scenario. Each ERC encroachment scenario was compared to the baseline. The encroachment percentages indicate the percentage of pasture that was converted to ERC in the calibrated SWAT model. Thus, the 100% encroachment scenario means that all HRUs that are classified as pasture are converted to ERC, and the relevant parameters in the SWAT model (i.e., CN, Max depth root, Canopy Maximum Interception Capacity CANMX) were changed to reflect the ERC parameters.

Due to the conceptual setup of the SWAT model, HRUs are a non-spatial feature. This means that any HRU with its unique features (i.e., slope, land use, soil type) can be located anywhere within the subbasin and the suer cannot select a specific HRUs in a specific unique location. Thus, it is impossible to reflect the generated encroachment maps from satellite images to the current model. This limits the opportunity to target a specific HRU without changing every HRU that holds the same features. Starks and Moriasi, (2017) performed a were split of HRU was performed where the sum of the area and the HRUs developed from the split equal the area of the original HRUs since in SWAT, HRUs are not spatially explicit. However, this does not allow to pick the location where the encroachment will possibly occur (i.e. near stream or around lakes and wetlands) instead it just select a percentage of HRU equivalent to the expected encroached area. To overcome the spatial limitation, a modification to the Land use map where pasture is located was performed. The original NLCD 2016 LULC map was divided into subsets within the original pasture land uses where each land use map represent a level of encroachment as shown in Figure 3-3. These maps were

combined into one land use map but the pasture land use was segmented into PA10, PA15, PA25, PA40, PA55 and PA70. The new names represent the same encroachment scenarios 11.9%, 16.1%, 28%, 40.6%, 57.5% and 72.5% respectively.

Only the class name was changed keeping other parameters of pasture as the original pasture class. This segmentation of pasture resulted in an increased number of associated HRU files from 1493 to 3342. The segmentation was conducted by overlaying the different land use maps representing the different encroachment scenarios. These maps were generated using satellite image analysis. After the model was calibrated the encroachment scenarios were simulated by selecting the related pasture class (thus selecting only corresponding HRU files where they should spatially be located). This is the first paper to use this approach.

3.2.5. SWAT model calibration approach

Strauch; and Linard;, (2009) performed streamflow simulations and percolation estimates using SWAT model for selected basins in the North-Central Nebraska for the period from 1940 to 2005. It simulated different subbasins including Elkhorn River Basin, Shell Creek Basin, Long Pine Creek Basin, Plum Creek Basin, and Loup River Basin.

The Loup River Basin is a watershed of around 38,850 km^2 with a dominant land uses of pasture/rangeland with agricultural land use along the river bottoms predominated by corn and soybeans. The mean annual precipitation in the Loup River Basin is 541 mm, the mean annual ET approximately 457 mm in and mean annual runoff is approximately 60.69 mm.

The study reported the statistical validation results for the performance of SWAT simulating streamflow for th Loup River of -1.13, 1.46 and, 21.11 for NSE, RSR, and PBIAS respectively. For a satisfactory results of NSE>0.5; RSR < 0.7; and PBIAS <+/-25, the study compared simulated and recorded streamflow values. To determine the ability of the watershed to estimate hydrological components the reported compared the cumulative basin-level water balance to the recorded and/or reported values. For the Loup River the following table show the comparison.

The water balance from the model was 185.4 mm compared to 48.24 mm from the recorded and reported values giving an difference of 26% of recorded over simulated balance.

The large water imbalance in the Loup River Basin model was caused by the large differences between the reported and simulated ET values. In this paper the improvement of ET and runoff simulations from SWAT model would improve the water balance estimation, thus the focus of calibration will be directed toward matching simulated ET with recorded ET on a monthly basis taking into account achieving acceptable percolation values. By keeping both ET and percolation within the range the uncertainty expected from SWAT model missing the stream discharge peaks could be alleviated. However, the modelling and

calibration approach will be applied towards the Upper Middle Loup (4,950 km^2 sub-watershed part of the entire 38,850 km^2 Loup River Basin Watershed) for the period between 2000-2019.

To calibrate the model the aquifer characteristics were evaluated, including the soil subsurface compositions, hydraulic conductivity, specific yield, lag time, and groundwater depths (Pettijohn and Chen, 1962; Rossman et al., 2014). To simulate the travel of water throughout the watershed, the lag time was applied to the SWAT model based on the values extracted from Rossman's groundwater model (Rossman et al., 2019). Additionally, Lag times ranged from 39 to 4500 days and the soil hydraulic conductivity and aquifer properties were applied based on USGS sub-soil map (Pettijohn and Chen, 1962).

Once the SWAT model was created, it was calibrated for evapotranspiration (ET), discharge, and recharge. Most modeling studies only calibrate discharge (Bailey et al., 2016; Dhami et al., 2018; Starks and Moriasi, 2017), and very few calibrate more than one hydrologic component (Jin and Jin, 2020). Thus, calibrating each component of the hydrologic cycle reduces the uncertainty in the results.

3.2.6. Discharge calibration approach:

The daily discharge data from the only USGS stream gauge located at the watershed outlet were downloaded for period of January 2000 to December 2019. With the high baseflow index, the variability in discharge was very low. The average streamflow was 13.4 m^{3}s^{-1} with a daily maximum and minimum of 19.7 and 10.3 m^{3}s^{-1}, respectively. 98% of the monthly discharge readings were between 11 and 17 m^{3}s^{-1}. The maximum discharge occurs in March, April, and May, ranging from 14-14.5 m^{3}s^{-1}, while the lowest flows occur from July to September ranging between 12.5-13 m^{3}s^{-1}. The calibration period is from the year 2000 to 2010 and the validation period is from 2011 to 2020.

3.2.7. ET calibration approach:

Billesbach and Arkebauer (2012) performed a long-term direct measurement of ET and surface water balance in NSH from 2003-2009. This study found that the three ecosystems in the NSH (sub-irrigated meadow, dry valley, and uplands) behaved in a different way. The annual ET for sub-irrigated meadow, dry valley, and uplands were 735 mm, 462 mm, and 280 mm, respectively. However, these measurements could only be considered point measurements compared the NSH scale. A study by Szilagyi et al. (2011) applied a Calibration-Free Evapotranspiration Mapping Technique (CREMAP) covering the entire state of Nebraska, which will be referred to as the CREMAP model. It provided a monthly ET estimation from January 2000 to December 2009. This was used to calibrate ET, not only for the entire watershed but also for each land use, specifically pasture and ERC. From the literature review, although some papers used ET as a calibration parameter, none of the papers calibrated ET for each land use. The average ET from the CREMAP model for the study area was around 482 mm. Average pasture and ERC ET was 479 mm and 511 mm, respectively.

In the NSH, there is very little runoff, so that it is often assumed that precipitation minus ET is equal to recharge. A study by Szilagyi et al. (2011) calculated the mean annual groundwater recharge across Nebraska using MODIS where the study utilizes 1-km 8-day composited MODIS surface temperature and basic atmospheric data. The monthly ET estimates resulted in an R^2 of 0.8 – 0.9, while the annual estimates had R^2 between 0.7-0.8. The mean annual ET estimated remained within 10% of the measured values. Another study by Rossman et al. (2014) evaluated how vadose zone lag time effects groundwater recharge in the NSH. They found that the recharge ranged from -204 mm (discharge in some areas where the lakes are clustered towards the western side of UML) to 143 mm (mainly towards the eastern and southern parts of the UML).

3.2.8. Recharge calibration approach:

Gilmore et al. (2019) used regional water table patterns to estimate the recharge rates in shallow aquifers. In the NSH, the mean annual recharge rates vary depending on soil type, land cover, climatic situation, and slope. The eastern part of the NSH has higher recharge rates (100-276 mm/yr) compared to the western parts, where recharge rates (0-60 mm/yr) are lower, or even discharge (0 to -386 mm/yr) can occur. For the UML watershed, the main discharge area is in the western part of the watershed, where lakes and wetlands are concentrated. The annual average recharge for the UML watershed is approximately 47 mm/yr compared to long-term mean recharge > 140 mm per year estimated in eastern Nebraska (Szilagyi et al., 2011).

3.2.9. Calibration evaluation approach and metrics:

A combination of manual and autocalibration using SWATCUP was used. Modeling results were evaluated using Nash-Sutcliffe Efficiency (NSE), R^2, and percent bias (PBIAS). NSE (Nash and Sutcliffe, 1970), which ranges from $-\infty \ to \ 1$, is often used to examine hydrological models' predictive power. The NSE equation is:

$$NSE = 1 - \left[\frac{\sum_{i=1}^{n}(Y_i^{obs} - Y_i^{sim})^2}{\sum_{i=1}^{n}(Y_i^{obs} - \overline{Y^{obs}})^2} \right]$$

where: Y_i^{obs} is the ith observation for the constituent being evaluated; Y_i^{sim} is the ith simulated for the constituent being evaluated; $\overline{Y^{obs}}$ is the mean of observed data for the constituent being evaluated, and n is the total number of observations.

Regression analysis is a statistical method that allows examining relationships between two or more variables. Many types of regression analyses focus on the influence of one (or more) independent variable on a dependent variable. The coefficient of determination is a key output of regression analysis (Thomas and Tiemann, 2015). This coefficient is one of the most widely used statistical coefficients, specifically

when the main purpose is to predict a future outcome or test hypotheses. Barten (1987) discussed R^2 and the following function presents a way to calculate this coefficient:

$$r^2 = \frac{ESS}{TSS} = \frac{sum\ of\ squares\ explained\ by\ regression}{total\ sum\ of\ squares}$$

$$TSS = ESS + USS = \sum (\hat{y} - \bar{y})^2 + \sum (y - \hat{y})^2$$

where: $\bar{y}$ is the average value of the dependent variable; y represents the observed values of the dependent variable, and $\hat{y}$ denotes the estimated value of y for the given x value.

$$PBIAS = \frac{\sum_{i=1}^{n}\left(Y_i^{obs} - Y_i^{sim}\right)}{\sum_{i=1}^{n}\left(Y_i^{obs}\right)} * 100$$

where Y_i^{obs} is the ith observation for the constituent being evaluated and Y_i^{sim} is the ith simulated value of the constituent being evaluated.

Percent Bias (PBIAS) measures the average tendency of the simulated values whether they are larger or smaller than their observed counterparts. A PBIAS of 0.0 is optimal, where low-magnitude values indicate more accurate model simulations (Yapo et al., 1996). In hydrological models, PBIAS can help to examine the model tendency towards underestimation (positive values) or tendency towards overestimation (negative values) (Van Liew et al., 2005).

3.2.10. Encroachment simulation approach

according to the literature review (Afinowicz et al., 2005; Ahl et al., 2008; Giulia Lembo Caterina, 2012) specific parameters changing can represent conversion of pasture to ERC. To perform the conversion of pasture to ERC (e.g. to simulate encroachment) the parameters shown in Table 3-3 were changed in each one of the corresponding pasture classes' HRUs (i.e. PA10, PA15, PA25, PA40, PA55, and PA70).

Table 3-3: Pasture and Eastern Redcedar parameters to simulate encroachment.

Parameters	Parameters Definition	PAST* Value	FRST** Value
CANMX	Maximum Canopy Storage (mm H_2O)	10	28
Sol_K	Saturated hydraulic conductivity (mm/hr)	70	116
Sol_ZMX	Maximum rooting depth of soil profile (mm)	525	8024
CN2	Initial SCS runoff curve number for moisture condition II	50	37
BLAI	Maximum potential leaf area index	4	5
CHTMX	Maximum canopy height (m)	0.5	10
RDMX	Maximum root depth (m)	2	3.5

* PAST: Pasture, **FRST: Eastern Redcedar

3.2.11. Single and Dual Risk Analysis for water quality evaluation

We assumed that discharge in the Loup River near Genoa (USGS gauge 06793000) would mimic that of the UML due to ERC encroachment. The reduction in flow was then subtracted from the discharge near North Bend (USGS gauge 06796000) on the Platte River. Measured concentrations of nitrate and atrazine were available at gauge stations 06793000 and 06796000 for the years 2010 to 2014 on an annual basis. Based on the baseline and encroachment scenarios, the concentration for nitrate and atrazine was estimated at gauge station 06796000 to assess the impact of encroachment on water quality in the Platte River. A relation between the flow vs concentration downstream at North Bend gauge was established.

For example, for the nitrate 1.44 mg L^{-1} in table 6, this number came from calculating total nitrate concentration at North Bend over the total water flowing through North Bend for each year and 1.44 is the average of all years. The total nitrate concentration was estimated based on the measured nitrate value multiplied by the recorded discharge quantity at North Bend. For the baseline (no encroachment) the same gauge reading was taken. To reflect encroachment scenarios impacts on the discharge reduction at North Bend, North Bend discharge represent the cumulative discharge coming from Duncan and Genoa as shown in Figure 3-8. While Duncan is not subjected to flow reduction (assuming the encroachment occurred only in the UML) only Genoa would transfer the percentage of reduction from Dunning. Genoa discharge is reduced in the same percentage as Dunning but using the Genoa discharge measurement.

The ranges of reported discharges at these gauges were collected for the same period used for SWAT simulation (2000-2020). The discharge at Dunning, Genoa, Duncan and North Bend were 13.9, 29.9, 50.5, and 130 m^{3}s^{-1} respectively. While for the water quality parameters, the ranges reported nitrate and atrazine for the years from 2010-2014 the nitrate concentrations ranged from 1.04 to 1.64 mg L^{-1} while the atrazine concentrations ranges from 0.35 to 3.36 µg L^{-1}.

Additionally, a risk factor was calculated for nitrate and atrazine exposure for the Platte River for each encroachment scenario based on the method adopted by Hansen et al. (2019). This study identified the risk of nitrate and atrazine exposure individually (single risk factor, SRF) and together (dual risk factor, DRF) for nitrate and atrazine in several locations within Nebraska. The SRF was determined based on sets of measured data and maximum contamination level (MCL) at 10 mg L^{-1} for nitrate and 3 µg L^{-1} for atrazine. The SRF analysis is:

$$RF_{MCL}^{95th\%} = \frac{95perc(MEC_i)}{MCL}$$

were $RF_{MCL}^{95th\%}$ is the risk factor for the contaminant based on the 95th percentile of the MEC and MCL, MEC_i is the measured environmental concentration at time i (based on yearly step according to the collected data), MCL is the maximum contaminant level according to Environmental Protection Agency acceptable concentrations for drinking water. were $RF_{MCL}^{95th\%} < 0.8$ safe, 0.8 to 1.0 Low Risk; 1.0 to 2.0 At Risk and > 2.0 is considered High Risk. A study by (Rhoades et al., 2013) showed that exposure to nitrate and atrazine together increased the occurrences of Non-Hodgkin Lymphoma in Nebraska. Hansen et al (2019) calculated the DRF by:

$$DRF = RI(x_1) + RI(x_2)$$

where RI(x) is the risk integer of contaminant (x) and DRF is the dual risk factor. A general term was applied to these different integer values for dual risk factor: 0 = Very Low Risk; 1 = Low Risk; 2 = Medium-Low Risk; 3 = Medium Risk; 4 = Medium-High Risk; 5 = High Risk; and 6 = Very High Risk.

3.3. Results and Discussion

3.3.1. SWAT Model Calibration and Validation

The calibrated model was compared to monthly observed discharge, ET, and recharge. Table 3-4 lists the parameters used in the SWAT calibration, their default ranged and calibrated values. It was found that discharge was most sensitive to the groundwater parameters (i.e., GW_Delay) and HRU-related parameters (i.e., LAT_TTIME and CANMX). For ET, GW_REVAP and soil-related parameters (i.e., Sol_AWC, Sol_K) were the most influential. Autocalibration was initially conducted before applying different manual calibration simulations using the mentioned parameters. The optimized values of the SWAT parameters are valid for all HRUs in the model domain.

Table 3-4: SWAT model calibration parameters, default ranges and the calibrated values.

GW_REVAP.gw	0.02 – 10	8	Groundwater "revap" coefficient.
GW_DELAY.gw	0 – 500 days	31	Groundwater delay time (days).
ESCO.hru	0 – 1	0	Soil evaporation compensation factor.
EPCO.hru	0 – 1	0.1	Plant uptake compensation factor.
CN.mgt	Varies	Varies	Initial SCS runoff curve number for moisture condition II
LAT_TTIME.hru	40 – 4500	Varies	Lateral flow travel time (days)
CANMX.hru	0 – 28	0, 10, 28	Maximum canopy storage (mm H_2O)
Sol_AWC.sol	0 – 1	0.22	Available water capacity of the soil layer (mm H_2O/mm soil)
Sol_K.sol	2 – 450	Varies	Saturated hydraulic conductivity (mm/hr)
PND_FR.pnd	0 – 1	0.1	Fraction of subbasin area that drains into ponds.
WET_FR.pnd	0 – 1	0.1	Fraction of subbasin area that drain into wetlands.
PLAPS.sub	-500 – 500	3.2	Precipitation lapse rate (mm H_2O/km).
TLAPS.sub	-50 – 50	0	Temperature lapse rate (°C/km).

3.3.2. Results of Discharge simulation:

The simulated discharge was close to the measured discharge pattern over the calibration (2000-2009) and validation periods (2010-2020) (Figure 3-5). Considering the low variability in discharge, where all the values lie between 10 to 20 m^3s^{-1}, we did not anticipate acceptable values for the metrics. The Q95/Q5 is only 1.41 with a Q95 of 16.3 m^3s^{-1} and Q5 of 11.5 m^3s^{-1} (Hobza and Schepers, 2018).

For the calibration period, the R^2, NSE, and PBIAS were 0.01, -8.38, and 19%, respectively. For the validation period the R^2, NSE, and PBIAS were 0.03, -8.99, and 21%, respectively.

Though the R^2 and NSE an unsatisfactory rating, the PBIAS was satisfactory. The simulated discharge for both calibration and validation periods were close to the observed averages. For the calibration period, the average simulated discharge was 12.1 m^3s^{-1} compared to the observed 13.2 m^3s^{-1}. For the validation period, the simulated discharge was 16.3 m^3s^{-1} compared to 14.4 m^3s^{-1} of the observed discharge.

Additionally, the model check achieved 0.95 baseflow percentages which approaches the recorded baseflow near the UML outlet based on USGS Science Data Catalog (SDC). Hobza and Schepers (2018) stated that the streamflow out of the NSH, groundwater discharges (defined as baseflow) ranges from 0.8 to 0.95. We hypothesize that the underprediction during the high flows may be due to the hundreds of oxbow lakes in the watershed. These oxbows would reduce the peak flow and increase the length of the falling limb of the hydrograph. As illustrated in Figure 3-5, the model responded to the large precipitation events, but the stream did not. In the only other study where SWAT was used in the NSH, modeling statistics were also poor, with NSE of -1.13, and PBIAS of 21.1 (Strauch and Linard, 2009).
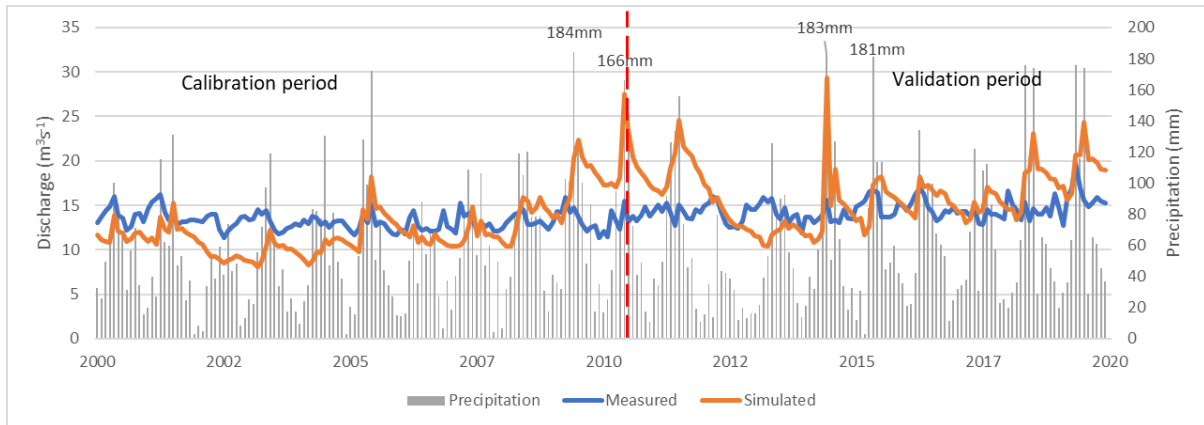
Figure 3-5. SWAT simulated vs observed discharge for the Upper Middle Loup watershed for the calibration (2000-2009) and validation periods (2010-2020)

3.3.3. Results of ET simulation:

The simulated ET for the entire watershed (2000-2009) was 483 mm compared to the CREMAP model average of 482 mm (~99%). The NSE and PBIAS metrics were 0.63 (Satisfactory) and -0.51 (Very Good), respectively. Additionally, ET model results for pasture and ERC were similar to the observed values with NSE, R^2, and PBIAS of 0.64, 0.65, and 0.82% for pasture and 0.45, 0.46, and 0.01% for ERC, respectively.

3.3.4. Results of recharge simulation:

Rossman et al. (2014) estimated an average recharge across the UML watershed of 56 mm/yr from 2000-2009. The calibrated SWAT model simulated an average of 54.2 mm/yr. This shows that the SWAT simulation of recharge achieved a very close estimation to Rossman et al (2014) (~97%). With our model simulations yielding discharge, ET, and recharge values comparable to measured values, our encroachment scenario results will thus have less uncertainty.

3.3.5. Evaluation of water balance:

Looking at the model outputs in terms of water balance in the baseline scenario, the model predicted precipitation 659.3, runoff 3.7, percolation 75.55, evapotranspiration 483.2, deep recharge 3.78, lateral flow 67.62, REVAP 72.11 (all in mm). To evaluate the water balance different zones were considered to conceptualize and explain how water entering and leaving the system is partitioned and/or routed. This

paper scored a simulated water balance of 122mm compared to 121mm of reported water balance (99.1%) giving a significance improvement compared to 26% scored by Strauch; and Linard;, (2009).

3.3.6. Encroachment Scenarios

Different encroachment scenarios were simulated using the calibrated SWAT model. The scenarios were conducted by changing the pasture classes in the modified land use (PA10, PA15, PA25, PA40, PA55, and PA70) into ERC. The general trend indicates that as the encroachment percentage increases, the average discharge decreases (Figure 3-6). An increase of ERC to 11.9% yielded a reduction in discharge from 12.1 to 11.5 m3 s-1. Additionally, the fact that the watershed is baseflow-dominated (i.e., more than 90% of the lateral flow is baseflow) makes the impacts of interception from ERC roots significant. Thus, any increase of ERC reduces lateral flow (feeding the streams). As encroachment continues to 41% and 100%, discharge to the UML decreases by 24.4% and 46.5%, respectively.
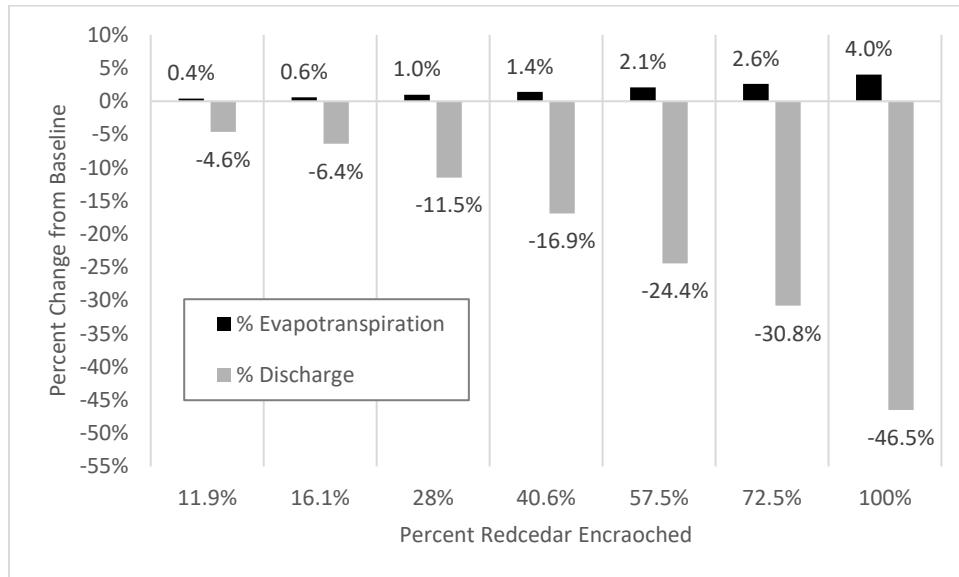
Figure 3-6: Simulated discharge and evapotranspiration for various levels of Easter Redcedar encroachment in the Upper Middle Loup watershed.

As shown in Table *3-5*, different hydrological components were evaluated for each of the simulated encroachment scenarios. The ET increases as the encroachment percentage increases. 11.9% encroachment resulted in a 0.43% increase in ET compared to the baseline, while a 100% encroachment resulted in a 4% increase. On the contrary, the discharge decreased as the encroachment increased with a -4.59% reduction for the first 11.9% of encroachment and reducing to -46.5% with 100% encroachment. Zou et al., (2018) stated that a complete conversion of rangeland to ERC (i.e., 100%) encroachment would lead to streamflow (i.e., discharge) reductions of 20-40%. Similarly, while the ET increased (with the increase of encroachment), the percolation increased from 75 mm to 95 mm at full encroachment (Figure 3-7). Though several studies have shown that recharge decreases from ERC encroachment, others have shown increases. For example, Tobella et al., (2014) showed increased infiltration rates and recharge potential with

afforestation in simi-arid agroecosystems. Zhang et al. (2020) argue that under normal condition of land-use change (i.e., transition from plant cover to another one), recharge usually decreases. However Shao et al. (2019) states that with the with smaller values of Sol_K, the lateral flow of SWAT decreased, thus allowing more water to recharge groundwater (increase in percolation and deep recharge). This can be seen from the results in our study, where the ranges of Sol_K are from 2.91 to 450 mm hr^{-1} with the majority of HRUs (2202 out of total 3342 HRUs) has a range of Sol_K 116 to 180 mm hr^{-1}, where a decrease in lateral flow was accompanied by an increase in both percolation and deep recharge.

Table 3-5: Water balance components from each encroachment scenario compared to the baseline scenario. All parameter units are in mm except for CN (unitless) and discharge (m3 s-1). CN=Curve Number

	Baseline	11.9%	16.1%	28%	40.6%	57.5%	72.5%	100%
Precipitation	659.3	659.3	659.3	659.3	659.3	659.3	659.3	659.3
Runoff	3.7	3.36	3.27	3.05	2.88	2.69	2.53	2.03
Percolation	75.55	77.37	78.18	80.53	83.05	86.54	89.53	95.72
Evapotranspiration	483.2	485.3	486	488	490	493.1	495.6	502.7
% ET from baseline	-	0.43%	0.58%	0.99%	1.41%	2.05%	2.57%	4.04%
Deep Recharge	3.78	3.87	3.91	4.03	4.15	4.33	4.48	4.79
Lateral Flow	67.62	64.67	63.49	60.07	56.36	51.34	46.95	36.43
REVAP*	72.11	73.84	74.6	76.84	79.23	82.53	85.37	91.19
Potential Evapotranspiration	939.3	939.5	939.5	939.7	939.8	940.1	940.3	940.9
Average Curve Number	50.12	48.97	48.53	47.3	45.98	44.17	42.56	38.09
Discharge	12.06	11.51	11.29	10.67	10.01	9.12	8.34	6.45
% disch from baseline	-	-4.59%	-6.37%	-11.5%	-16.9%	-24.4%	-30.8%	-46.5%

* REVAP: amount of water moving from shallow aquifer to plant/soil profile
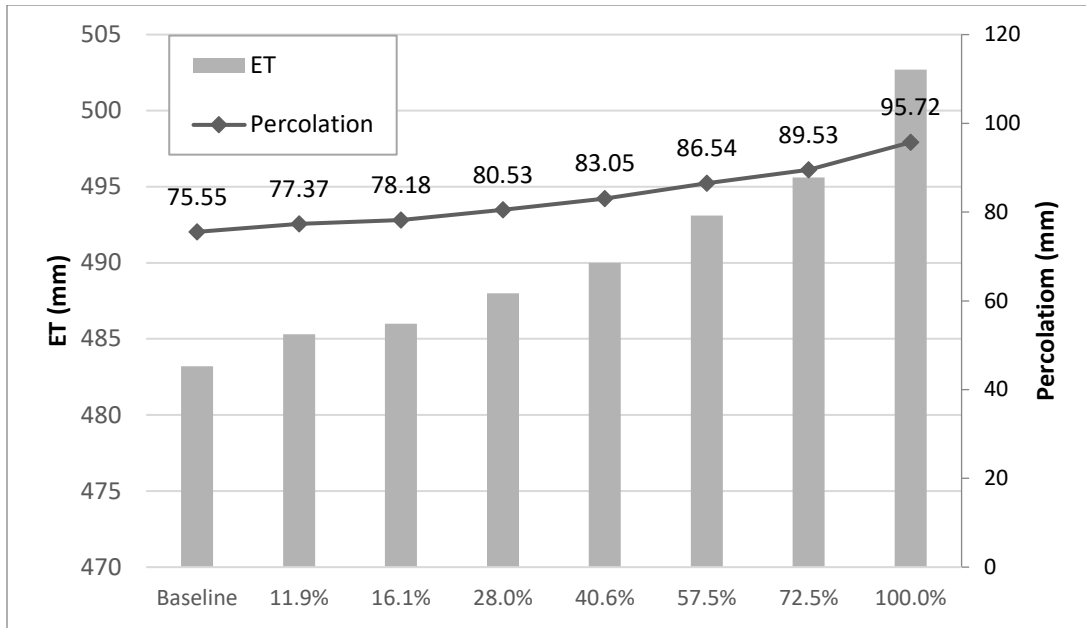
Figure 3-7: Comparison of simulated ET (evapotranspiration) vs percolation for each redcedar encroachment scenario.

3.3.7. Impact of Eastern Redcedar Encroachment on the Platte River

Though less than 1% of the Loup River watershed is currently ERC, the rate of encroachment has increased recently (Lower Loup NRD, 2017). The land use in the Loup River watershed is similar to the UML watershed, though there is less pasture in the Loup River watershed (80% vs 94%) and more cropland (15% vs <1%). As shown in Figure 3-8, the Loup River watershed discharges at Genoa (USGS gauge 06793000) to the Platte River, and the encroachment changes in the UML and Loup River watershed impact the discharge at North Bend (USGS gauge 06796000) on the Platte River.
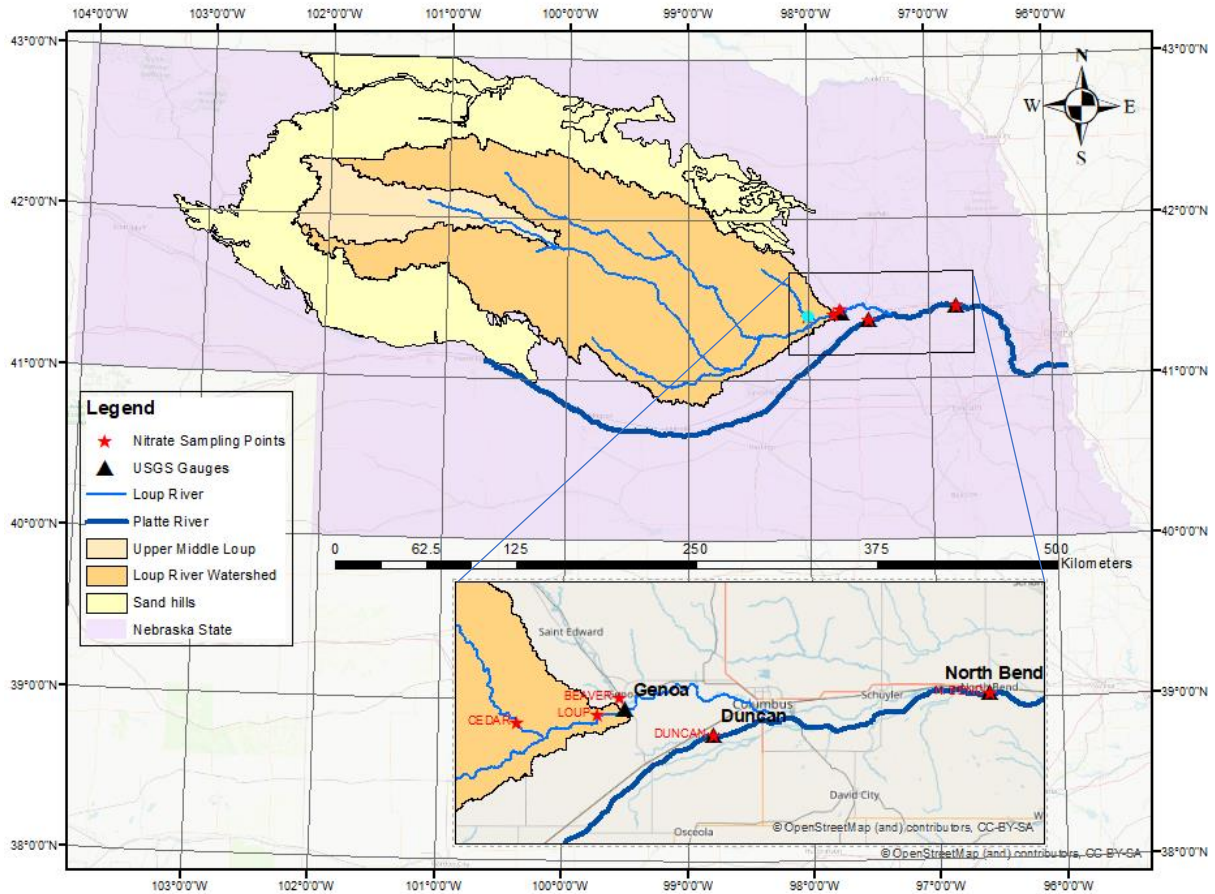
Figure 3-8: Map illustrating the Upper Middle Loup Watershed relative to the Loup River Watershed and Sand Hills

Assuming the impact on discharge of ERC encroachment would be similar in the Loup River watershed as the UML watershed, though there is less pasture and more cropland, we evaluated the potential impact of ERC encroachment on the entire Loup River watershed and its impact on the Platte River discharge and water quality based on the results obtained from the UML watershed encroachment scenarios.

To examine this, we evaluated discharge from three USGS gauges on the Loup and Platte Rivers (Figure 3-9). These locations are the Loup River near Genoa (USGS gauge 06793000), Platte River near Duncan (USGS gauge 06774000), and Platter River at North Bend (USGS gauge 06796000). The gauge station 06774000 is upstream of the confluence with the Loup River, while the gauge station 06796000 is downstream of the tributary. The analysis of the discharge from these three gauges shows similar peaks and baseflow.
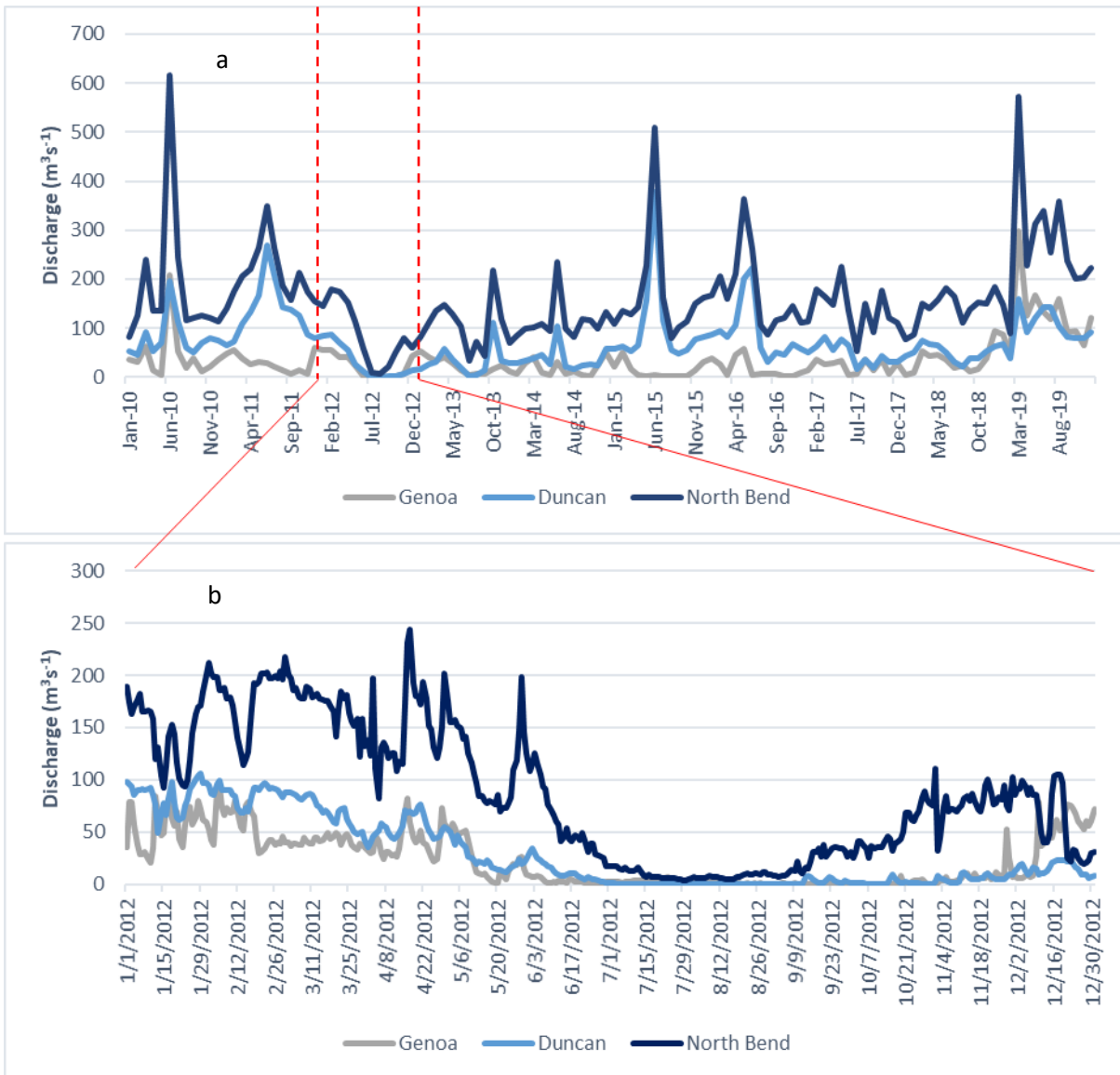
Figure 3-9: (a) Comparing Flow at Genoa gauge (at Loup River) with Duncan and North Bend Gauges (at Platte River) from 2010 to 2019; (b) average daily discharge for the three sites for the drought year 2012

The average discharge in the Loup River from 2000-2019 was 13.8 and 28.9 m^3s^{-1} at Dunning and Genoa, respectively. The stream discharge on the Platte River was 51.8 and 128.8 m^3s^{-1} at Duncan (upstream of confluence) and North Bend (downstream of confluence), respectively for the same period. Therefore, 23% of the discharge at the North Bend gauge originates from the Loup River (9a). In the drought year 2012 (9b) the average monthly flows were 23.8, 29.8, and 87.4 m^3s^{-1} at Genoa, Duncan, and North Bend, respectively (that is 80%, 57%, and 67% of the average flow from 2000-2019 for the three stations). Any impact on the discharge from the ERC encroachment will not only influence the discharge in the Loup River, but also the discharge in the Platte River.

Assuming encroachment to the Loup River would be equally impacted by ERC encroachments, the discharge at Genoa would decrease from 28.9 to 25.6 m^3s^{-1}, 21.9 m^3s^{-1}, and 15.5 m^3s^{-1} for 28%, 57.5%, and 100% encroachment, respectively. At the North Bend gauge on the Platte River, the average discharge would decrease from 126.9 m^3s^{-1} to 123.6 m^3s^{-1}, 119.9 m^3s^{-1}, and 113.5 m^3s^{-1} for 28%, 57.5%, and 100% encroachment of the Loup River watershed, respectively.

This reduction in discharge to the Platte River will also impact water quality, a concept noted by Zou et al. (2015). The assessment of discharge at USGS gauges, at Genoa, Duncan, and North Bend, is important to estimate the potential changes in water quality at both Loup and Platte Rivers. The available water quality measures of both nitrate and atrazine (from 2010 to 2014) were averaged at both Genoa and North Bend. The nitrate concentrations were 0.67 mg/L and 1.44 mg/L, while the atrazine concentrations were 0.51 µg/L and 1.22 µg/L at Genoa and North Bend stations, respectively.

Accounting for the reduced discharge to the Platte River, concentrations of nitrate increased from 1.44 to 1.61 m L^{-1}, and atrazine increased from 1.22 to 1.37 µg L^{-1} for the 100% encroachment (Table 3-6). The findings show that an increase by 11.0% and 12.3% for nitrate and atrazine, respectively, in the Platte River. The SRF for both nitrate and atrazine is Low Risk (1) on a scale from 0 (Considered Safe) to 3 (High Risk). At 28% encroachment, the SRF for atrazine increases to 2 (At Risk) and the DRF increases from Medium Low Risk to Medium Risk, based on our modeling assumptions. These predictions support the hypotheses that an increase in ERC encroachment in the Loup River watershed will impact both water quantity and quality in the Platte River. While our modeled results have substantial uncertainties, they highlight the general concept that the amount of water discharging from NSH streams is relevant to cities of Lincoln and Omaha in terms of water security and water resources management plans.

Table 3-6: Estimates of water quality parameters and Single Risk Factor at North Bend Gauges on the Platte River for years 2010-2014

ERC Scen.	Nitrate Concentrations mg L^{-1}						SRF	Risk Class
	Avg.	2010	2011	2012	2013	2014		
baseline	1.44	1.64	1.04	1.61	1.34	1.58	0.817	low risk
11.9%	1.46	1.66	1.05	1.63	1.35	1.59	0.826	low risk
16.1%	1.46	1.67	1.06	1.63	1.36	1.60	0.830	low risk
28%	1.48	1.69	1.07	1.65	1.37	1.62	0.840	low risk
40%	1.50	1.71	1.08	1.68	1.39	1.64	0.851	low risk
57%	1.53	1.74	1.10	1.71	1.42	1.67	0.866	low risk
72%	1.55	1.77	1.12	1.73	1.44	1.70	0.880	low risk
100%	1.61	1.84	1.16	1.80	1.50	1.77	0.915	low risk
ERC Scen.	Atrazine Concentrations µg/Liter						SRF	Risk Class
	Avg.	2010	2011	2012	2013	2014		
baseline	1.22	0.56	0.52	1.33	3.36	0.35	0.98	low risk

11.9%	1.23	0.56	0.52	1.34	3.39	0.35	0.99	low risk
16.1%	1.24	0.56	0.52	1.34	3.41	0.35	1.00	low risk
28%	1.25	0.57	0.53	1.36	3.45	0.36	1.01	risk
40%	1.27	0.58	0.54	1.38	3.49	0.36	1.02	risk
57%	1.29	0.59	0.55	1.40	3.55	0.37	1.04	risk
72%	1.31	0.60	0.56	1.43	3.61	0.37	1.06	risk
100%	1.37	0.62	0.58	1.48	3.76	0.39	1.10	risk

Future work includes the coupling of SWAT with MODFLOW. The SWAT model is limited in its ability to simulate groundwater processes. Using SWAT-MODFLOW in this baseflow-dominated system will improve modeling results. This coupling of the surface and the groundwater model can help improve the calibration of the model, thus improve the estimation of discharge. Coupling with MODFLOW will also provide the change in the water table as ERC encroachment increases. The reduction in the water table will impact the thousands of lakes and wetlands, as well as the ecosystem, in the NSH.

Another aspect of future improvement would be more accurate ERC encroachment predictions by applying machine learning or some ecological model to better predict the spatial and temporal spread of ERC. Incorporating climate change models will not only impact the water resources directly but will influence the growth rate of ERC based on changes in temperature, precipitation, and CO_2.

3.4. Conclusions

In this study, the SWAT model was utilized to examine the impacts of Eastern Redcedar encroachment on the water resources in the Nebraska Sandhills, a major recharge zone for the High Plains Aquifer, and the Platte River, a major water source for the cities of Omaha and Lincoln. The scenarios ranged from 11.9% to 100% encroachment. The results showed a reduction in discharge as the encroachment increased. With full encroachment, the flow in the Upper Middle Loup River was reduced by nearly half (53% of the original flow), and the evapotranspiration increased 4.04% from baseline. Assuming the same reduction in discharge for the Loup River watershed, a major tributary to the Platte River, the discharge in the Platte River will decrease from 126.9 m^3s^{-1} to 123.6 m^3s^{-1} and 113.5 m^3s^{-1} for 28% and 100% encroachment, respectively. Additionally, we evaluated the impacts of the Eastern Redcedar encroachment on water quality in the Loup and Platte Rivers. When assuming constant nitrate and atrazine loading, but decreased stream flow, model results follow the intuitive pattern of increased concentrations of nitrate and atrazine in the Platte River. With 100% ERC encroachment, concentrations could increase by 11.0% and 12.3% for nitrate and atrazine, respectively, in the Platte River. The risk level for atrazine could increase from Low Risk to At Risk at just 28% encroachment, and the dual risk of nitrate and atrazine increases from Medium Low Risk to Medium Risk.

Chapter 4.   The combined impact of redcedar encroachment and climate change on water resources in the Nebraska Sand Hills

4.1. Introduction

Historically, water has been considered the backbone of human civilization and the main factor in its development. Increasing water demand related to the intensification of agriculture, industry, and domestic water uses and decreasing freshwater supplies have made it critical to continuously explore additional water sources and ways to achieve universal water access. Globally, the agricultural sector uses between 60% to 90% of water (Adeyemi et al., 2017; Pedro-Monzonís et al., 2015) and according to the Food and Agriculture Organization, FAO, (2017) and Doungmanee (2016), this accounts for nearly 72.5% of freshwater withdrawals. Agriculture is considered the major user of groundwater and surface water in the United States (U.S.) with 80% consumption of water resources (up to 90% in the Western U.S. (Hrozencik, 2021). Because 60% of irrigation in the U.S. relies on groundwater, aquifer overexploitation can significantly impact crop production. More importantly, groundwater depletion in the irrigated High Plains accounts for ~50% of groundwater depletion (Scanlon et al., 2012b).

The High Plains Aquifer represents an invaluable source of groundwater for the U.S. The aquifer is in the central part of the U.S. expanding from South Dakota in the north to Texas in the south. It underlies parts of eight states (Overmann, 2021) with a total area of approximately 453,248 km^2 and total recoverable water in the storage of about 3.6 trillion m^3 (Virginia L McGuire, 2017). The dust bowl of the 1930s and the development of modern pump hydraulics, improvements in irrigation technology, and availability of low-cost energy increased the number of wells drilled into the aquifer from 21,000 wells to 30,000 in 1980 (Gutentag et al., 1984) then increased to 200,000 wells in recent years (Hennings and Lynch, 2022). This reliable source of water helped transform this part of the U.S. into the "Breadbasket of the World" (Steward and Allen, 2016). However,   groundwater withdrawals have greatly exceeded R rates by approximately 3 to 1 (American Ground Water Trust, 2002), decreasing the water storage by 410 km^3 from 1935 to 2011 (Haacker et al., 2016b). The largest reduction in water storage has been recorded in the Central and Southern Plains where the storage has declined by more than 11.9% per decade. The water level decline has been minimal in the Northern High Plains, the location of the Nebraska Sand Hills (NSH) (Haacker et al., 2016b). The NSH is considered a major recharge zone for the High Plains Aquifer. According to Rossman et al., (2014), the sand dunes in the NSH are composed of eolian sand (well-sorted) and fine-to-medium grained soil. This region has high sand content ranging from 94 to 97% which yields high infiltration rates and minimal overland flow. Eggemeyer et al., (2009) stated that 36% of the High Plains Aquifer area and 65% of its water are located under Nebraska (specifically NSH) where 6-14% of the annual precipitation (P) recharges the aquifer. Szilagyi et al. (2011) estimated that the largest mean annual recharge rates (200±85

mm yr^{-1}) occur in the southern and eastern parts of the NSH while smaller rates (40±59 mm yr^{-1}) occur in the western part. This supports the importance of the NSH as a recharge zone for the High Plains Aquifer. In the NSH, the largest land use threat is the eastern redcedar (*Juniperus Virginiana*) (Heavican, 2021). Redcedar, a native Nebraska flora, was historically controlled by wildfires (Axmann and Knapp, 1993). The reduction in wildfires and the planting of redcedar for windbreaks have increased the number of trees in the NSH. Shrestha (2022) found that the area of redcedar in this part of Nebraska increased from 686.30±409.58 km^2 in 1990 to 1521±316.09 km^2 in 2020 based on stratified random estimates. The encroachment rate thus varied between 2.26 and 11.19% annually. Applying the Markov-chain and cellular automata model to the encroachment trend estimated redcedar cover would increase from 5,016 km^2 to 14,256 km^2 by 2099.

Kishawi et al., (2023) used different scenarios that considered redcedar encroachment spatially throughout the watershed with different encroachment levels ranging from 11.9% to 100% of grassland converted to redcedar. The study found, for example, that 16.1% redcedar encroachment in the NSH can reduce D by 12% and increase evapotranspiration and percolation by 0.6% and 3.4%, respectively. With 100% encroachment, the D would be reduced by nearly 50% while the recharge increased by 26% thus potentially increasing the concentration of atrazine in the Platte River by 16.3% to 48.1%. Starks and Moriasi (2017) considered 10% increments of redcedar encroachments in the North Canadian River watershed in central Oklahoma. They found that if rangeland was replaced by redcedar completely (100% encroachment), a reduction in D could reach 112% of the current municipal water demand and 89% of the projected 2060 demand. Zou et al., (2018) found that a complete conversion of rangeland to redcedar would reduce D by 20% to 40%. None of these studies considered the additional impact of climate change on the hydrology of the watershed.

Both land use and climate change can cause significant changes in water resources. Hydrological models can help understand how these variables interact and impact the water cycle. Several studies have evaluated the impact of climate change on the hydrological cycle at the watershed scale. Some studies applied different representative concentration pathways (RCPs) scenarios for different climate models under Coupled Model Intercomparison Project 5 (CMIP5) using RCP2.6, RCP4.5, and RCP8.5 (Ercan et al., 2020; Fant et al., 2017; Wang et al., 2020), or consider the impacts of changing CO_2 on hydrological fluxes while applying climate models (Lee et al., 2018; Perazzoli et al., 2013). Many studies used the Soil Water Assessment Tool (SWAT) with climate models on different scales worldwide (Pandey et al., 2021; Touseef et al., 2021), in the U.S. (Ercan et al., 2020; Mueller-Warrant et al., 2019) and in Nebraska (Rehana et al., 2018; van Liew et al., 2012).

Few studies have also evaluated the combined impact of both land use and climate change (Petrovic, 2021; Teklay et al., 2021; Zhang et al., 2016). Petrovic, (2021) studied the impacts of both climate and land use

change on hydrology and found that the overall decline of annual flow is due to the decline in seasonal flow under combined scenarios. Teklay et al. (2021) studied four land-use scenarios under climate projections from 2005-2015 and 2045-2055 using RCP4.5 and RCP8.5. The results showed that surface runoff increased by 5.1% while baseflow decreased by 6.5%. Under expansion of irrigation crops and forest, D decreased by 12.5% and 5.2%, while evapotranspiration increased by 4.8% and 8.9%, respectively. Under RCP8.5, D, surface runoff, and evapotranspiration increased by 34.3%, 51.8%, and 12.2% showing that climate change was more important than land-use change. Zhang et al. (2016) agreed with this conclusion by assessing separate and combined hydrological impacts of land use and climate change between 1995-2014 and 2015-2024. Zhang et al. (2016) applied two land-use models in SWAT and applied hypothetical climate scenarios based on analyzing climatic observations. It was concluded that a slight reductions in surface runoff and baseflow was due to land-use change.

The overall objective of this study is to simulate the combined impact of climate change and redcedar encroachment on the water balance in the NSH including impacts on recharge. The specific objectives of this study are to: *i*) evaluate the impact of historical climate and land use on D (D), recharge (R), deep recharge (DR), and actual evapotranspiration (ET_a) (representing the main water balance components) within the study area during the historical period (2000-2019), *ii*) compare the impact of historical and most-likely climate and land use change scenario (2020-2099) on the water balance components, and *iii*) compare the impact of historical and 16 hypothetical scenarios (different combinations of redcedar encroachment and climate change) (2020-2099) on the water balance components.

4.2. Methodology

4.2.1. Study Area

The study area is the Upper Middle Loup River (UMLR) watershed (4,954 km^2), located in the NSH. The NSH, located in the western part of Nebraska, has a total area of 51,000 km^2 (Figure 4-1). It consists of sand dunes with interdunal watersheds connected with an unconfined aquifer with many lakes and wetlands, predominantly in the western part. The climate in the study area is semi-arid with mean annual P 571.04 mm yr^{-1} and mean temperature of around 9.54 °C for the historical period (2000-2019). The study area is covered by 93% pasture, 4.3% wetlands, 1.1% lakes and minimal cropland, urban and forest (Kishawi et al., 2023).
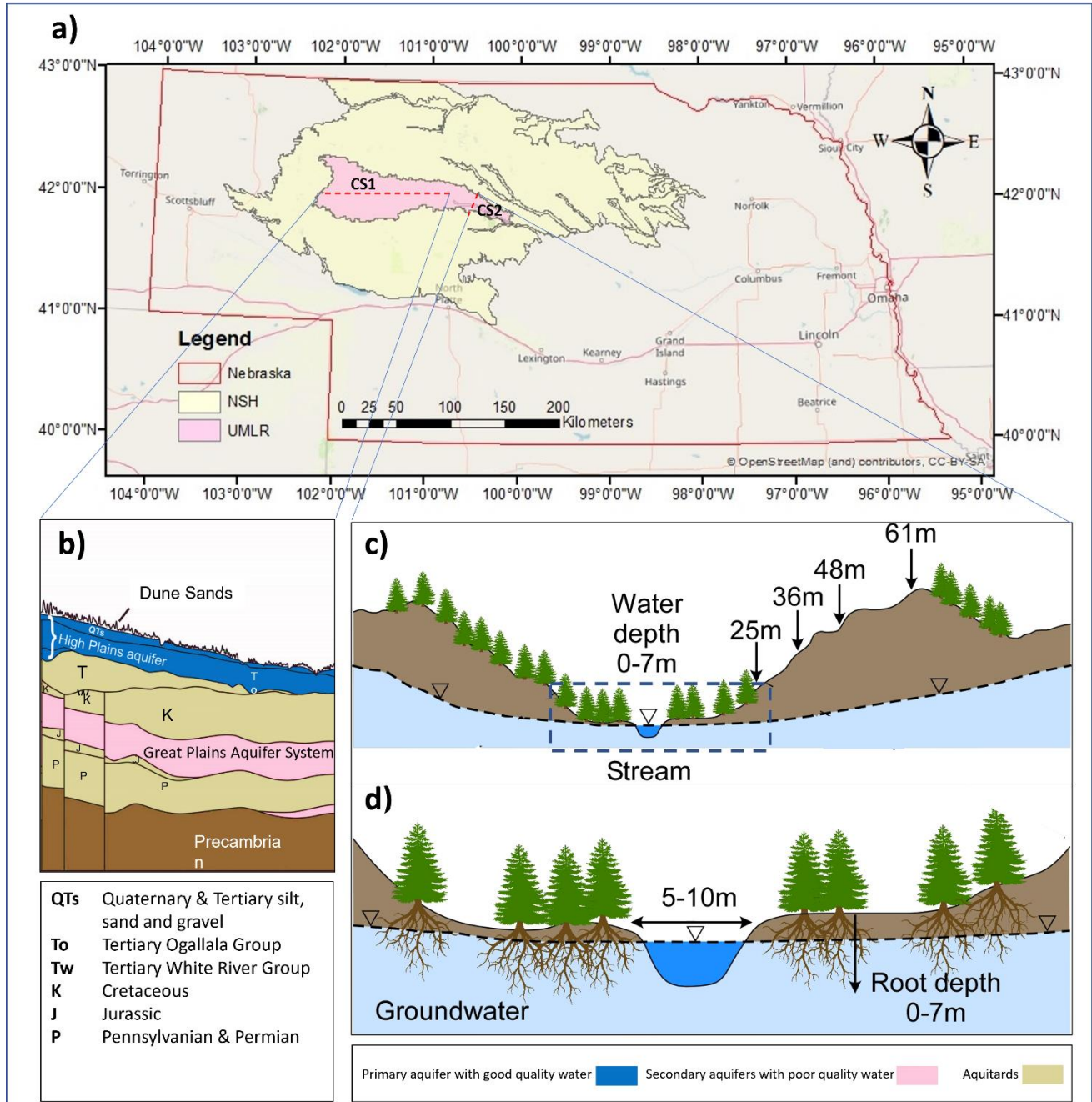
Figure 4-1: Map of the Upper Middle Loup River (UMLR) watershed (pink area) within the Nebraska Sand Hills (yellow area) and Nebraska (red line).

While currently less than 1% of the study area is covered by eastern redcedar (*Juniperus Virginiana*), 256,653 ha of grassland was converted to woody vegetation(predominantly redcedar) from 2007 to 2017 in Nebraska (Fogarty et al., 2020). Nearly 21,000 ha of Sand Hills grassland was converted to woody vegetation. The encroachment rate has increased significantly east, north and south of the UMLR watershed (Shrestha, 2022). Once controlled by wildfires, fire suppression and tree planting for windbreaks has led to

the expansion of redcedar encroachment. Redcedar, concentrated near streams and windbreaks, would encroach into the grassland.

The thickness of the High Plains Aquifer can exceed 300 m with most of the sand dunes covered with grassland. The High Plains Aquifer is composed primarily of unconsolidated, poorly sorted clay, silt, sand, and gravel and was laid 10 to 12 million years ago by fluvial deposition from streams that flowed eastward from the Rocky Mountains during the Pliocene. The High Plains Aquifer in Nebraska and South Dakota is an unconfined system composed of sedimentary deposits of Quaternary, Tertiary, and Cretaceous age. The aquifer system thins from south to north and from west to east where the base of the aquifer slopes eastward at approximately 1.5 meter per kilometer. The depth of the water table varies from surface D to more than 150 m. Generally, the aquifer is found from 15 to 90 m below the surface. Saturated thickness ranges from zero (mainly near the western edge) to about 304 m in west-central Nebraska (Sand Hills region) but overall averages around 60 m (Gutentag et al., 1984).

4.2.2. Scenario modeling approach

SWAT is a semi-distributed ecohydrological model operating on a daily time scale at a watershed scale (Arnold et al., 1998; Dile et al., 2016; Mundetia, 2019). The main components of the water balance equation are the daily change in water storage (ΔWS) as controlled by P, ET_a, and water yield. Water yield is given by the contribution of surface runoff, lateral flow, and groundwater circulation. Water yield is partially depleted by transmission losses from tributary channels and water abstractions. The D is calculated at the outlet of the UMLR watershed. The percolation represents the amount of water moving downward across the vadose zone when soil moisture exceeds field capacity. Percolation replenishes the shallow unconfined aquifer and can be assumed as R. Water stored in the shallow aquifer may replenish soil moisture in the soil profile (through upward flux induced by capillary fringe) or streamflow (through base flow or return flow). DR is the amount of water replenishing the deep confined High Plains Aquifer originating from seepage in the shallow aquifer or directly from percolation exiting through the bottom of the soil profile. All hydrological fluxes are expressed in units of mm of water height except D that is expressed as m^3 s^{-1}. As input, SWAT requires P and crop-specific potential evapotranspiration (ET_P) and is based on the concept of hydrological response units (HRUs), which are areas identified by similarities in soil, land cover, and terrain attributes. The potential root water uptake depends on soil water content and CO_2 levelsand is reduced when the soil profile does not contain sufficient water in dry periods or CO_2 level increase related to reduction in leaf conductance. SWAT typically uses the ArcSWAT interface to set up model inputs. ArcSWAT is a public domain software which works in the licensed ArcGIS environment. ArcSWAT version 2012.10._5.21 was used in this study. Kishawi et al., (2023) constructed and calibrated SWAT for the UMLR. For more details on model inputs, calibration and validation, see Kishawi et al., (2023).

The methodology adopted in this paper is shown in . SWAT was calibrated by Kishawi et al., (2023) and used in this study to perform simulations under different combinations of climate (Section 2.3) and land use change (Section 2.4) from 2000 to 2099. The D, ET_a, DR and R simulated under the historical period (2000-2019) were compared to those ones obtained under: *i*) the most likely combined land use and climate change scenario and *ii*) 16 hypothetical scenarios combining four redcedar encroachments (0.5%, 2.4%, 4.6% and 11.9%) and two extreme climate projections split in two sub-period (2020-2050 and 2051 and 2099).
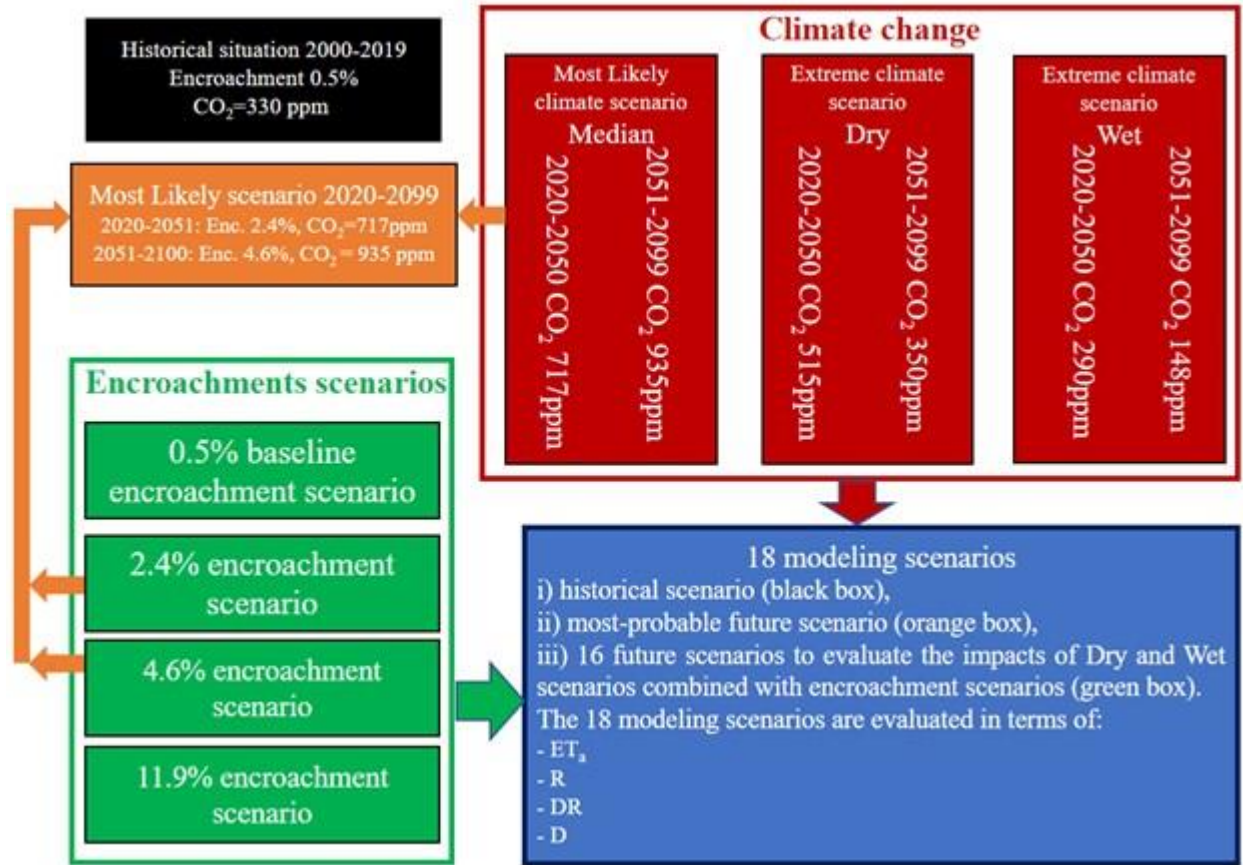
Figure 4-2: A schematic overview of the adopted methodology based on the data collected from Coupled Model Intercomparison Project (CMIP5) database and selected redcedar encroachment scenarios in the Upper Middle Loup River (UMLR) watershed. Baseline redcedar coverage is 0.5%.

Therefore, a total of 18 scenarios (blue box) were built to evaluate the simulations of the water balance components in SWAT:

1) Historical climate and land use scenario with daily climate data (CO_2 of 330 ppm) recorded between 2000 and 2019 and encroachment of 0.5% (black box in);

2) Most likely climate and land use change scenario with climate data (CO_2 of 717 ppm in 2020-2050 and CO_2 of 935 ppm in 2051-2099) estimated between 2020 and 2099 and encroachment of 2.4% in 2020-2050 and 4.6% in 2051-2099 (orange box in).

3) 16 climate and land use change scenarios combining extreme climate projections (dry and wet) split in two sub-periods (red boxes in) and four different encroachment scenarios (green boxes in).

4.2.3.Climate change scenario

The climate raw data were obtained from an ensemble of General Circulation Models (GCMs) using the Downscaled CMIP3 and CMIP5 Climate and Hydrology Projections website (Maurer et al., 2007) accessed through https://esgf-node.llnl.gov/search/cmip5/ (CMIP, 2021). The full list includes 60 models. Each model presents four Representative Concentration Pathways (RCPs, i.e., 2.6, 4.5, 6.0, and 8.5) by potentially obtaining 240 climate simulations. Since 18 sets of RCPs with corresponding climate data were missing from the remaining climate models, a total of 222 climate projections were available. Table 2.S in the Supplementary Material includes the full list of the 222 climate models with their corresponding RCPs. Through the website explorer, the coordinates of the pixels representing the study area were used to download the climate models' raw data (P, minimum, and maximum temperature) on a daily time step from 2000 and 2099. We considered the historical period from 2000 and 2019 and climate projections from 2020 and 2099. A spatial-average historical mean annual rainfall and spatial-average projected mean annual rainfall were established using 17×5 pixels (85 pixels), however only 44 pixels were within the watershed. The ET_p at daily time resolution was calculated with the Hargreaves equation based on minimum and maximum temperatures (Hargreaves and Samani, 1985). The aridity index (AI) based on the Food and Agriculture Organization (FAO) is a climate indicator which is used for measuring the degree of dryness as it is expressed as the ratio between mean annual P over ET_p (Spinoni et al., 2015). The mean annual AI values were calculated for each GCM. The 222 mean annual AI values were ranked in ascending order. Three models defined as dry, median, and wet climate scenarios were selected at 5th, 50th, and 95th percentiles, respectively, as recently done by Adane et al. (2019).

4.2.4.Land use change scenarios

The likely scenario of redcedar encroachment was created using a combination of neural network and Markov-chain cellular automata model. The current state of redcedar in 1990, 2015, and 2020 were extracted using multi-layer perceptron (MLP) neural network, trained and optimized with multiple hidden layers (3-5), regularization, and dropout parameters (Shrestha, 2022). The classified redcedar map of 1990 and 2015 were then used to calculate the transition probability using Markov-chain analysis. The transition potential was calculated using MLP with single hidden layer using environmental variables that affect the potential redcedar distribution. The variables included elevation, aspect, topographic position index, total insolation, duration of insolation, wind dispersion, distance to road, distance to windbreak, distance to stream, and depth to water table. Cellular automata method was then used to combine the transition probability and transition potential using multi-objective land allocation algorithm to predict the current (2020) and future redcedar scenarios (2050 and 2100). The predicted model of 2020 was validated against

the classified redcedar map. The model with the highest accuracy predicted an encroachment of 2.4% by 2050 and 4.6% by 2099. For more details on the MLP neural network and Markov-chain cellular automata model, refer to Shrestha (2022).

In addition to the most likely scenario, hypothetical land use scenarios were also evaluated. Hypothetical redcedar encroachment scenarios were created by combining the evergreen and mixed forest classes of 2016 National Land Cover Database (NLCD) data. With redcedar comprising at least 90% of the conifer basal area in the Great plains and at early stage of encroachment occurring as understory species, mixed forest was also included (Filippelli et al., 2020). The NLCD data derived from Landsat images at 30 m resolution do not detect such occurrences of redcedar and therefore we assumed that including the mixed forest could also compensate for undetected redcedar that are significant for future encroachment scenarios. The baseline map (0.5% redcedar) was reclassified as a binary image with the presence of redcedar represented by a value of 1 while absence by 0. A morphological filter with size between 3×3 m to 7×7 m (Haralick et al., 1987) was used to create a hypothetical scenario of different encroachment levels (Kishawi et al., 2023). Dilation is a process where a zero value in a binary image is replaced by 1, simulating the process or encroachment from established redcedar pixels.

4.3. Results

4.3.1. Historical climate and land use scenario (2000-2019)

Table 4-1 shows the annual values of P, ET_p, R, DR, ET_a, and D under the historical scenario (2000-2019). The SWAT input climate variables are P and ET_p. The mean annual P was 571.0 mm with the driest year in 2012 (P=239.7 mm) and the wettest year in 2009 (P=748.6 mm). Annual P sums are characterized by high temporal variability while annual ET_p values are close to their mean annual value.

Table 4-1: Annual P, R, DR, ETa, ETp, and D in the historical period (2000-2019) under 0.5% redcedar cover.

Year	P mm	R mm	DR mm	ET_a mm	ET_p mm	D m^3s^{-1}
2000	475.9	4.2	0.2	418.3	894.3	8.0
2001	490.4	19.5	1.0	474.2	903.7	8.1
2002	314.5	0.02	0.0	368.5	947.4	6.3
2003	456.6	12.6	0.6	419.6	884.5	6.5
2004	535.1	5.7	0.3	434.4	867.7	6.8
2005	603.0	111.9	5.6	487.8	877.9	9.6
2006	418.8	0.5	0.0	401.1	929.9	7.9
2007	580.2	34.4	1.7	476.2	925.2	8.2
2008	668.8	68.3	3.3	496.8	826.5	9.5
2009	748.6	150.5	7.6	524.4	752.8	12.6
2010	675.4	112.5	5.7	547.8	883.5	14.3
2011	698.8	113.8	5.7	516.3	804.8	14.1
2012	239.7	1.2	0.1	384.9	1041.4	10.4
2013	544.1	9.5	0.5	398.3	832.5	8.5
2014	599.8	65.7	3.3	453.0	828.3	10.8
2015	691.3	93.3	4.7	519.0	874.6	11.2

2016	616.4	65.4	3.3	546.4	915.8	11.7
2017	589.4	47.5	2.3	491.2	863.1	10.8
2018	737.0	129.7	6.5	519.2	813.1	12.7
2019	737.0	128.3	6.4	546.1	859.5	14.0
Mean	**571.0**	**58.7**	**2.9**	**471.2**	**876.3**	**10.1**
SD	**139.85**	**51.90**	**2.61**	**57.73**	**61.53**	**2.57**
CV	**24.49**	**88.37**	**88.67**	**12.25**	**7.02**	**25.04**
Min	**239.7**	**0.0**	**0.0**	**368.5**	**752.8**	**6.3**
Max	**748.6**	**150.5**	**7.6**	**547.8**	**1041.4**	**14.3**
Range	**508.9**	**150.5**	**7.6**	**179.3**	**288.6**	**8.0**

4.3.2.Most likely combined land use and climate change scenario (2020-2099)

All 222 mean annual AI-values ranged from 0.333 to 0.426 and can be grouped within the semi-arid class (0.2<AI<0.5) (Spinoni et al., 2015). The 5th (AI=0.35), 50th (AI=0.371), and 95th (AI=0.392) percentiles correspond to the climate models ACCESS1-0.1 (RCP 4.5), CMCC-CM.1 (RCP 8.5), and Ec-Earth.8 (RCP 2.6), respectively. These three climate models were selected to represent dry, median, and wet climate scenarios, respectively. illustrates the frequency distribution of mean annual AI values for each climate model in CMIP5.
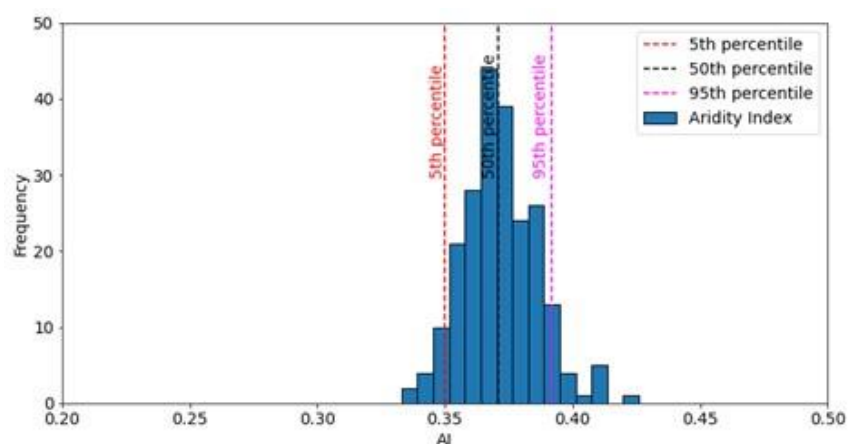
Figure 4-3: Frequency distribution of mean annual aridity index (AI) values. Vertical dashed lines depict the 5th (red line), 50th (black line), and 95th (magenta line) percentiles that denote the dry (access1-0.1), wet (cmcc-cm.1), and median (ec-earth.8) climate scenarios, respectively. The annual AI-values lie between 0.20 and 0.50 (range of the semi-arid climate class).

The median climate scenario is considered as the most likely climate projection. The mean annual P is predicted to slightly decrease by 7.6% from 571.0 mm (2000-2019) to 527.9 mm (2020-2099). The mean annual temperatures are expected to increase from 9.5 °C in the historical period (2000-2019) to 13.6 °C in the period (2051-2099). The CO_2 concentration is expected to increase to 717 ppm by 2050 and 935 ppm by 2099. The results indicate that a warming pattern will be expected with 4.1 °C increase on average over

the 100-year period, and this will be associated with lower-than-normal P and higher-than-normal ET_p. Details of P and temperatures are included in the Supplemental Material.

According to Shrestha, (2022), the most likely redcedar coverage will be 2.4% by 2050 and 4.6% by 2099 with most of the encroachment occurring around the streams and water bodies. These encroachment rates were combined with the median climate scenario and represent the most likely projection in terms of redcedar cover and future P and ET_p patterns. As shown in Table 4-2, ET_a decreased from 471.2 mm to 406.65 mm by 2050 and to 328.8 mm by 2099. The reduction in ET_a can be attributed to the root water uptake stress induced by increased CO_2 concentrations. The results showed that the minimal increase in encroachment would not have a significant impact on ET_a in the study area. Thus, CO_2 concentration has the most impact on ET_a compared to encroachment levels under the most likely scenario.

Table 4-2: Model simulations of ETa, R, DR, and D for the historical (0.5% redcedar) and most-likely scenario.

Redcedar cover	CO$_2$ ppm	2020-2050	2051-2099
		717	935
		Median climate scenario	
	P (mm)	535.70	524.00
0.5%		663.48	473.77
2.40%	ET$_p$ (mm)	663.49	*
4.60%		*	482.45
0.5%		420.08	330.91
2.40%	ET$_a$ (mm)	420.28	*
4.60%		*	341.12
0.5%		80.64	142.25
2.40%	R (mm)	81.05	*
4.60%		*	143.09
0.5%		10.2	10.3
2.40%	D (m^3 s^{-1})	13.1	*
4.60%		*	14.1
0.5%		4.03	7.11
2.40%	DR (mm)	4.05	*
4.60%		*	7.15

* The 2.4% encroachment was simulated for 2020-2050 and 4.6% was simulated for 2051-2099. Together (under the median climate scenario) they form the most-likely scenario for 2020-2099.

The impact of increased CO_2 concentrations on the plant stomata and consequently on the water balance components is shown in Figure 4-4. The increase of CO_2 level from 717 ppm (in the period 2020-2050) to 935 ppm (in the period 2051-2099) causes a reduction of 22% in the ET_a thereby increasing D by 7.6% and R by 75% between the two periods. The DR is likely to double even though it remains a residual portion of mean annual P. The model simulation provides insight into what should be expected if the encroachment conditions occurred under the most likely climate scenario in the coming 100 years.
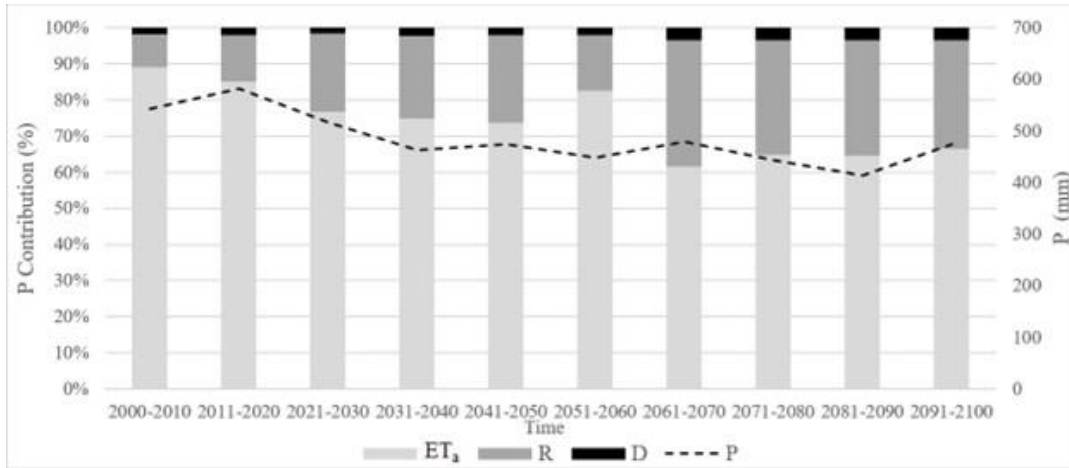
Figure 4-4: Annual simulated stacked percentages of ETa, R, and D, compared to decadal averages of P from 2000 to 2099.

Additionally, a statistical analysis of the historical (2000-2019) and projected model simulations for 2020-2050 and for 2051-2099 were performed. Table 4-3 lists the descriptive statistics of P, ET_p, D, R, and DR. Compared to the historical period, projected P, and ET_a are expected to decrease by 10%, and 14%, respectively while T and D will likely increase by 23% and 30% for the period 2020-2050. Similarly, P and ET_a will decrease by 8% and 32% while D and T will increase by 40% and 43% respectively for the period 2051-2099.

Table 4-3: Descriptive statistics of P, ETp, ETa, D and R under the historical scenario and most likely combined scenario. SD, CV, Min and Max indicate standard deviation, coefficient of variation, minimum and maximum, respectively.

Historical climate with 0.5% redcedar cover (2000-2019)					
	P (mm)	ET_p (mm)	ET_a (mm)	D ($m^3 s^{-1}$)	R (mm)	DR (mm)
Mean	571.04	876.32	471.17	10.1	58.73	2.94
SD	139.85	61.53	57.73	2.57	51.90	2.61
CV	24.49	7.02	12.25	25.40	88.37	88.67
Min	239.68	752.8	368.5	6.3	0.02	0.01
Max	748.59	1041.4	547.8	14.3	150.5	7.60
Projected median climate scenario with 2.4% encroachment (2020-2050)					
	P (mm)	ET_p (mm)	ET_a (mm)	D ($m^3 s^{-1}$)	R (mm)	DR (mm)
Mean	512.9	585.21	406.42	13.1	80.77	4.04
SD	100.8	51.73	23.31	2.2	52.53	2.58
CV	19.65	8.84	5.73	16.9	65.03	63.90
Min	341.17	499.74	358.54	9.0	2.62	0.33
Max	684.14	697.65	451.54	17.0	200.30	10.01
Projected median climate scenario with 4.6% encroachment (2051-2099)					
	P (mm)	ET_p (mm)	ET_a (mm)	D ($m^3 s^{-1}$)	R (mm)	DR (mm)
Mean	524.0	419.72	318.18	14.1	141.08	7.07
SD	87.0	37.88	15.80	3.2	65.24	3.17
CV	16.6	9.02	4.97	22.82	46.24	44.78
Min	328.76	356.85	295.09	7.3	31.92	2.06

Max	730.39	497.48	346.67	18.7	275.60	13.85

As shown in Table 4-4, we report a 38% and 37% increase in R and DR for 2020-2050 and an increase of 140% for both R and DR from 2051-2099 periods, respectively. Because climate and hydrological factors are interacting in a complex manner, analyzing these factors in isolation may not reflect the actual impacts. The sensitivities of annual ET_a, D and R to annual AI are shown in Figure 4-5. The sensitivity is quantified by comparing the change in AI to the change in the water balance components. While the sensitivities of ET_a and D to AI are weak, as indicated by the corresponding correlation coefficients ($\square$=—0.57 and $\square$= —0.34, respectively), AI shows significant impact on R as indicated by the strong positive correlation ($\square$=+0.93). The scatterplot in Figure 4-5 corroborates the reported correlation coefficients between AI and change in ET_a, D, and R.
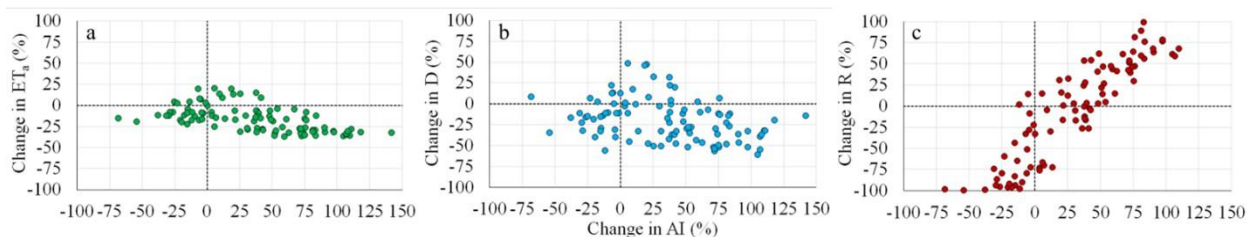
Figure 4-5: The relation between change in aridity index, AI and the change in (a) ETa (green circles), (b) D (blue circles) and, (c) R (red circles) under the most-likely combined scenario.

Table 4-4: Decadal averages of ETa, R, DR, and D and their relationship with the change in carbon dioxide (CO2), P, and temperature (T) in terms of percentage of change comparing median to historical scenario

	2000-2019	2020-2050	2051-2099	2000-2019	2020-2050	2051-2099
	mean annual values			**% of change from historical**		
ET_a (mm)	471.17	406.42	318.18	-	-14%	-32%
R (mm)	58.73	80.77	141.08	-	38%	140.2%
DR (mm)	2.94	4.04	7.07	-	37%	140.4%
D (mm)	10.1	13.1	14.1	-	30%	40%
CO_2 (ppm)	565	717	935	-	27%	65%
P (mm)	571.04	512.9	524	-	-10%	-8%
T mean (°C)	9.5	11.7	13.64		23%	43%

4.3.3.Combination of 16 hypothetical land use and extreme climate change scenarios (2020-2099)

In this section, a comparison between 16 hypothetical projected scenarios (2020-2099) and the historical scenario (2000-2019) was evaluated. For this scenario, the mean annual ET_a under the historical period is equal to 471 mm. Combined with the 4.6% encroachment level, the wet climate scenario projected a slight increase in ET_a to 476 (2020-2050) and 473 (2051-2099). For the dry climate scenario, the R increased by 0.2 mm and 1.2 mm for CO_2 levels of 515 ppm and 350 ppm, respectively. On the contrary, under the wet climate scenario the R decreased by 0.1 mm and 2.9 mm for CO_2 levels 290 ppm and 148 ppm, respectively.

When considering the change in CO_2 concentrations under the 0.5% encroachment (in the historical period 2000-2019) and compared to the projections, R decreased by 9.2 mm under the dry scenario but increased by 3.5 mm under the wet scenario. Under 11.9% encroachment and the dry climate scenario, R decreased by 10.2 mm. However, R increased by 0.3 mm under the wet scenario with 11.9% encroachment. DR slightly increased as encroachment level increases while it decreased when CO_2 decreased.

The heat maps in Figure 4-6 show the ET_a, D, and R under wet and dry scenarios over different encroachment simulations. The values range from high (red) to low (green) values. Under the dry scenario, ET_a values are lower compared to the wet scenario. Also, higher D values (red cells) are more frequent in the first period of the century (2020-2050) compared to the second period of the century (2051-2099). Results indicate that higher ET_a and lower D and R are likely to occur in the second period. The wet scenario, with RCP2.6, the projection shows lower than normal CO_2 levels. ET_p is not stressed and therefore ET_a is higher-than-normal.
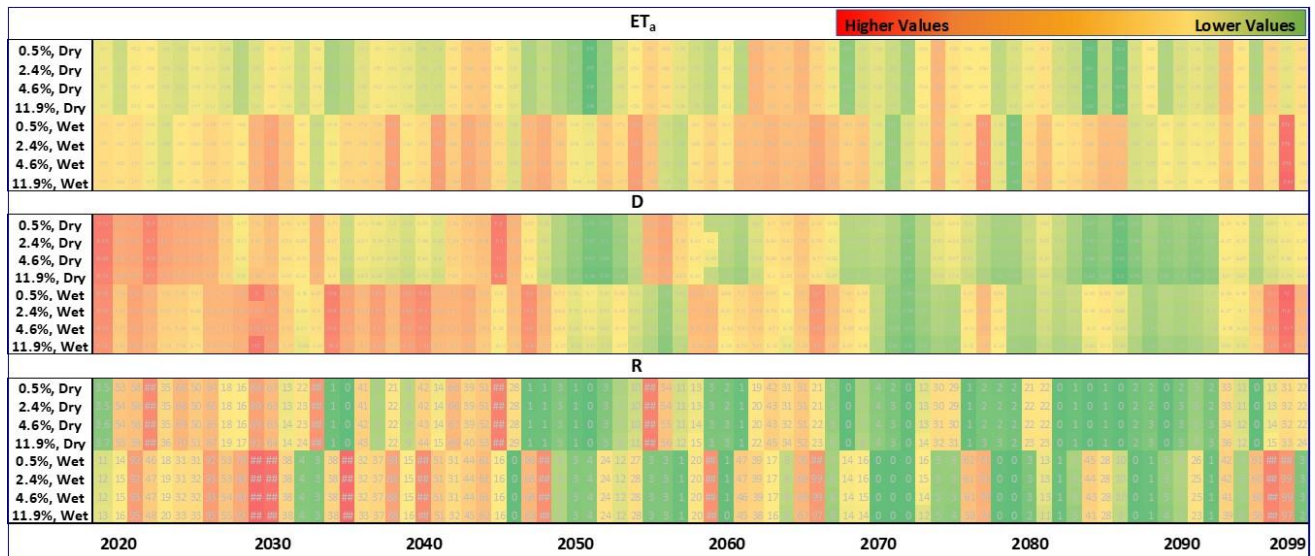
Figure 4-6: Heat maps of annual values of ETa, D and R under different combinations of encroachment scenarios from 2020-2099 (y-axis) and climate projections (x-axis) 0.5% refers to historical redcedar encroachment

As encroachment increased, D decreased under both dry and wet scenarios by less than 1 $m^3 s^{-1}$ regardless of CO_2 levels. Additionally, under the same encroachment rate, but different CO_2 concentrations, there was also a slight change in D by less than 1 $m^3 s^{-1}$. It can be concluded that different CO_2 levels had very little impact on D. The D had similar trends in the second period (2051-2099) under both dry and wet scenarios while in the first period (2020-2050) the wet scenario yielded higher D than the dry scenario.

The DR had similar trends as R under the climate and land use scenarios. As encroachment rates increased, the results indicated an increase in DR under all simulations except the wet scenario in the second period (2051-2099). Both dry and wet scenarios under the same land use conditions resulted in a reduction in DR

as the CO_2 levels increased towards the end of the century. On the contrary, the median climate scenario resulted in an increase of DR for the same period.

ET_a is more sensitive to climate change than land use change. ET_a increased by 2.6% when encroachment increased to 11.9% and increased by 3.0% from 471 to 485 mm under the wet scenario from the historical period 2000-2019 to the 2051-2099 period. This was due to the reduction in CO_2 from 365 to 100 ppm. The combined impact of encroachment and climate change caused ET_a to increase by 4.5% when considering the wet scenario and 11.9% encroachment. The largest impact of CO_2 concentration on ET_a was under the median scenario when CO_2 increased to 800 ppm (2020-2050) where there was a reduction of 33.1% compared to the first third of the century. This reduction in ET_a is due to the stomata closing as CO_2 concentrations increase. The later period 2051-2099 showed a lower reduction of 11% compared to the first period.

4.4. Discussion

4.4.1.Resource Identification Initiative

In this study we assessed how climate and land use change influenced the hydrological cycle and management of water resources in a large watershed. We adopted a modeling scenario approach to determine the most likely forecast and 16 less probable predictions to support decision-making. The approach covering the full spectrum of plausible encroachments and climate projections represents a novelty in the body of literature. This is done through evaluating the most probable combined scenario (most probable projection and well-modelled encroachment) while the other scenarios (characterized by low occurrence probability) represent a sensitivity analysis. As far as we know, this approach was used for the first time in the NSH.

Three climate scenarios (i.e., dry, wet, and median), selected according to the AI criterion, were simulated using the corresponding CO_2 levels. We gave more importance to the median climate scenario related to the highest probability of occurrence while the extremely dry (5th percentile) and wet (95th percentile) climate forecasts indicate the impact of potential climate hazard on water resources. Another novel aspect of this study is the influence of CO_2 levels on stomata closure and its impact on the most relevant water balance component output, namely the ET_a. While the default CO_2 level in the SWAT model is 330 ppm, several CO_2 projections have been used in different studies. (Kishawi et al., 2023)Ficklin et al. (2009) modeled hydrological responses of stomata closure to two CO_2 emissions (i.e., 550 and 970 ppm). Another study presented by van Liew et al., (2012) used three CO_2 levels (330 ppm, 525 ppm, 475 ppm) in SWAT from 2040 to 2059. The study did not elaborate on progressively increasing the CO_2 values over different years, rather focused on replacing baseline 330 ppm value with the new 525 and 475 ppm values based on the selected scenarios. Lee et al., (2018) used six climate scenarios to assess the impacts of various CO_2 concentrations on the water resources. This was conducted under different CO_2 emissions including 330

ppm (baseline), 590 ppm, and 850 ppm. However, in this study different RCPs have specific CO_2 emissions based on the literature review and IPCC reports (i.e., IPCC report 5). In our study, the dry, median, and wet scenarios consider RCP4.5, RCP8.5 and RCP2.6, respectively. Using data based on Pachauri et al. (2015), we varied the CO_2 concentrations for each climate scenario. With the shallow aquifer near the stream and lower parts of the sand dunes, the deep roots of redcedar can significantly impact the lateral flow and streamflow D in the watershed (Kishawi et al., 2023).

Land use change plays an important role in controlling hydrological fluxes at watershed scale. In this study we considered the most likely redcedar encroachment forecast by using a combination of neural network and Markov-chain cellular automata model. The expected increase in encroachment induced higher-than-normal R, except under the wet scenario from 2051 and 2099 when we report higher-than-normal ET_a induced by CO_2 emissions below 330 ppm. Previous studies have shown that encroachment causes an increase in percolation and DR (Zou et al., 2018). According to Zou et al., (2018), the increased infiltration is attributed to a reduction in soil bulk density associated with a reduction in compaction and an increase in soil organic matter. The reduction in compaction is a result of decreased grazing intensity (Zou et al., 2014). In this study we found that under the dry scenario, the increase in R was 59.7% of that simulated under the historical scenario. Under the same land use conditions, both dry and wet scenarios resulted in a reduction in R as the CO_2 levels increased towards the end of the century, however the median scenario resulted in an increase in 2020-2050 then followed by a lower increasing rate in 2050-2099. R was about five times larger under the wet scenario (R=159 mm) than under the dry scenario (R=30 mm) in 2020-2050.

Our results mostly reflect the findings reported in the body of literature. Increasing CO_2 concentrations will likely impact the plant stomata and guard cells by increasing root water uptake stress which will limit the potential and ET_a losses. Xu et al., (2016) indicated that under elevated CO_2, stomata tend to close because of greater depolarization causing K^+, Ca^{2+}, and Cl^- in plant guard cells to decrease while H^+ concentrations remain at high levels. This can cause the plant stomata to shut down, reduce leaf transpiration leading to an increase in D and recharge rate. Aasamaa and Sõber (2011) studied the responses of stomatal conductance to simultaneous changes in two environmental factors selected from a set of factors including air humidity, leaf water potential, air CO_2 and light intensity. The concentration of the abscisic acid (ABA) increases in the cytosol of stomatal guard cells after a decrease in leaf or air water potential. Additionally, the results indicated that the 'stomatal closing' stimuli, such as high CO_2 and darkness, cause cytosolic levels in the cells to increase. Roelfsema et al., (2004) assessed the plant hormone ABA during drought and how it depolarizes guard cells in intact plants. The study concluded that the combined activation of selected anion channels leads to the transient depolarization of guard cells where the ABA response correlates with the transient extrusion of Cl_2 from guard cells and a rapid but confined reduction in stomatal aperture.

Xu et al. (2016) also supported this conclusion by stating that elevated CO_2 concentrations are among the main factors affecting the stomata behavior. However, it was mentioned that elevated CO_2 concentrations generally cause reductions in stomatal density, stomatal conductance, leaf transpiration, and canopy/ecosystem evapotranspiration, but other factors might induce a reverse response when elevated CO_2 concentrations interact with these climatic factors.

Kishawi et al., (2023) reported that increased encroachment reduced stream D in the UMLR watershed. In this study we observed that stream D is likely to increase as higher-than-normal CO_2 concentrations are expected, by decreasing evapotranspiration losses. The results show an increase in the stream D up to 14.1 $m^3 s^{-1}$ (39.6%) compared to the historical period. As a conclusion from the sensitivity analysis (16 combined land use and climate change modeling scenarios) presented in this study, evapotranspiration, recharge, and stream D were more influenced by the change in climate rather than to the change in land use in this watershed.

However, we report some limitations in our approach that might be subject to future work improvements. The feedbacks in the soil-plant-atmosphere continuum were missing in the model set up and should be described in the future when considering the impact of climate and land use change on the hydrological cycle. Some output fluxes including water pumping from shallow and deep aquifers, transferring water outside the watershed, management practices were ignored in this study and might be included in future studies to integrate information on ecosystem services related to the water cycle. Potential improvement of this modeling scenario approach could include the simulation of soil erosion, the tracking of nitrogen and phosphorus, fertilizers and pesticides in the study area.

4.5. Conclusion

This study analyzed the hydrological responses in the Upper Middle Loup River watershed in the Nebraska Sand Hills under different redcedar encroachments and climate projections. SWAT was used to evaluate the impact of different combinations of climate and land use change on the hydrological cycle in the study area. Our results predicted a slight decrease in P but the expected increase in temperature and CO_2 levels is likely to cause the plant stomata to close, resulting in a significant reduction in evapotranspiration (specifically in the last part of this century). The CO_2 concentrations are more important than the projected P and temperature in influencing the water budget in the Upper Middle Loup River watershed.

The most probable combined land use and climate change scenario was given by two encroachment levels of 2.4% from 2020-2050 and 4.6% from 2051-2099 under the median climate projection (corresponding to the 50th percentile of the AI distribution). The results showed that an increase in CO_2 was accompanied by a dramatic decrease in ET_a and an increase in D, specifically over the last decades of the century. The decision-makers can benefit from the scenario modeling approach presented in this paper that can help support optimal management of water resources

4.6. Supplementary materials

4.6.1. Historical and future precipitation and temperature projections

The monthly mean precipitation (P) and maximum and minimum temperatures (T) based on historical values and future predictions are illustrated in Figure 4-7. The predictions of the three scenarios (wet, median, and dry) agree with the historical records in terms of the rainy months (May to July) as shown in Figure 4-7.a. July and August are the hottest months of the year in the study area as shown in Figure 4-7.b and Figure 4-7.c. July (the warmest month) has the largest differences between the historical and predicted P in wet, median, and dry scenarios with 32.6 mm, 18.2 mm, and 23.6 mm respectively, with all scenarios having less P compared to the historical period. There are fewer differences in the cooler months (October to February) ranging from 0.27 mm to 9.71 mm.
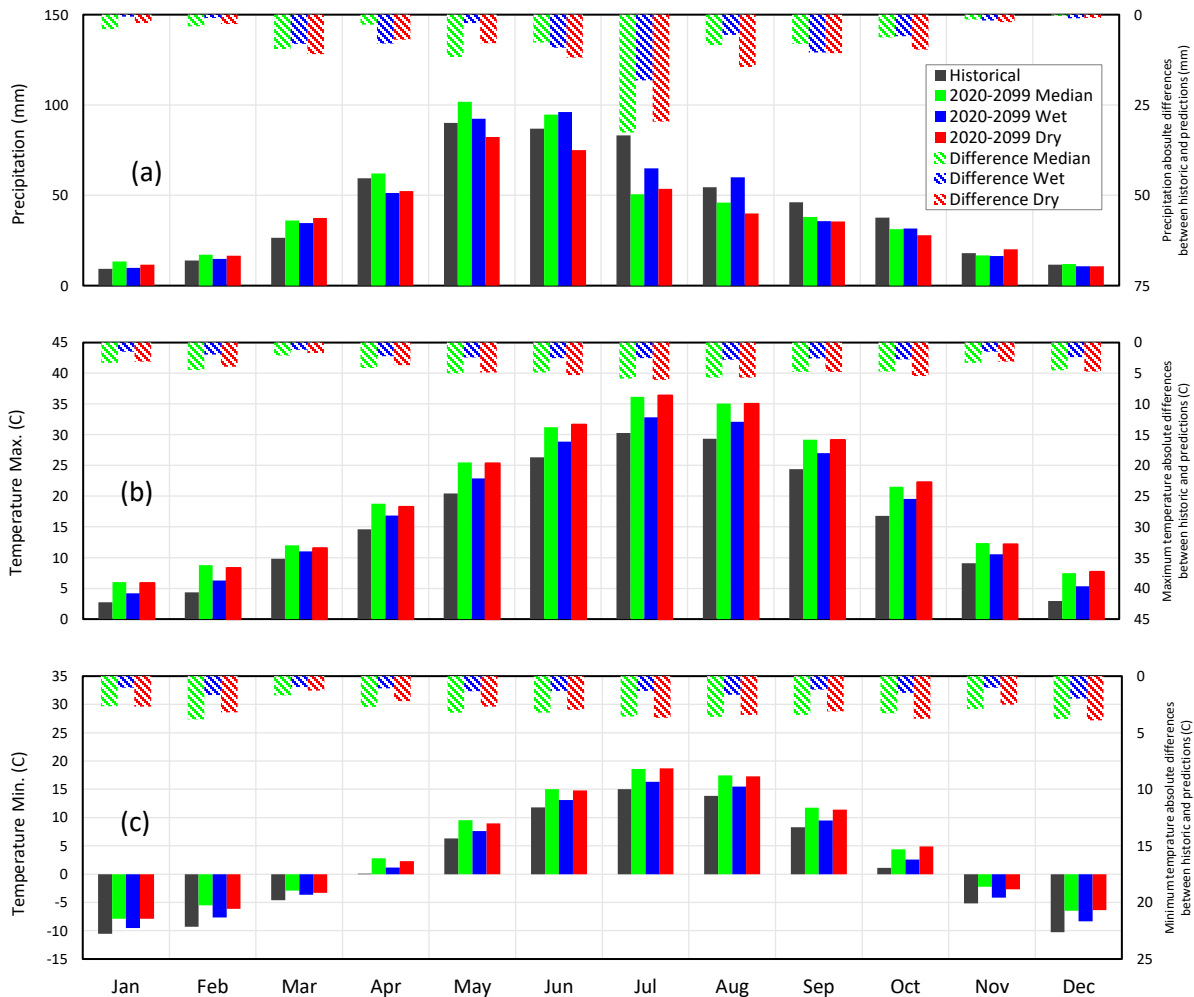
Figure 4-7: Comparing monthly average (a) precipitation, (b) maximum temperature, and (c) minimum temperature, for historical (1981-2019), future predictions (2020-2099), and the absolute differences.

The wet scenario predicts higher P in specific years (760 mm and 763 mm in years 2035 and 2040, respectively) compared to the median scenario (highest predicted year 730 mm in 2088) while the dry

scenario projects less P as expected (Figure 4-8.a). The averaged maximum and minimum temperature values indicate an increasing trend between 2020 and 2099. Looking at Figure 4-8.b and Figure 4-8c, the median and wet scenario curves have a similar pattern for both maximum and minimum temperatures. However, after the year 2070, the wet scenario tends to have higher peaks compared to the median scenario. The difference can be related to the fact that the projected T values are higher than the historical T and consequently ET0 will be higher than normal. Only in the wet scenario, the increase in ETp will be moderate.

The projected multi-year averages of P are 464 mm yr-1, 521 mm yr-1, and 520 mm yr-1, in the dry, median, and wet scenarios, respectively. This result demonstrates that the average P for the median scenario exceeds the wet scenario projection. This agrees with the results by Adane et al. (2019), where they had higher P for the median scenario multi-years-average than the wet scenario. The decadal average results show that the 100-year average precipitation for the wet, median, and dry are 524.7 mm, 525.4 mm, and 487.3 mm, respectively.

Analyzing the multi-decadal averages, it was found that both wet and dry scenarios project a steady decrease of precipitation up to 2080 (for wet) and 2090 (for dry) then an increase up to 2099. The median and wet scenarios curves predict an increasing trend of T from 2020 to 2099, where the median scenario curve is almost equivalent to the wet scenario curve. The projection indicates that temperature will rise from the historical average of 16 oC to 22 oC by the end of the 21st century (6 °C increase on average over the 100-year).
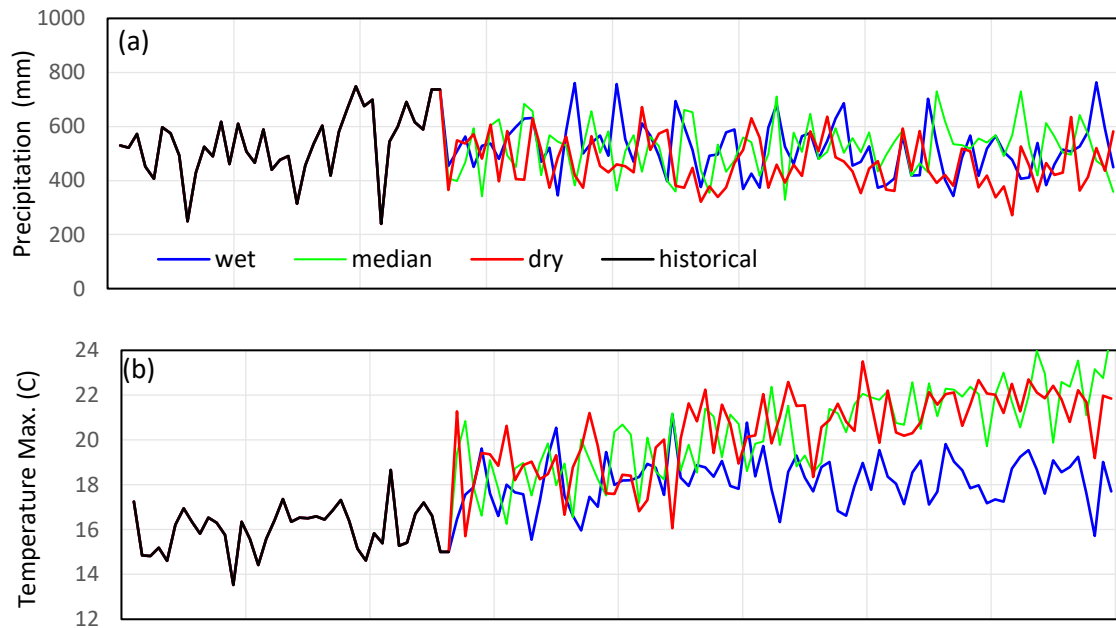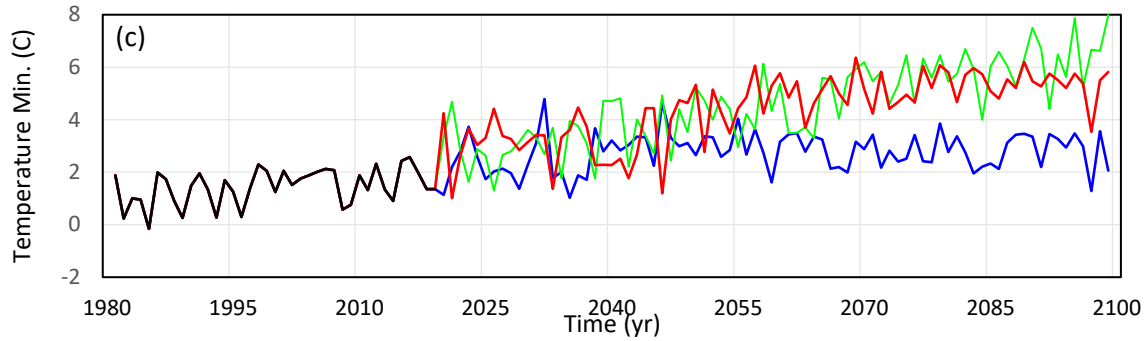
Figure 4-8: Historic and projected trends (wet, median, and dry projection) for average annual a. precipitation, b. maximum temperature, and c. minimum temperature from 1981 to 2099.

However, the dry scenario curve predicts an increase in T up to the year 2050 followed by a stable range of temperatures around 18 °C between 2050 and 2099 (2 °C increase in average over 100 years). The median scenario precipitation average was almost equivalent to the wet scenario average, however decadal averages of the wet scenario were higher than the median except for the 2070s and 2080s (Table 4-5).

Table 4-5: Average decadal precipitation (mm) for the three climate models (dry, median, and wet climate scenarios) based on historical and future predictions for the Upper Middle Loup River (UMLR) watershed.

Decade	Wet	Median	Dry
1981-1990	483	483	483
1991-2000	518	518	518
2001-2010	549	549	549
2011-2020	591	586	582
Historic Avg (mm)	**535**	**534**	**533**
2021-2030	549	531	516
2031-2040	553	507	463
2041-2050	527	511	475
2051-2060	513	485	448
2061-2070	539	545	479
2071-2080	455	525	444
2081-2090	489	545	415
2091-2099	531	519	474
Projected Avg (mm)	**519.5**	**521.0**	**464.3**

Full list of all 222 climate models

Table 0-6: List of the 222 GCMs with available RCPs that contain daily values of precipitation and minimum and maximum temperature within the study area

GCMs	RCP	GCMs	RCP	GCMs	RCP	GCMs	RCP	GCMs	RCP	GCMs	RCP
access1-0.1	4.5	ccsm4.4	4.5	csiro-mk3-6-0.2	4.5	ec-earth.8	4.5	giss-e2-r-cc.1	4.5	ipsl-cm5a-mr.1	8.5
access1-0.1	8.5	ccsm4.4	2.6	csiro-mk3-6-0.2	6.0	fgoals-g2.1	8.5	hadgem2-ao.1	8.5	ipsl-cm5a-mr.1	6.0
bcc-csm1-1.1	4.5	ccsm4.5	8.5	csiro-mk3-6-0.3	8.5	fgoals-g2.1	4.5	hadgem2-ao.1	4.5	ipsl-cm5a-mr.1	4.5
bcc-csm1-1.1	2.6	ccsm4.5	4.5	csiro-mk3-6-0.3	4.5	fgoals-g2.1	2.6	hadgem2-ao.1	2.6	ipsl-cm5a-mr.1	2.6
bcc-csm1-1.1	8.5	ccsm4.5	6.0	csiro-mk3-6-0.3	6.0	fio-esm.1	8.5	hadgem2-ao.1	6.0	ipsl-cm5b-lr.1	4.5
bcc-csm1-1.1	6.0	ccsm4.5	2.6	csiro-mk3-6-0.3	2.6	fio-esm.1	2.6	hadgem2-cc.1	8.5	ipsl-cm5b-lr.1	8.5
bcc-csm1-1-m.1	4.5	cesm1-bgc.1	8.5	csiro-mk3-6-0.4	8.5	fio-esm.1	4.5	hadgem2-cc.1	4.5	miroc5.1	4.5
bcc-csm1-1-m.1	8.5	cesm1-bgc.1	4.5	csiro-mk3-6-0.4	4.5	fio-esm.1	6.0	hadgem2-es.1	2.6	miroc5.1	8.5
canesm2.1	2.6	cesm1-cam5.1	8.5	csiro-mk3-6-0.4	6.0	fio-esm.2	6.0	hadgem2-es.1	8.5	miroc5.1	6.0
canesm2.1	4.5	cesm1-cam5.1	4.5	csiro-mk3-6-0.4	2.6	fio-esm.2	8.5	hadgem2-es.1	4.5	miroc5.1	2.6
canesm2.1	8.5	cesm1-cam5.1	6.0	csiro-mk3-6-0.5	8.5	fio-esm.2	2.6	hadgem2-es.1	6.0	miroc-esm.1	2.6
canesm2.2	2.6	cesm1-cam5.1	2.6	csiro-mk3-6-0.5	6.0	fio-esm.2	4.5	hadgem2-es.2	4.5	miroc-esm.1	8.5
canesm2.2	4.5	cesm1-cam5.2	8.5	csiro-mk3-6-0.5	4.5	fio-esm.3	2.6	hadgem2-es.2	2.6	miroc-esm.1	4.5
canesm2.2	8.5	cesm1-cam5.2	4.5	csiro-mk3-6-0.5	2.6	fio-esm.3	8.5	hadgem2-es.2	8.5	miroc-esm.1	6.0
canesm2.3	4.5	cesm1-cam5.2	2.6	csiro-mk3-6-0.6	8.5	fio-esm.3	4.5	hadgem2-es.2	6.0	miroc-esm-chem.1	4.5
canesm2.3	2.6	cesm1-cam5.3	4.5	csiro-mk3-6-0.6	6.0	fio-esm.3	6.0	hadgem2-es.3	6.0	miroc-esm-chem.1	6.0
canesm2.3	8.5	cesm1-cam5.3	6.0	csiro-mk3-6-0.6	4.5	gfdl-cm3.1	6.0	hadgem2-es.3	4.5	miroc-esm-chem.1	8.5
canesm2.4	4.5	cesm1-cam5.3	8.5	csiro-mk3-6-0.6	2.6	gfdl-cm3.1	2.6	hadgem2-es.3	8.5	miroc-esm-chem.1	2.6
canesm2.4	8.5	cesm1-cam5.3	2.6	csiro-mk3-6-0.7	8.5	gfdl-cm3.1	8.5	hadgem2-es.3	2.6	mpi-esm-lr.1	8.5
canesm2.4	2.6	cmcc-cm.1	8.5	csiro-mk3-6-0.7	2.6	gfdl-cm3.1	4.5	hadgem2-es.4	2.6	mpi-esm-lr.1	4.5
canesm2.5	2.6	cmcc-cm.1	4.5	csiro-mk3-6-0.7	6.0	gfdl-esm2g.1	2.6	hadgem2-es.4	4.5	mpi-esm-lr.1	2.6
canesm2.5	8.5	cnrm-cm5.1	8.5	csiro-mk3-6-0.7	4.5	gfdl-esm2g.1	8.5	hadgem2-es.4	6.0	mpi-esm-lr.2	2.6
canesm2.5	4.5	cnrm-cm5.1	4.5	csiro-mk3-6-0.8	8.5	gfdl-esm2g.1	6.0	hadgem2-es.4	8.5	mpi-esm-lr.2	4.5
ccsm4.1	6.0	cnrm-cm5.10	8.5	csiro-mk3-6-0.8	4.5	gfdl-esm2g.1	4.5	inmcm4.1	8.5	mpi-esm-lr.2	8.5
ccsm4.1	4.5	cnrm-cm5.2	8.5	csiro-mk3-6-0.8	2.6	gfdl-esm2m.1	6.0	inmcm4.1	4.5	mpi-esm-lr.3	8.5
ccsm4.1	8.5	cnrm-cm5.4	8.5	csiro-mk3-6-0.8	6.0	gfdl-esm2m.1	8.5	ipsl-cm5a-lr.1	4.5	mpi-esm-lr.3	2.6
ccsm4.1	2.6	cnrm-cm5.6	8.5	csiro-mk3-6-0.9	8.5	gfdl-esm2m.1	2.6	ipsl-cm5a-lr.1	8.5	mpi-esm-lr.3	4.5
ccsm4.2	8.5	csiro-mk3-6-0.1	8.5	csiro-mk3-6-0.9	4.5	gfdl-esm2m.1	4.5	ipsl-cm5a-lr.1	2.6	mpi-esm-mr.1	4.5
ccsm4.2	6.0	csiro-mk3-6-0.1	6.0	csiro-mk3-6-0.9	2.6	giss-e2-h-cc.1	4.5	ipsl-cm5a-lr.1	6.0	mpi-esm-mr.1	8.5
ccsm4.2	2.6	csiro-mk3-6-0.1	2.6	csiro-mk3-6-0.9	6.0	giss-e2-r.1	8.5	ipsl-cm5a-lr.2	8.5	mpi-esm-mr.1	2.6
ccsm4.2	4.5	csiro-mk3-6-0.1	4.5	ec-earth.12	8.5	giss-e2-r.1	4.5	ipsl-cm5a-lr.2	4.5	mri-cgcm3.1	4.5

ccsm4.3	8.5	csiro-mk3-6-0.10	8.5	ec-earth.12	4.5	giss-e2-r.1	6.0	ipsl-cm5a-lr.2	2.6	mri-cgcm3.1	2.6
ccsm4.3	4.5	csiro-mk3-6-0.10	4.5	ec-earth.12	2.6	giss-e2-r.1	2.6	ipsl-cm5a-lr.3	4.5	mri-cgcm3.1	8.5
ccsm4.3	2.6	csiro-mk3-6-0.10	6.0	ec-earth.2	4.5	giss-e2-r.2	4.5	ipsl-cm5a-lr.3	8.5	noresm1-m.1	4.5
ccsm4.3	6.0	csiro-mk3-6-0.10	2.6	ec-earth.6	8.5	giss-e2-r.3	4.5	ipsl-cm5a-lr.3	2.6	noresm1-m.1	8.5
ccsm4.4	6.0	csiro-mk3-6-0.2	8.5	ec-earth.8	8.5	giss-e2-r.4	4.5	ipsl-cm5a-lr.4	8.5	noresm1-m.1	6.0
ccsm4.4	8.5	csiro-mk3-6-0.2	2.6	ec-earth.8	2.6	giss-e2-r.5	4.5	ipsl-cm5a-lr.4	4.5	noresm1-m.1	2.6

References:

Aasamaa, K., Sober, A., 2011. Responses of stomatal conductance to simultaneous changes in two environmental factors. Tree Physiol. 31, 855–864. https://doi.org/10.1093/treephys/tpr078

Adane, Z., Nasta, P., Gates, J.B., 2017. Links between soil hydrophobicity and groundwater recharge under plantations in a sandy grassland setting, Nebraska Sand Hills, USA. For. Sci. 63, 388–401. https://doi.org/10.5849/FS-2016-137

Adane, Z., Zlotnik, V.A., Rossman, N.R., Wang, T., Nasta, P., 2019a. Sensitivity of potential groundwater recharge to projected climate change scenarios: A site-specific study in the Nebraska Sand Hills, USA. Water (Switzerland) 11. https://doi.org/10.3390/w11050950

Adane, Z., Zlotnik, V.A., Rossman, N.R., Wang, T., Nasta, P., Adane, Z., Zlotnik, V.A., Rossman, N.R., Wang, T., Nasta, P., 2019b. Sensitivity of Potential Groundwater Recharge to Projected Climate Change Scenarios: A Site-Specific Study in the Nebraska Sand Hills, USA. Water 11, 950. https://doi.org/10.3390/w11050950

Adane, Z.A., Gates, J.B., 2014. Détermination des impacts d'une plantation forestière expérimentale sur la recharge des aquifères dans les Sand Hills du Nebraska (USA) en utilisant des chlorures et du sulfate. Hydrogeol. J. 23, 81–94. https://doi.org/10.1007/s10040-014-1181-6

Adane, Z.A., Nasta, P., Zlotnik, V., Wedin, D., 2018. Impact of grassland conversion to forest on groundwater recharge in the Nebraska Sand Hills. J. Hydrol. Reg. Stud. 15, 171–183. https://doi.org/10.1016/j.ejrh.2018.01.001

Adeyemi, O., Grove, I., Peets, S., Norton, T., 2017. Advanced monitoring and management systems for improving sustainability in precision irrigation. Sustain. 9, 1–29. https://doi.org/10.3390/su9030353

Afinowicz, J.D., Munster, C.L., Wilcox, B.P., 2005. Modeling effects of brush management on the Rangeland water budget: Edwards Plateau, Texas. J. Am. Water Resour. Assoc. 41, 181–193. https://doi.org/10.1111/j.1752-1688.2005.tb03727.x

Ahl, R.S., Woods, S.W., Zuuring, H.R., 2008. Hydrologic calibration and validation of SWAT in a snow-dominated Rocky Mountain watershed, Montana, U.S.A. J. Am. Water Resour. Assoc. 44, 1411–1430. https://doi.org/10.1111/j.1752-1688.2008.00233.x

Ahlbrandt, T.S., Fryberger, S.G., 1980. Eolian deposits in the Nebraska sand hills. US Geol. Surv. Prof. Pap. 1120, 1–24.

Aksoy, H., Kaptan, S., 2020. Simulation of future forest and land use/cover changes (2019–2039) using the cellular automata-Markov model. Geocarto Int. https://doi.org/10.1080/10106049.2020.1778102

Alvarez-Taboada, F., Paredes, C., Julián-Pelaz, J., 2017. Mapping of the Invasive Species Hakea sericea Using Unmanned Aerial Vehicle (UAV) and WorldView-2 Imagery and an Object-Oriented Approach. Remote Sens. 9, 913. https://doi.org/10.3390/rs9090913

American Ground Water Trust, 2002. OGALLALA AQUIFER | American Ground Water Trust [WWW Document]. URL https://agwt.org/content/ogallala-aquifer-0 (accessed 6.6.22).

Anadón, J.D., Sala, O.E., Maestre, F.T., 2014a. Climate change will increase savannas at the expense of forests and treeless vegetation in tropical and subtropical Americas. J. Ecol. 102, 1363–1373. https://doi.org/10.1111/1365-2745.12325

Anadón, J.D., Sala, O.E., Turner, B.L., Bennett, E.M., 2014b. Effect of woody-plant encroachment on livestock production in North and South America. Proc. Natl. Acad. Sci. U. S. A. 111, 12948–12953. https://doi.org/10.1073/pnas.1320585111

Anderson D., M., 2003. Juniperus virginiana. In: Fire Effects Information System [WWW Document]. URL https://www.wildflower.org/expert/show.php?id=11335

Anderson, M.D., 2003. SPECIES: Juniperus virginiana [WWW Document]. URL https://www.fs.fed.us/database/feis/plants/tree/junvir/all.html#:~:text=Eastern redcedar has a generally,)%5B26%2C142%5D.

Andrew, M.E., Ustin, S.L., 2009. Habitat suitability modelling of an invasive plant with advanced remote sensing data. Divers. Distrib. 15, 627–640. https://doi.org/10.1111/j.1472-4642.2009.00568.x

Arévalo, P., Olofsson, P., Woodcock, C.E., 2020. Continuous monitoring of land change activities and post-disturbance dynamics from Landsat time series: A test methodology for REDD+ reporting. Remote Sens. Environ. 238, 111051. https://doi.org/10.1016/j.rse.2019.01.013

Arnold, J.G., Srinivasan, R., Muttiah, R.S., Williams, J.R., 1998. Large area hydrologic modeling and assessment part I: Model development. J. Am. Water Resour. Assoc. https://doi.org/10.1111/j.1752-1688.1998.tb05961.x

Arsanjani, J.J., Kainz, W., Mousivand, A.J., 2011. Tracking dynamic land-use change using spatially explicit markov chain based on cellular automata: The case of Tehran. Int. J. Image Data Fusion 2, 329–345. https://doi.org/10.1080/19479832.2011.605397

Asner, G.P., Archer, S., Hughes, R.F., Ansley, R.J., Wessman, C.A., 2003. Net changes in regional woody vegetation cover and carbon storage in Texas drylands, 1937-1999. Glob. Chang. Biol. 9, 316–335. https://doi.org/10.1046/j.1365-2486.2003.00594.x

Awada, T., El-Hage, R., Geha, M., Wedin, D.A., Huddle, J.A., Zhou, X., Msanne, J., Sudmeyer, R.A., Martin, D.L., Brandle, J.R., 2013. Intra-annual variability and environmental controls over transpiration in a 58-year-old even-aged stand of invasive woody Juniperus virginiana L. in the Nebraska Sandhills, USA. Ecohydrology 6, 731–740. https://doi.org/10.1002/eco.1294

Axmann, B.D., Knapp, A.K., 1993. Water Relations of Juniperus virginiana and Andropogon Gerardii in an Unburned Tallgrass Prairie Watershed Author (s): Beverly D . Axmann and Alan K . Knapp Source : The Southwestern Naturalist , Dec ., 1993 , Vol . 38 , No . 4 (Dec ., 1993), pp . 325 38, 325–330.

Baidar, T., Shrestha, A.B., Ranjit, R., Adhikari, R., Ghimire, S., Shrestha, N., 2017. Impact assessment of mikania micrantha on land cover and maxent modeling to predict its potential invasion sites, in: International Archives of the Photogrammetry, Remote Sensing and Spatial Information Sciences - ISPRS Archives. https://doi.org/10.5194/isprs-archives-XLII-1-W1-305-2017

Bailey, R.T., Wible, T.C., Arabi, M., Records, R.M., Ditty, J., 2016. Assessing regional-scale spatio-temporal patterns of groundwater–surface water interactions using a coupled SWAT-MODFLOW model. Hydrol. Process. 30, 4420–4433. https://doi.org/10.1002/hyp.10933

Balzter, H., 2000. Markov chain models for vegetation dynamics. Ecol. Modell. 126, 139–154. https://doi.org/10.1016/S0304-3800(00)00262-3

Barger, N.N., Archer, S.R., Campbell, J.L., Huang, C., Morton, J.A., Knapp, A.K., 2011. Woody plant proliferation in North American drylands: A synthesis of impacts on ecosystem carbon balance. J. Geophys. Res. 116, G00K07. https://doi.org/10.1029/2010JG001506

Barnes, P.W., Harrison, A.T., Heinisch, S.P., 1984. Vegetation patterns in relation to topography and edaphic variation Nebraska Sandhills prairie.

Barten, A.P., 1987. The coefficient of determination for regression without a constant term 181–189. https://doi.org/10.1007/978-94-009-3591-4_12

Bechtold, W.A., 2003. Crown-Diameter Prediction Models for 87 Species of Stand-Grown Trees in the Eastern United States. South. J. Appl. For. 27, 269–278. https://doi.org/10.1093/sjaf/27.4.269

Belgiu, M., Drăgu, L., 2016. Random forest in remote sensing: A review of applications and future directions. ISPRS J. Photogramm. Remote Sens. 114, 24–31. https://doi.org/10.1016/J.ISPRSJPRS.2016.01.011

Benz, U.C., Hofmann, P., Willhauck, G., Lingenfelder, I., Heynen, M., 2004. Multi-resolution, object-oriented fuzzy analysis of remote sensing data for GIS-ready information. ISPRS J. Photogramm. Remote Sens. 58, 239–258. https://doi.org/10.1016/J.ISPRSJPRS.2003.10.002

Bielski, C.H., Twidwell, D., Allen, C.R., 2017. Eastern Redcedar Science Literacy Project | Department of Agronomy and Horticulture | Nebraska [WWW Document]. URL https://agronomy.unl.edu/eastern-redcedar-science-literacy-project (accessed 5.25.21).

Billesbach, D.P., Arkebauer, T.J., 2012. First long-term, direct measurements of evapotranspiration and surface water balance in the Nebraska SandHills. Agric. For. Meteorol. 156, 104–110. https://doi.org/10.1016/j.agrformet.2012.01.001

Bishop, Y.M.M., Fienberg, S., Holland, P., 1975. Discrete multivariate analysis: theory and practice MIT Press. Cambridge, Massachusetts.

Bradley, B.A., 2014. Remote detection of invasive plants: A review of spectral, textural and phenological approaches. Biol. Invasions 16, 1411–1425. https://doi.org/10.1007/s10530-013-0578-9

Briggs, J.M., Hoch, G.A., Johnson, L.C., 2002. Assessing the rate, mechanisms, and consequences of the conversion of tallgrass prairie to Juniperus virginian a forest. Ecosystems 5, 578–586. https://doi.org/10.1007/s10021-002-0187-4

Brown, J.R., Archer, S., 1999. Shrub invasion of grassland: Recruitment is continuous and not regulated by herbaceous biomass or density. Ecology 80, 2385–2396. https://doi.org/10.1890/0012-9658(1999)080[2385:SIOGRI]2.0.CO;2

Bullock, E.L., Nolte, C., Segovia, A.R., Woodcock, C.E., 2020. Ongoing forest disturbance in Guatemala's protected areas. Remote Sens. Ecol. Conserv. 6, 141–152. https://doi.org/10.1002/RSE2.130

Burbach, M.E., Joeckel, R.M., 2006. A delicate balance: Rainfall and groundwater in Nebraska during the 2000-2005 drought. Gt. Plains Res. 16, 5–16.

Camacho Olmedo, M.T., Paegelow, M., Mas, J.F., 2013. Interest in intermediate soft-classified maps in land change model validation: suitability versus transition potential. Int. J. Geogr. Inf. Sci. 27, 2343–2361. https://doi.org/10.1080/13658816.2013.831867

Camacho Olmedo, M.T., Pontius, R.G., Paegelow, M., Mas, J.-F., 2015. Comparison of simulation models in terms of quantity and allocation of land change. Environ. Model. Softw. 69, 214–221. https://doi.org/10.1016/j.envsoft.2015.03.003

CMIP, 2021. Downscaled CMIP3 and CMIP5 Climate and Hydrology Projections [WWW Document]. URL https://gdo-dcp.ucllnl.org/downscaled_cmip_projections/dcpInterface.html#Projections: Subset Request (accessed 7.8.21).

Cochran, W.G. (William G., 1963. Sampling techniques, 2d ed. ed, A Wiley publication in applied statistics. Wiley, New York.

Cohen, W.B., Spies, T.A., 1992. Estimating structural attributes of Douglas-fir/western hemlock forest stands from landsat and SPOT imagery. Remote Sens. Environ. 41, 1–17. https://doi.org/10.1016/0034-4257(92)90056-P

Conrad, O., Bechtel, B., Bock, M., Dietrich, H., Fischer, E., Gerlitz, L., Wehberg, J., Wichmann, V., Böhner, J., 2015. System for automated geoscientific analyses (SAGA) v. 2.1. 4. Geosci. Model Dev. Discuss. 8, 1991–2007. https://doi.org/10.5194/gmd-8-1991-2015

Coop, J.D., Givnish, T.J., 2007. Spatial and temporal patterns of recent forest encroachment in montane grasslands of the Valles Caldera, New Mexico, USA. J. Biogeogr. 34, 914–927. https://doi.org/10.1111/j.1365-2699.2006.01660.x

Copass, C., Antonova, N., Kennedy, R., 2018. Comparison of Office and Field Techniques for Validating Landscape Change Classification in Pacific Northwest National Parks. Remote Sens. 2019, Vol. 11, Page 3 11, 3. https://doi.org/10.3390/RS11010003

Coppedge, B.R., Engle, D.M., Fuhlendorf, S.D., 2007. Markov models of land cover dynamics in a southern Great Plains grassland region. Landsc. Ecol. 22, 1383–1393. https://doi.org/10.1007/s10980-007-9116-4

Cordova, C.E., Johnson, W.C., Mandel, R.D., Palmer, M.W., 2011. Late Quaternary environmental change inferred from phytoliths and other soil-related proxies: Case studies from the central and southern Great Plains, USA. Catena 85, 87–108. https://doi.org/10.1016/j.catena.2010.08.015

Cowen, D.J., Jensen, J.R., Bresnahan, P.J., Ehler, G.G., Graves, D., Huang Xueqiao, Wiesner, C., Mackey, H.E., 1995. The design and implementation of an integrated geographic information system for environmental applications. Photogramm. Eng. Remote Sensing 61, 1393–1404.

Crist, E.P., Cicone, R.C., 1984. A Physically-Based Transformation of Thematic Mapper Data—The TM Tasseled Cap. IEEE Trans. Geosci. Remote Sens. GE-22, 256–263. https://doi.org/10.1109/TGRS.1984.350619

Dappen, P., Merchant, J., Ratcliffe, I., Robbins, C., 2007. Delineation of 2005 land use patterns for the state of Nebraska. Lincoln, NE Cent. Adv. L. Manag. Inf. Technol. Sch. Nat. Resour. Univ. Nebraska-Lincoln.

Del Frate, F., Pacifici, F., Schiavon, G., Solimini, C., 2007. Use of neural networks for automatic classification from high-resolution images. IEEE Trans. Geosci. Remote Sens. 45, 800–809. https://doi.org/10.1109/TGRS.2007.892009

Dewitz, J., 2019. National Land Cover Database (NLCD) 2016 Products [WWW Document]. U.S. Geol. Surv. data release. https://doi.org/10.5066/P96HHBIE

Dhami, B., Himanshu, S.K., Pandey, A., Gautam, A.K., 2018. Evaluation of the SWAT model for water balance study of a mountainous snowfed river basin of Nepal. Environ. Earth Sci. 77, 1–20. https://doi.org/10.1007/s12665-017-7210-8

Dile, Y.T., Daggupati, P., George, C., Srinivasan, R., Arnold, J., 2016. Introducing a new open source GIS user interface for the SWAT model. Environ. Model. Softw. 85, 129–138. https://doi.org/10.1016/j.envsoft.2016.08.004

Doungmanee, P., 2016. The nexus of agricultural water use and economic development level. Kasetsart J. Soc. Sci. 37, 38–45. https://doi.org/10.1016/j.kjss.2016.01.008

Eastman, J.R., Toledano, J., 2018. A Short Presentation of the Land Change Modeler (LCM). Springer, Cham, pp. 499–505. https://doi.org/10.1007/978-3-319-60801-3_36

Eastman, J.R., Van Fossen, M.E., Solarzano, L.A., 2005. Transition potential modeling for land cover change. GIS, Spat. Anal. Model. 17, 357–386.

Eggemeyer, K.D., Awada, T., Harvey, F.E., Wedin, D.A., Zhou, X., Zanner, C.W., 2009. Seasonal changes in depth of water uptake for encroaching trees Juniperus virginiana and Pinus ponderosa and two dominant C4 grasses in a semiarid grassland. Tree Physiol. 29, 157–169. https://doi.org/10.1093/treephys/tpn019

Eldridge, D.J., Bowker, M.A., Maestre, F.T., Roger, E., Reynolds, J.F., Whitford, W.G., 2011. Impacts of shrub encroachment on ecosystem structure and functioning: Towards a global synthesis. Ecol. Lett. 14, 709–722. https://doi.org/10.1111/j.1461-0248.2011.01630.x

Engle, D.M., Coppedge R., B., Fuhlendorf D., S., 2008. From the Dust Bowl to the Green Glacier: Human Activity and Environmental Change in Great Plains Grasslands. West. North Am. Juniperus Communities 53–78. https://doi.org/10.1007/978-0-387-34003-6_14

Ercan, M.B., Maghami, I., Bowes, B.D., Morsy, M.M., Goodall, J.L., 2020. Estimating Potential Climate Change Effects on the Upper Neuse Watershed Water Balance Using the SWAT Model. J. Am. Water Resour. Assoc. 56, 53–67. https://doi.org/10.1111/1752-1688.12813

Erdody, T.L., Moskal, L.M., 2010. Fusion of LiDAR and imagery for estimating forest canopy fuels. Remote Sens. Environ. 114, 725–737. https://doi.org/10.1016/J.RSE.2009.11.002

Evenson, G.R., Golden, H.E., Lane, C.R., D'Amico, E., 2016. An improved representation of geographically isolated wetlands in a watershed-scale hydrologic model. Hydrol. Process. 30, 4168–4184. https://doi.org/10.1002/hyp.10930

Evenson, G.R., Golden, H.E., Lane, C.R., D'Amico, E., 2015. Geographically isolated wetlands and watershed hydrology: A modified model analysis. J. Hydrol. 529, 240–256. https://doi.org/10.1016/j.jhydrol.2015.07.039

Evenson, G.R., Golden, H.E., Lane, C.R., McLaughlin, D.L., D'Amico, E., 2018. Depressional wetlands affect watershed hydrological, biogeochemical, and ecological functions. Ecol. Appl. 28, 953–966. https://doi.org/10.1002/eap.1701

Falkowski, M.J., Evans, J.S., Naugle, D.E., Hagen, C.A., Carleton, S.A., Maestas, J.D., Khalyani, A.H., Poznanovic, A.J., Lawrence, A.J., 2017. Mapping Tree Canopy Cover in Support of Proactive Prairie Grouse Conservation in Western North America. Rangel. Ecol. Manag. 70, 15–24. https://doi.org/10.1016/J.RAMA.2016.08.002

Fant, C., Srinivasan, R., Boehlert, B., Rennels, L., Chapra, S.C., Strzepek, K.M., Corona, J., Allen, A., Martinich, J., 2017. Climate change impacts on us water quality using two models: HAWQS and US basins. Water (Switzerland) 9. https://doi.org/10.3390/w9020118

FAO, 2017. Water for Sustainable Food and Agriculture Water for Sustainable Food and Agriculture, A report produced for the G20 Presidency of Germany.

Fassnacht, F.E., Latifi, H., Stereńczak, K., Modzelewska, A., Lefsky, M., Waser, L.T., Straub, C., Ghosh, A., 2016. Review of studies on tree species classification from remotely sensed data. Remote Sens. Environ. 186, 64–87. https://doi.org/10.1016/J.RSE.2016.08.013

Ferguson, E.R., Lawson, E.R., Maple, W.R., Mesavage, C., Forest, S., Station, E., Nelson, T.C., Service, F., 1968. Managing Eastern Redcedar.

Ficklin, D.L., Luo, Y., Luedeling, E., Zhang, M., 2009. Climate change sensitivity assessment of a highly agricultural watershed using SWAT. J. Hydrol. 374, 16–29. https://doi.org/10.1016/j.jhydrol.2009.05.016

Filippelli, S.K., Vogeler, J.C., Falkowski, M.J., Meneguzzo, D.M., 2020. Monitoring conifer cover: Leaf-off lidar and image-based tracking of eastern redcedar encroachment in central Nebraska. Remote Sens. Environ. 248, 111961. https://doi.org/10.1016/j.rse.2020.111961

Fogarty, D.T., Roberts, C.P., Uden, D.R., Donovan, V.M., Allen, C.R., Naugle, D.E., Jones, M.O., Allred, B.W., Twidwell, D., 2020. Woody plant encroachment and the sustainability of priority conservation areas. Sustain. 12, 1–15. https://doi.org/10.3390/su12208321

Forest Service, U., 2020. Forests of Nebraska, 2019, Resource Update FS-237. Madison, WI: U.S. Department of Agriculture Forest Service, Northern Research Station. https://doi.org/10.2737/FS-RU-237

Fowler, C., Konopik, E., 2007. The History of Fire in the Southern United States. Hum. Ecol. Rev. 14, 165–176.

Géron, A., 2019. Hands-On Machine Learning with Scikit-Learn, Keras, and TensorFlow: Concepts, Tools, and Techniques to Build Intelligent Systems. O'Reilly Media.

Ghosh, A., Fassnacht, F.E., Joshi, P.K., Kochb, B., 2014. A framework for mapping tree species combining hyperspectral and LiDAR data: Role of selected classifiers and sensor across three spatial scales. Int. J. Appl. Earth Obs. Geoinf. 26, 49–63. https://doi.org/10.1016/j.jag.2013.05.017

Gilman, E.F., Watson, D.G., 1993. Juniperus virginiana Eastern Redcedar 32611.

Gilmore, T.E., Zlotnik, V., Johnson, M., 2019. Recognition of Regional Water Table Patterns for Estimating Recharge Rates in Shallow Aquifers. Groundwater 57, 443–454. https://doi.org/10.1111/gwat.12808

Giulia Lembo Caterina, 2012. Juniperus Virginiana Encroachment Into Mesic Grasslands: Rainfall Interception And Tree Water Use. Master Degree Dessirtation 53, 1689–1699.

Gong, P., Wang, J., Yu, L., Zhao, Yongchao, Zhao, Yuanyuan, Liang, L., Niu, Z., Huang, X., Fu, H., Liu, S., Li, C., Li, X., Fu, W., Liu, C., Xu, Y., Wang, X., Cheng, Q., Hu, L., Yao, W., Zhang, Han, Zhu, P., Zhao, Z., Zhang, Haiying, Zheng, Y., Ji, L., Zhang, Y., Chen, H., Yan, A., Guo, J., Yu, Liang, Wang, L., Liu, X., Shi, T., Zhu, M., Chen, Y., Yang, G., Tang, P., Xu, B., Giri, C., Clinton, N., Zhu, Z., Chen, Jin, Chen, Jun, 2012. Finer resolution observation and monitoring of global land cover: first mapping results with Landsat TM and ETM+ data. http://dx.doi.org/10.1080/01431161.2012.748992 34, 2607–2654. https://doi.org/10.1080/01431161.2012.748992

Gosselin, D.C., Sridhar, V., Harvey, F.E., Goeke, J.W., 2006. Hydrological effects and groundwater fluctuations in interdunal environments in the Nebraska Sandhills. Gt. Plains Res. 16, 17–28.

Guan, D., Li, H., Inohae, T., Su, W., Nagaie, T., Hokao, K., 2011. Modeling urban land use change by the integration of cellular automaton and Markov model. Ecol. Modell. 222, 3761–3772. https://doi.org/10.1016/j.ecolmodel.2011.09.009

Gutentag, E.D., Heimes, F.J., Krothe, N.C., Luckey, R.R., Weeks, J.B., 1984. Geohydrology of the High Plains aquifer in parts of Colorado, Kansas, Nebraska, New Mexico, Oklahoma, South Dakota, Texas, and Wyoming (USGS, USA, groundwater). US Geol. Surv. Prof. Pap. 1400 B. https://doi.org/10.3133/pp1400B

Haacker, E.M.K., Kendall, A.D., Hyndman, D.W., 2016a. Water Level Declines in the High Plains Aquifer: Predevelopment to Resource Senescence. Groundwater 54, 231–242. https://doi.org/10.1111/gwat.12350

Haacker, E.M.K., Kendall, A.D., Hyndman, D.W., 2016b. Water Level Declines in the High Plains Aquifer: Predevelopment to Resource Senescence. Groundwater 54, 231–242. https://doi.org/10.1111/gwat.12350

Hansen, S.P., Messer, T.L., Mittelstet, A.R., 2019. Mitigating the risk of atrazine exposure: Identifying hot spots and hot times in surface waters across Nebraska, USA. J. Environ. Manage. 250, 109424. https://doi.org/10.1016/j.jenvman.2019.109424

Haralick, R.M., R., S.S., Xinhua, Z., 1987a. Image Analysis Using Mathematical Morphology. IEEE Transcations Pattern Anal. Mach. Intell. PAMI-9, 532–550.

Haralick, R.M., Sternberg, S.R., Zhuang, X., 1987b. Image Analysis Using Mathematical Morphology. IEEE Trans. Pattern Anal. Mach. Intell. PAMI-9, 532–550. https://doi.org/10.1109/TPAMI.1987.4767941

Hargreaves, Samani, 1985. Reference Crop Evapotranspiration from Temperature. Appl. Eng. Agric. 1, 96–99. https://doi.org/10.13031/2013.26773

He, D., Shi, Q., Liu, X., Zhong, Y., Zhang, X., 2021. Deep Subpixel Mapping Based on Semantic Information Modulated Network for Urban Land Use Mapping. IEEE Trans. Geosci. Remote Sens. 59, 10628–10646. https://doi.org/10.1109/TGRS.2021.3050824

He, K., Zhang, X., Ren, S., Sun, J., 2016. Deep residual learning for image recognition, in: Proceedings of the IEEE Computer Society Conference on Computer Vision and Pattern Recognition. pp. 770–778. https://doi.org/10.1109/CVPR.2016.90

He, K.S., Bradley, B.A., Cord, A.F., Rocchini, D., Tuanmu, M., Schmidtlein, S., Turner, W., Wegmann, M., Pettorelli, N., 2015. Will remote sensing shape the next generation of species distribution models? Remote Sens. Ecol. Conserv. 1, 4–18. https://doi.org/10.1002/rse2.7

Heavican, K., 2021. EASTERN RED CEDAR TRESS COULD BE THE BIGGEST THREAT TO NEBRASKA SANDHILLS [WWW Document]. Brownf. ag news website. URL https://brownfieldagnews.com/news/eastern-red-cedar-tress-could-be-the-biggest-threat-to-nebraska-sandhills/ (accessed 11.3.22).

Hellerich, J.A., 2006. Influence of afforestation and hillslope position on soil carbon dynamics in the Nebraska Sand Hills.

Hennings, J., Lynch, H., 2022. Depleting the Ogallala Aquifer, FactSheet Episode 278. EarthData.

Hermosilla, T., Wulder, M.A., White, J.C., Coops, N.C., 2022. Land cover classification in an era of big and open data: Optimizing localized implementation and training data selection to improve mapping outcomes. Remote Sens. Environ. 268, 112780. https://doi.org/10.1016/j.rse.2021.112780

Herold, M., Mayaux, P., Woodcock, C.E., Baccini, A., Schmullius, C., 2008. Some challenges in global land cover mapping: An assessment of agreement and accuracy in existing 1 km datasets. Remote Sens. Environ. 112, 2538–2556. https://doi.org/10.1016/J.RSE.2007.11.013

Hobza, C.M., Schepers, A.R., 2018. Groundwater Discharge Characteristics for Selected Streams Within the Loup River Basin , Nebraska , 2014 – 16 Scientific Investigations Report 2018 – 5093.

Houet, T., Hubert-Moy, L., 2006. Modeling and projecting land-use and land-cover changes with Cellular Automaton in considering landscape trajectories. EARSeL eProceedings 5, 63–76.

Hrozencik;, A., 2021. USDA ERS - Irrigation & Water Use [WWW Document]. URL https://www.ers.usda.gov/topics/farm-practices-management/irrigation-water-use/ (accessed 7.7.21).

Hu, F., Xia, G.-S., Hu, J., Zhang, L., Foody, G.M., Wang, L., Thenkabail, P.S., 2015. Transferring Deep Convolutional Neural Networks for the Scene Classification of High-Resolution Remote Sensing Imagery. Remote Sens. 2015, Vol. 7, Pages 14680-14707 7, 14680–14707. https://doi.org/10.3390/RS71114680

Hudak, A.T., Wessman, C.A., 1998. Textural Analysis of Historical Aerial Photography to Characterize Woody Plant Encroachment in South African Savanna. Remote Sens. Environ. 66, 317–330. https://doi.org/10.1016/S0034-4257(98)00078-9

Huxman, T.E., Wilcox, B.P., Breshears, D.D., Scott, R.L., Snyder, K.A., Small, E.E., Hultine, K., Pockman, W.T., Jackson, R.B., 2005. Ecohydrological implications of woody plant encroachment. Ecology 86, 308–319. https://doi.org/10.1890/03-0583

Hyde, P., Dubayah, R., Walker, W., Blair, J.B., Hofton, M., Hunsaker, C., 2006. Mapping forest structure for wildlife habitat analysis using multi-sensor (LiDAR, SAR/InSAR, ETM+, Quickbird) synergy. Remote Sens. Environ. 102, 63–73. https://doi.org/10.1016/J.RSE.2006.01.021

Im, J., Jensen, J.R., Tullis, J.A., 2008. Object-based change detection using correlation image analysis and image segmentation. Int. J. Remote Sens. 29, 399–423. https://doi.org/10.1080/01431160601075582

Jiang, W., He, G., Long, T., Ni, Y., Liu, H., Peng, Y., Lv, K., Wang, G., 2018. Multilayer Perceptron Neural Network for Surface Water Extraction in Landsat 8 OLI Satellite Images. Remote Sens. 2018, Vol. 10, Page 755 10, 755. https://doi.org/10.3390/RS10050755

Jin, X., Jin, Y., 2020. Calibration of a distributed hydrological model in a data-scarce basin based on GLEAM datasets. Water (Switzerland) 12. https://doi.org/10.3390/w12030897

Kaskie, K.D., Wimberly, M.C., Bauman, P.J., 2019. Rapid assessment of juniper distribution in prairie landscapes of the northern Great Plains. Int. J. Appl. Earth Obs. Geoinf. 83, 101946. https://doi.org/10.1016/j.jag.2019.101946

Kishawi, Y., Mittelstet, A.R., Gilmore, T.E., Twidwell, D., Roy, T., Shrestha, N., 2023. Impact of Eastern Redcedar encroachment on water resources in the Nebraska Sandhills. Sci. Total Environ. 858, 159696. https://doi.org/10.1016/j.scitotenv.2022.159696

Knapp, A.K., Briggs, J.M., Collins, S.L., Archer, S.R., Bret-Harte, M.S., Ewers, B.E., Peters, D.P., Young, D.R., Shaver, G.R., Pendall, E., Cleary, M.B., 2008. Shrub encroachment in North American grasslands: Shifts in growth form dominance rapidly alters control of ecosystem carbon inputs. Glob. Chang. Biol. 14, 615–623. https://doi.org/10.1111/j.1365-2486.2007.01512.x

Kura, A.L., Beyene, D.L., 2020. Cellular automata Markov chain model based deforestation modelling in the pastoral and agro-pastoral areas of southern Ethiopia. Remote Sens. Appl. Soc. Environ. 18, 100321. https://doi.org/10.1016/j.rsase.2020.100321

Kussul, N., Lavreniuk, M., Skakun, S., Shelestov, A., 2017. Deep Learning Classification of Land Cover and Crop Types Using Remote Sensing Data. IEEE Geosci. Remote Sens. Lett. 14, 778–782. https://doi.org/10.1109/LGRS.2017.2681128

Lassoie, J.P., Dougherty, P.M., Reich, P.B., Hinckley, T.M., Metcalf, C.M., Dina, S.J., 1983. Ecophysiological Investigations of Understory Eastern Redcedar in Central Missouri. Ecology 64, 1355–1366. https://doi.org/10.2307/1937490

Lawson, E.R., 1990. Pinus echinata Mill. shortleaf pine. Silvics North Am. 1, 316–326.

Leach, M.K., Givnish, T.J., 1996. Ecological determinants of species loss in remnant prairies. Science (80-.). 273, 1555–1558. https://doi.org/10.1126/science.273.5281.1555

LeCun, Y., Bengio, Y., Hinton, G., 2015. Deep learning. Nature 521, 436–444. https://doi.org/10.1038/nature14539

Lee, S., Yeo, I.Y., Sadeghi, A.M., McCarty, G.W., Hively, W.D., Lang, M.W., Sharifi, A., 2018. Comparative analyses of hydrological responses of two adjacent watersheds to climate variability and change using the SWAT model. Hydrol. Earth Syst. Sci. 22, 689–708. https://doi.org/10.5194/hess-22-689-2018

Lee, Yeo, I.Y., Lang, M.W., Sadeghi, A.M., McCarty, G.W., Moglen, G.E., Evenson, G.R., 2018. Assessing the cumulative impacts of geographically isolated wetlands on watershed hydrology using the SWAT model coupled with improved wetland modules. J. Environ. Manage. 223, 37–48. https://doi.org/10.1016/j.jenvman.2018.06.006

Li, Y., Zhang, H., Xue, X., Jiang, Y., Shen, Q., 2018. Deep learning for remote sensing image classification: A survey. Wiley Interdiscip. Rev. Data Min. Knowl. Discov. https://doi.org/10.1002/widm.1264

Lobell, D.B., Asner, G.P., Law, B.E., Treuhaft, R.N., 2001. Subpixel canopy cover estimation of coniferous forests in Oregon using SWIR imaging spectrometry. J. Geophys. Res. Atmos. 106, 5151–5160. https://doi.org/10.1029/2000JD900739

Loope, D., Swinehart, J., 2000. Thinking Like a Dune Field: Geologic History in the Nebraska Sand Hills. Gt. Plains Res. A J. Nat. Soc. Sci.

López, S., Stokes, D.L., 2016. Modeling the invasion of holly (Ilex aquifolium): Spatial relationships and spread trajectories. Prof. Geogr. 68, 399–413. https://doi.org/10.1080/00330124.2015.1102029

Lower Loup NRD, 2017. South Loup River Watershed Management Plan.

Ma, L., Liu, Y., Zhang, X., Ye, Y., Yin, G., Johnson, B.A., 2019. Deep learning in remote sensing applications: A meta-analysis and review. ISPRS J. Photogramm. Remote Sens. 152, 166–177. https://doi.org/10.1016/j.isprsjprs.2019.04.015

Manatsa, D., Chingombe, W., Matarira, C.H., 2008. The impact of the positive Indian Ocean dipole on Zimbabwe droughts Tropical climate is understood to be dominated by. Int. J. Climatol. 2029, 2011–2029. https://doi.org/10.1002/joc

Mas, J.-F., Kolb, M., Paegelow, M., Camacho Olmedo, M.T., Houet, T., 2014. Inductive pattern-based land use/cover change models: A comparison of four software packages. Environ. Model. Softw. 51, 94–111. https://doi.org/10.1016/j.envsoft.2013.09.010

Maurer, E.P., Brekke, L., Pruitt, T., Duffy, P.B., 2007. Fine-Resolution Climate Projections Enhance Regional Climate Change Impact Studies. Eos, Trans. Am. Geophys. Union 88, 504–504. https://doi.org/10.1029/2007eo470005

McGuire, V.L., 2017. Water-Level and Recoverable Water in Storage Changes, High Plains Aquifer, Predevelopment to 2015 and 2013-15. U.S. Geol. Surv. Sci. Investig. Rep. 2017–5040 14. https://doi.org/10.3133/SIR20175040

McGuire, Virginia L, 2017. Water-Level and Recoverable Water in Storage Changes, High Plains Aquifer, Predevelopment to 2015 and 2013-15.

McKinley, D.C., Blair, J.M., 2008. Woody plant encroachment by Juniperus virginiana in a mesic native grassland promotes rapid carbon and nitrogen accrual. Ecosystems 11, 454–468. https://doi.org/10.1007/s10021-008-9133-4

Meddens, A.J.H., Hicke, J.A., Jacobs, B.F., 2016. Characterizing the Response of Piñon-Juniper Woodlands to Mechanical Restoration Using High-Resolution Satellite Imagery. Rangel. Ecol. Manag. 69, 215–223. https://doi.org/10.1016/j.rama.2015.12.006

Mellor, A., Boukir, S., Haywood, A., Jones, S., 2015. Exploring issues of training data imbalance and mislabelling on random forest performance for large area land cover classification using the ensemble margin. ISPRS J. Photogramm. Remote Sens. 105, 155–168. https://doi.org/10.1016/J.ISPRSJPRS.2015.03.014

Meneguzzo, D.M., Liknes, G.C., 2015. Status and Trends of Eastern Redcedar (<I>Juniperus virginiana</I>) in the Central United States: Analyses and Observations Based on Forest Inventory and Analysis Data. J. For. 113, 325–334. https://doi.org/10.5849/jof.14-093

Meneguzzo, D.M., Lister, A.J., Sullivan, C., 2018. Summary of findings from the Great Plains Tree and Forest Invasives Initiative, Gen. Tech. Rep. NRS-GTR-177. Newtown Square, PA: U.S. Department of Agriculture, Forest Service, Northern Research Station. 24 p. https://doi.org/10.2737/NRS-GTR-177

Millard, K., Richardson, M., 2015. On the Importance of Training Data Sample Selection in Random Forest Image Classification: A Case Study in Peatland Ecosystem Mapping. Remote Sens. 2015, Vol. 7, Pages 8489-8515 7, 8489–8515. https://doi.org/10.3390/RS70708489

Miller, J.A., Appel, C.L., 1997. GROUND WATER ATLAS of the UNITED STATES Kansas, Missouri, and Nebraska.

Morisette, J.T., Jarnevich, C.S., Ullah, A., Cai, W., Pedelty, J.A., Gentle, J.E., Stohlgren, T.J., Schnase, J.L., 2006. A tamarisk habitat suitability map for the continental United States, Front Ecol Environ. John Wiley & Sons, Ltd. https://doi.org/10.1890/1540-9295(2006)004[0012:ATHSMF]2.0.CO;2

Mueller-Warrant, G.W., Phillips, C.L., Trippe, K.M., 2019. Use of SWAT to Model Impact of Climate Change on Sediment Yield and Agricultural Productivity in Western Oregon, USA. Open J. Mod. Hydrol. 09, 54–88. https://doi.org/10.4236/ojmh.2019.92004

Muhammad, A., Evenson, G.R., Stadnyk, T.A., Boluwade, A., Jha, S.K., Coulibaly, P., 2019. Impact of model structure on the accuracy of hydrological modeling of a Canadian Prairie watershed. J. Hydrol. Reg. Stud. 21, 40–56. https://doi.org/10.1016/j.ejrh.2018.11.005

Mundetia, N., 2019. International conference on swat-sea, siem reap, combodia, october, 24-25, 2019 hydrological impact assessment of land use change in an ungauged semi-arid river basin of rajasthan, india 24–25.

Myint, S.W., Gober, P., Brazel, A., Grossman-Clarke, S., Weng, Q., 2011. Per-pixel vs. object-based classification of urban land cover extraction using high spatial resolution imagery. Remote Sens. Environ. 115, 1145–1161. https://doi.org/10.1016/j.rse.2010.12.017

Myint, S.W., Wang, L., 2006. Multicriteria decision approach for land use land cover change using Markov chain analysis and a cellular automata approach. Can. J. Remote Sens. 32, 390–404. https://doi.org/10.5589/m06-032

Nash, J.E., Sutcliffe, J. V, 1970. RIVER FLOW FORECASTING THROLIGH CONCEPTUAL MODELS PART I - A DISCLISSION OF PRINCIPLES. J. Hydrol. 10, 282–290.

Nebraska Forest Service, 2016. Cedar Issue Paper July 2016 w signatures.pdf.

Norris, M.D., Blair, J.M., Johnson, L.C., McKane, R.B., 2001. Assessing changes in biomass, productivity, and C and N stores following Juniperus virginiana forest expansion into tallgrass prairie. Can. J. For. Res. 31, 1940–1946. https://doi.org/10.1139/x01-132

Noujdina, N. V., Ustin, S.L., 2008. Mapping Downy Brome (Bromus tectorum) Using Multidate AVIRIS Data. Weed Sci. 56, 173–179. https://doi.org/10.1614/WS-07-009.1

Oklahoma Conservation Commission, 2008. Eastern Redcedar — A Growing Threat What Has Caused the Cedar Population The Cost to Oklahoma ?

Olofsson, P., Arévalo, P., Espejo, A.B., Green, C., Lindquist, E., McRoberts, R.E., Sanz, M.J., 2020. Mitigating the effects of omission errors on area and area change estimates. Remote Sens. Environ. 236, 111492. https://doi.org/10.1016/J.RSE.2019.111492

Olofsson, P., Foody, G.M., Herold, M., Stehman, S. V., Woodcock, C.E., Wulder, M.A., 2014. Good practices for estimating area and assessing accuracy of land change. Remote Sens. Environ. 148, 42–57. https://doi.org/10.1016/J.RSE.2014.02.015

Olofsson, P., Foody, G.M., Stehman, S. V., Woodcock, C.E., 2013. Making better use of accuracy data in land change studies: Estimating accuracy and area and quantifying uncertainty using stratified estimation. Remote Sens. Environ. 129, 122–131. https://doi.org/10.1016/j.rse.2012.10.031

Olson, D.M., Dinerstein, E., 2002. The Global 200: Priority Ecoregions for Global Conservation. Ann. Missouri Bot. Gard. 89, 199. https://doi.org/10.2307/3298564

Olthof, I., Butson, C., Fraser, R., 2005. Signature extension through space for northern landcover classification: A comparison of radiometric correction methods. Remote Sens. Environ. 95, 290–302. https://doi.org/10.1016/J.RSE.2004.12.015

Overmann, S.R., 2021. The High Plains Aquifer [WWW Document]. URL https://wps.prenhall.com/wps/media/objects/1373/1406592/Regional_Updates/update23.htm (accessed 7.7.21).

Pachauri, R.K., Meyer, L., The Core Writing Team, 2015. Climate Change 2014 Synthesis Synthesis Report, United Nations Environmental Programme.

Pandey, A., Bishal, K.C., Kalura, P., Chowdary, V.M., Jha, C.S., Cerdà, A., 2021. A Soil Water Assessment Tool (SWAT) Modeling Approach to Prioritize Soil Conservation Management in River Basin Critical Areas Coupled With Future Climate Scenario Analysis. Air, Soil Water Res. 14, 117862212110213. https://doi.org/10.1177/11786221211021395

Pedro-Monzonís, M., Solera, A., Ferrer, J., Estrela, T., Paredes-Arquiola, J., 2015. A review of water scarcity and drought indexes in water resources planning and management. J. Hydrol. 527, 482–493. https://doi.org/10.1016/j.jhydrol.2015.05.003

Peerbhay, K., Mutanga, O., Lottering, R., Ismail, R., 2016. Mapping Solanum mauritianum plant invasions using WorldView-2 imagery and unsupervised random forests. Remote Sens. Environ. 182, 39–48. https://doi.org/10.1016/j.rse.2016.04.025

Perazzoli, M., Pinheiro, A., Kaufmann, V., 2013. Evaluation de l'impact des scénarios de changement climatique sur les ressources en eau dans le Brésil méridional. Hydrol. Sci. J. 58, 77–87. https://doi.org/10.1080/02626667.2012.742195

Pérez-Vega, A., Mas, J.F., Ligmann-Zielinska, A., 2012. Comparing two approaches to land use/cover change modeling and their implications for the assessment of biodiversity loss in a deciduous tropical forest. Environ. Model. Softw. 29, 11–23. https://doi.org/10.1016/j.envsoft.2011.09.011

Peterson, E.B., 2005. Estimating cover of an invasive grass (Bromus tectorum) using tobit regression and phenology derived from two dates of Landsat ETM + data. Int. J. Remote Sens. 26, 2491–2507. https://doi.org/10.1080/01431160500127815

Peterson, S.M., Flynn, A.T., Traylor, J.P., 2016. Water Availability and Use Science Program Groundwater-Flow Model of the Northern High Plains Aquifer in Colorado, Kansas, Nebraska, South Dakota, and Wyoming Scientific Investigations Report 2016-5153 Time series of simulated and estimated base flow Grou, Scientific Investigations Report. https://doi.org/10.3133/SIR20165153

Petrovic, F., 2021. Hydrological impacts of climate change and land use. Water (Switzerland) 13, 13–15. https://doi.org/10.3390/w13060799

Pettijohn, R.A., Chen, H., 1962. MAP SHOWING HYDRAULIC CONDUCTIVITY OF HIGH PLAINS AQUIFER SYSTEM HYDRAULIC CONDUCTIVITY , SPECIFIC YIELD , AND PUMPAGE-HIGH PLAINS AQUIFER SYSTEM , NEBRASKA By HYDRAULIC CONDUCTIVITY , SPECIFIC YIELD , AND PUMPAGE-HIGH PLAINS AQUIFER SYSTEM , NEBRASKA By . North.

Polley, H.W., Mayeux, H.S., Johnson, H.B., Tischler, C.R., 1997. Viewpoint: Atmospheric CO2, soil water, and shrub/grass ratios on rangelands. J. Range Manag. 50, 278–284. https://doi.org/10.2307/4003730

Pontius, G.R., Malanson, J., 2005. Comparison of the structure and accuracy of two land change models. Int. J. Geogr. Inf. Sci. 19, 243–265. https://doi.org/10.1080/13658810410001713434

Pontius, R.G., Huffaker, D., Denman, K., 2004. Useful techniques of validation for spatially explicit land-change models. Ecol. Modell. 179, 445–461. https://doi.org/10.1016/j.ecolmodel.2004.05.010

Pontius, R.G., Neeti, N., 2010. Uncertainty in the difference between maps of future land change scenarios. Sustain. Sci. 5, 39.

Pontius, R.G., Petrova, S.H., 2010. Assessing a predictive model of land change using uncertain data. Environ. Model. Softw. 25, 299–309. https://doi.org/10.1016/j.envsoft.2009.09.005

Pontius, R.G., Schneider, L.C., 2001. Land-cover change model validation by an ROC method for the Ipswich watershed, Massachusetts, USA. Agric. Ecosyst. Environ. 85, 239–248. https://doi.org/10.1016/S0167-8809(01)00187-6

Pontius, R.G., Spencer, J., 2005. Uncertainty in Extrapolations of Predictive Land-Change Models. Environ. Plan. B Plan. Des. 32, 211–230. https://doi.org/10.1068/b31152

PRISM Climate Group, 2004. PRISM Explorer, Oregon State University [WWW Document]. URL https://prism.oregonstate.edu/explorer/ (accessed 5.25.21).

Puhr, C.B., Donoghue, D.N.M., 2000. Remote sensing of upland conifer plantations using Landsat TM data: A case study from Galloway, south-west Scotland. Int. J. Remote Sens. 21, 633–646. https://doi.org/10.1080/014311600210470

Qiao, L., Zou, C.B., Will, R.E., Stebler, E., 2015. Calibration of SWAT model for woody plant encroachment using paired experimental watershed data. J. Hydrol. 523, 231–239. https://doi.org/10.1016/j.jhydrol.2015.01.056

Quintano, C., Fernández-Manso, A., Shimabukuro, Y.E., Pereira, G., 2012. Spectral unmixing. http://dx.doi.org/10.1080/01431161.2012.661095 33, 5307–5340. https://doi.org/10.1080/01431161.2012.661095

Raczko, E., Zagajewski, B., 2017. Comparison of support vector machine, random forest and neural network classifiers for tree species classification on airborne hyperspectral APEX images. Eur. J. Remote Sens. 50, 144–154. https://doi.org/10.1080/22797254.2017.1299557

Rehana, S., Sireesha Naidu, G., Naresh, A., Khan, M., Munoz-, F., Munoz-Arriola, F., 2018. Climate Change Sensitivity Assessment using SWAT for a Highly Agricultural Watershed, Shell Creek, Nebraska, USA.

Rhoades, M.G., Meza, J.L., Beseler, C.L., Shea, P.J., Kahle, A., Vose, J.M., Eskridge, K.M., Spalding, R.F., 2013. Atrazine and Nitrate in Public Drinking Water Supplies and Non-Hodgkin Lymphoma in Nebraska, USA. Environ. Health Insights. https://doi.org/10.4137/EHI.S10629

Rocchini, D., Andreo, V., Förster, M., Garzon-Lopez, C.X., Gutierrez, A.P., Gillespie, T.W., Hauffe, H.C., He, K.S., Kleinschmit, B., Mairota, P., Marcantonio, M., Metz, M., Nagendra, H., Pareeth, S., Ponti, L., Ricotta, C., Rizzoli, A., Schaab, G., Zebisch, M., Zorer, R., Neteler, M., 2015. Potential of remote sensing to predict species invasions. Prog. Phys. Geogr. Earth Environ. 39, 283–309. https://doi.org/10.1177/0309133315574659

Rodriguez-Galiano, V.F., Ghimire, B., Rogan, J., Chica-Olmo, M., Rigol-Sanchez, J.P., 2012. An assessment of the effectiveness of a random forest classifier for land-cover classification. ISPRS J. Photogramm. Remote Sens. 67, 93–104. https://doi.org/10.1016/J.ISPRSJPRS.2011.11.002

Rodriguez-Iturbe, I., 2000. Ecohydrology: A hydrologic perspective of climate-soil-vegetation dynamies. Water Resour. Res. 36, 3–9. https://doi.org/10.1029/1999WR900210

Roelfsema, M.R.G., Levchenko, V., Hedrich, R., 2004. ABA depolarizes guard cells in intact plants, through a transient activation of R- and S-type anion channels. Plant J. 37, 578–588. https://doi.org/10.1111/j.1365-313X.2003.01985.x

Rogan, J., Franklin, J., Stow, D., Miller, J., Woodcock, C., Roberts, D., 2008. Mapping land-cover modifications over large areas: A comparison of machine learning algorithms. Remote Sens. Environ. 112, 2272–2283. https://doi.org/10.1016/J.RSE.2007.10.004

Rossman, N.R., Zlotnik, V.A., Rowe, C.M., 2019. Simulating lake and wetland areal coverage under future groundwater recharge projections: The Nebraska Sand Hills system. J. Hydrol. 576, 185–196. https://doi.org/10.1016/j.jhydrol.2019.06.046

Rossman, N.R., Zlotnik, V.A., Rowe, C.M., Szilagyi, J., 2014. Vadose zone lag time and potential 21st century climate change effects on spatially distributed groundwater recharge in the semi-arid Nebraska Sand Hills. J. Hydrol. 519, 656–669. https://doi.org/10.1016/j.jhydrol.2014.07.057

Samson, F., Knopf, F., 1994. Prairie Conservation in North America. Bioscience 44, 418–421. https://doi.org/10.2307/1312365

Samson, F.B., Knopf, F.L., Ostlie, W.R., 2004. Great Plains ecosystems: past, present, and future. Wildl. Soc. Bull. 32, 6–15.

Sankey, T.T., Glenn, N., Ehinger, S., Boehm, A., Hardegree, S., 2010. Characterizing Western Juniper Expansion via a Fusion of Landsat 5 Thematic Mapper and Lidar Data. Rangel. Ecol. Manag. 63, 514–523. https://doi.org/10.2111/REM-D-09-00181.1

Scanlon, B.R., Faunt, C.C., Longuevergne, L., Reedy, R.C., Alley, W.M., McGuire, V.L., McMahon, P.B., 2012a. Groundwater depletion and sustainability of irrigation in the US High Plains and Central Valley. Proc. Natl. Acad. Sci. U. S. A. 109, 9320–9325. https://doi.org/10.1073/pnas.1200311109

Scanlon, B.R., Faunt, C.C., Longuevergne, L., Reedy, R.C., Alley, W.M., McGuire, V.L., McMahon, P.B., 2012b. Groundwater depletion and sustainability of irrigation in the US High Plains and Central Valley. Proc. Natl. Acad. Sci. U. S. A. 109, 9320–9325. https://doi.org/10.1073/pnas.1200311109

Schreiner-McGraw, A.P., Vivoni, E.R., Ajami, H., Sala, O.E., Throop, H.L., Peters, D.P.C., 2020. Woody Plant Encroachment has a Larger Impact than Climate Change on Dryland Water Budgets. Sci. Rep. 10, 1–9. https://doi.org/10.1038/s41598-020-65094-x

Shao, G., Zhang, D., Guan, Y., Xie, Y., Huang, F., 2019. Application of SWAT model with a modified groundwater module to the semi-arid Hailiutu River catchment, northwest China. Sustain. 11. https://doi.org/10.3390/su11072031

Shrestha, N., 2022. Understanding Lake Dynamics and Redcedar Encroachment in the Nebraska Sand Hills: A Remote Sensing and Modelling Perspective. Order No. 2871324 The University of Nebraska - Lincoln, 2021 Ann Arbor ProQuest. 24 Feb. 2022.

Sinha, P., Kumar, L., 2013. Markov land cover change modeling using pairs of time-series satellite images. Photogramm. Eng. Remote Sens. 79, e1051.

Smith, A.R., 1978. Color gamut transform pairs. ACM SIGGRAPH Comput. Graph. 12, 12–19. https://doi.org/10.1145/965139.807361

Smith, H.T.U., 1965. Dune Morphology and Chronology in Central and Western Nebraska. J. Geol. 73, 557–578. https://doi.org/10.1086/627093

Soil Survey, S., 2021. Gridded soil survey geographic (gSSURGO) database for the conterminous United States.

Song, C., Woodcock, C.E., Seto, K.C., Lenney, M.P., Macomber, S.A., 2001. Classification and Change Detection Using Landsat TM Data: When and How to Correct Atmospheric Effects? Remote Sens. Environ. 75, 230–244. https://doi.org/10.1016/S0034-4257(00)00169-3

Spinoni, J., Vogt, J., Naumann, G., Carrao, H., Barbosa, P., 2015. Towards identifying areas at climatological risk of desertification using the Köppen-Geiger classification and FAO aridity index. Int. J. Climatol. 35, 2210–2222. https://doi.org/10.1002/joc.4124

Srivastava, N., Hinton, G., Krizhevsky, A., Sutskever, I., Salakhutdinov, R., 2014. Dropout: A simple way to prevent neural networks from overfitting. J. Mach. Learn. Res. 15, 1929–1958.

Starks, P.J., Moriasi, D.N., 2017. Impact of Eastern redcedar encroachment on stream discharge in the North Canadian River basin. J. Soil Water Conserv. 72, 12–25. https://doi.org/10.2489/jswc.72.1.12

Staver, A.C., Bond, W.J., February, E.C., 2011. History matters: Tree establishment variability and species turnover in an African savanna. Ecosphere. https://doi.org/10.1890/ES11-00029.1

Stehman, S. V., 2009. Sampling designs for accuracy assessment of land cover. Int. J. Remote Sens. 30, 5243–5272. https://doi.org/10.1080/01431160903131000

Steward, D.R., Allen, A.J., 2016. Peak groundwater depletion in the High Plains Aquifer, projections from 1930 to 2110. Agric. Water Manag. 170, 36–48. https://doi.org/10.1016/j.agwat.2015.10.003

Strauch;, K.R., Linard;, J.I., 2009. Streamflow Simulations and Percolation Estimates Using the Soil and Water Assessment Tool for Selected Basins in North-Central Nebraska, 1940-2005, USGS.

Suttie, J.M., Reynolds, S.G., Batello, C., 2005. Grasslands of the World. Food & Agriculture Org.

Sweeney, M.R., Loope, D.B., 2001. Holocene dune-sourced alluvial fans in the Nebraska Sand Hills. Geomorphology 38, 31–46. https://doi.org/10.1016/S0169-555X(00)00067-2

Szilagyi, J.., Zlotnik, V.A.., Gates, J.B.., Jozsa, J., 2011. Mapping mean annual groundwater recharge in the Nebraska Sand Hills, USA. Hydrogeol. J. 19, 1503–1513. https://doi.org/10.1007/s10040-011-0769-3

Szilagyi, Jozsef, Jozsa, J., Kovacs, A., 2011. A Calibration-Free Evapotranspiration Mapping (CREMAP) Technique. Evapotranspiration. https://doi.org/10.5772/14277

Szilagyi, J., Zlotnik, V.A., Gates, J.B., Jozsa, J., 2011. Mapping mean annual groundwater recharge in the Nebraska Sand Hills, USA. Hydrogeol. J. 19, 1503–1513. https://doi.org/10.1007/s10040-011-0769-3

Tang, X.-J., Liu, X., Yan, P.-F., Li, B.-X., Qi, H.-Y., Huang, F., 2022. An MLP Network Based on Residual Learning for Rice Hyperspectral Data Classification. IEEE Geosci. Remote Sens. Lett. 19, 1–5. https://doi.org/10.1109/LGRS.2022.3149185

Teklay, A., Dile, Y.T., Asfaw, D.H., Bayabil, H.K., Sisay, K., 2021. Impacts of Climate and Land Use Change on Hydrological Response in Gumara Watershed, Ethiopia. Ecohydrol. Hydrobiol. 21, 315–332. https://doi.org/10.1016/j.ecohyd.2020.12.001

Thomas and Tiemann, 2015. Introductory Business Statistics with Interactive Spreadsheets - 1st Canadian Edition.

Tobella, A., Reese, H., Almaw, A., Bayala, J., Malmer, A., Laudon, H., Ilstedt, U., 2014. The effect of trees on preferential flow and soil infiltrability in an agroforestry parkland in semiarid Burkina Faso. Water Resour. Res. 50, 3342–3354. https://doi.org/10.1002/2013WR015197

Touseef, M., Chen, L., Yang, W., 2021. Assessment of Surface Water Availability under Climate Change Using Coupled SWAT-WEAP in Hongshui River Basin, China. ISPRS Int. J. Geo-Information 10, 298. https://doi.org/10.3390/ijgi10050298

Tucker, C.J., 1979. Red and photographic infrared linear combinations for monitoring vegetation. Remote Sens. Environ. 8, 127–150. https://doi.org/10.1016/0034-4257(79)90013-0

Twidwell, D., Rogers, W.E., Fuhlendorf, S.D., Wonkka, C.L., Engle, D.M., Weir, J.R., Kreuter, U.P., Taylor, C.A., 2013. The rising Great Plains fire campaign: Citizens' response to woody plant encroachment. Front. Ecol. Environ. 11. https://doi.org/10.1890/130015

U.S. Geological Survey, 2020. USGS earth explorer [WWW Document]. URL https://earthexplorer.usgs.gov/ (accessed 10.5.20).

Ustin, S.L., Roberts, D.A., Gamon, J.A., Asner, G.P., Green, R.O., 2004. Using Imaging Spectroscopy to Study Ecosystem Processes and Properties, BioScience. Oxford Academic. https://doi.org/10.1641/0006-3568(2004)054[0523:UISTSE]2.0.CO;2

Van Auken, O.W., 2009. Causes and consequences of woody plant encroachment into western North American grasslands. J. Environ. Manage. 90, 2931–2942. https://doi.org/10.1016/J.JENVMAN.2009.04.023

Van Liew, M.W., Arnold, J.G., Bosch, D.D., 2005. Problems and potential of autocalibrating a hydrologic model. Trans. Am. Soc. Agric. Eng. 48, 1025–1040. https://doi.org/10.13031/2013.18514

van Liew, M.W., Feng, S., Pathak, T.B., 2012. Climate change impacts on streamflow, water quality, and best management practices for the shell and logan creek watersheds in Nebraska. Int. J. Agric. Biol. Eng. 5, 13–34. https://doi.org/10.3965/j.ijabe.20120501.003

Vázquez-Quintero, G., Solís-Moreno, R., Pompa-García, M., Villarreal-Guerrero, F., Pinedo-Alvarez, C., Pinedo-Alvarez, A., 2016. Detection and projection of forest changes by using the Markov Chain model and cellular automata. Sustain. 8, 236. https://doi.org/10.3390/su8030236

Walker, T.L., Hoback, W.W., 2007. Effects of invasive eastern redcedar on capture rates of Nicrophorus americanus and other silphidae. Environ. Entomol. 36, 297–307. https://doi.org/10.1603/0046-225X(2007)36[297:EOIERO]2.0.CO;2

Wang, C., Jia, M., Chen, N., Wang, W., 2018. Long-Term Surface Water Dynamics Analysis Based on Landsat Imagery and the Google Earth Engine Platform: A Case Study in the Middle Yangtze River Basin. Remote Sens. 10, 1635. https://doi.org/10.3390/rs10101635

Wang, J., Hu, L., Li, D., Ren, M., 2020. Potential Impacts of Projected Climate Change under CMIP5 RCP Scenarios on Streamflow in the Wabash River Basin. Adv. Meteorol. 2020. https://doi.org/10.1155/2020/9698423

Wang, J., Xiao, X., Qin, Y., Dong, J., Geissler, G., Zhang, G., Cejda, N., Alikhani, B., Doughty, R.B., 2017. Mapping the dynamics of eastern redcedar encroachment into grasslands during 1984–2010 through PALSAR and time series Landsat images. Remote Sens. Environ. 190, 233–246. https://doi.org/10.1016/j.rse.2016.12.025

Wang, J., Xiao, X., Qin, Y., Doughty, R.B., Dong, J., Zou, Z., 2018. Characterizing the encroachment of juniper forests into sub-humid and semi-arid prairies from 1984 to 2010 using PALSAR and Landsat data. Remote Sens. Environ. 205, 166–179. https://doi.org/10.1016/j.rse.2017.11.019

Weisberg, P.J., Lingua, E., Pillai, R.B., 2007. Spatial Patterns of Pinyon–Juniper Woodland Expansion in Central Nevada. Rangel. Ecol. Manag. 60, 115–124. https://doi.org/10.2111/05-224R2.1

Wilson, T.B., Witkowski, E.T.F., 1998. Water requirements for germination and early seedling establishment in four African savanna woody plant species. J. Arid Environ. 38, 541–550. https://doi.org/10.1006/JARE.1998.0362

Wine, M.L., Hendrickx, J.M.H., 2013. Biohydrologic effects of eastern redcedar encroachment into grassland, Oklahoma, USA. Biol. 68, 1132–1135. https://doi.org/10.2478/s11756-013-0252-9

Xu, Z., Jiang, Y., Jia, B., Zhou, G., 2016. Elevated-CO2 response of stomata and its dependence on environmental factors. Front. Plant Sci. 7, 1–15. https://doi.org/10.3389/fpls.2016.00657

Yapo, P.O., Gupta, H.V., Sorooshian, S., 1996. Automatic calibration of conceptual rainfall-runoff models: Sensitivity to calibration data. J. Hydrol. 181, 23–48. https://doi.org/10.1016/0022-1694(95)02918-4

Zha, Y., Gao, J., Ni, S., 2010. Use of normalized difference built-up index in automatically mapping urban areas from TM imagery. https://doi.org/10.1080/01431160304987 24, 583–594. https://doi.org/10.1080/01431160304987

Zhang, C., Pan, X., Li, H., Gardiner, A., Sargent, I., Hare, J., Atkinson, P.M., 2018. A hybrid MLP-CNN classifier for very fine resolution remotely sensed image classification. ISPRS J. Photogramm. Remote Sens. 140, 133–144. https://doi.org/10.1016/j.isprsjprs.2017.07.014

Zhang, L., Nan, Z., Xu, Y., Li, S., 2016. Hydrological impacts of land use change and climate variability in the headwater region of the Heihe River Basin, northwest China. PLoS One 11, 1–25. https://doi.org/10.1371/journal.pone.0158394

Zhang, L., Wang, C., Liang, G., Cui, Y., Zhang, Q., 2020. Influence of land use change on hydrological cycle: Application of SWAT to Su-Mi-Huai area in Beijing, China. Water (Switzerland) 12, 1–17. https://doi.org/10.3390/w12113164

Zhou, Q., Tollerud, H., Barber, C., Smith, K., Zelenak, D., 2020. Training Data Selection for Annual Land Cover Classification for the Land Change Monitoring, Assessment, and Projection (LCMAP) Initiative. Remote Sens. 2020, Vol. 12, Page 699 12, 699. https://doi.org/10.3390/RS12040699

Zhu, Z., Gallant, A.L., Woodcock, C.E., Pengra, B., Olofsson, P., Loveland, T.R., Jin, S., Dahal, D., Yang, L., Auch, R.F., 2016. Optimizing selection of training and auxiliary data for operational land cover classification for the LCMAP initiative. ISPRS J. Photogramm. Remote Sens. 122, 206–221. https://doi.org/10.1016/J.ISPRSJPRS.2016.11.004

Zou, C., Turton, D., Engle, D., 2010. How eastern redcedar encroachment affects the water cycle of Oklahoma rangelands 1–4.

Zou, C.B., Caterina, G.L., Will, R.E., Stebler, E., Turton, D., 2015. Canopy interception for a tallgrass prairie under juniper encroachment. PLoS One 10, 1–19. https://doi.org/10.1371/journal.pone.0141422

Zou, C.B., Turton, D.J., Will, R.E., Engle, D.M., Fuhlendorf, S.D., 2014. Alteration of hydrological processes and streamflow with juniper (Juniperus virginiana) encroachment in a mesic grassland catchment. Hydrol. Process. 28, 6173–6182. https://doi.org/10.1002/hyp.10102

Zou, C.B., Twidwell, D., Bielski, C.H., Fogarty, D.T., Mittelstet, A.R., Starks, P.J., Will, R.E., Zhong, Y., Acharya, B.S., 2018. Impact of Eastern redcedar proliferation on water resources in the great plains USA-current state of knowledge. Water (Switzerland) 10. https://doi.org/10.3390/w10121768